

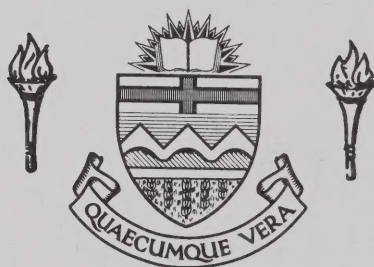
# **For Reference**

---

**NOT TO BE TAKEN FROM THIS ROOM**



Ex LIBRIS  
UNIVERSITATIS  
ALBERTAENSIS







THE UNIVERSITY OF ALBERTA

STUDY OF LEVELS IN  $^{154}\text{Sm}$  AND  $^{160}\text{Gd}$  BY THE  $(n,n'\gamma)$  REACTION  
USING A NEW SMALL SAMPLE METHOD

by



Sayed Aly Omar ELBAKR

A THESIS

SUBMITTED TO THE FACULTY OF GRADUATE STUDIES AND RESEARCH  
IN PARTIAL FULFILMENT OF THE REQUIREMENTS FOR THE DEGREE  
OF DOCTOR OF PHILOSOPHY

DEPARTMENT OF PHYSICS

EDMONTON, ALBERTA

FALL, 1972





## ABSTRACT

A technique has been developed which makes it possible to study  $(n,n'\gamma)$  reactions using very small scattering samples in a close geometry. To show that reliable  $\gamma$ -ray yield curves can be obtained with this method, the excitation curve for the 847 keV  $\gamma$ -ray from  $^{56}\text{Fe}$  has been measured. The resulting yield curve is in good agreement with previous measurements obtained by conventional techniques.

The method has been applied to the study of levels above 900 keV excitation in  $^{154}\text{Sm}$  and  $^{160}\text{Gd}$  populated by the  $(n,n'\gamma)$  reaction. De-excitation  $\gamma$ -rays were observed at several neutron energies between 0.9 and 2.3 MeV. The  $\gamma$ -ray production cross sections have been obtained at these neutron energies and were used to determine neutron inelastic scattering cross sections for reactions leading to several states in these nuclei. The experimental results were compared with the predictions of the statistical theory to establish level spins.

The  $^{154}\text{Sm}$  nucleus: Previously known spin assignments have been confirmed:  $1^-$  for the 921 keV level,  $3^-$  for the 1012 keV level,  $0^+$  for the 1099 keV level,  $1^-$  for the 1475 keV level and  $3^-$  for the 1585 keV level. The 1178 and 1182 keV levels were clearly resolved and assigned spins of  $2^+$  and  $5^-$ , respectively. Existence of levels at 1202, 1286, 1338, 1515, 1539, 1707 and

Digitized by the Internet Archive  
in 2023 with funding from  
University of Alberta Library

<https://archive.org/details/Elbakr1972>



1755 keV has been confirmed. A level at 1674 keV is tentatively proposed. Spin assignments of  $4^+$  and  $3^+$  have been made for the 1338 and 1539 keV levels, respectively. Tentative assignments are:  $0^+$  to the 1202 keV level,  $3^-$  to the 1286 keV level,  $3$  to the 1515 keV level,  $0^+$  to the 1674 keV level,  $4^+$  to the 1707 keV level and  $2^+$  to the 1755 keV level.

The  $^{160}\text{Gd}$  nucleus: Spin assignments of  $2^+$  and  $3^-$  were obtained for the 989 and 1290 keV levels, respectively, in agreement with previous results. An assignment of  $3^+$  and  $1^-$  has been made for the 1058 and 1225 keV states, respectively. The levels at 1071 and 1149 keV were tentatively assigned a  $J^\pi = 4^+$ . Seven new levels are proposed at 1262, 1351, 1378, 1381, 1569, 1587 and 1599 keV. A spin of  $1^-$  was assigned to the 1351 keV level. Tentative assignments are:  $4^+$  to the 1262 keV level,  $0^+$  or  $1^-$  to the 1378 and 1381 keV levels, and  $1^-$  or  $2^+$  to the 1569, 1587 and 1599 keV levels.

Reduced transition probability ratios for  $\gamma$ -rays depopulating members of rotational bands observed in  $^{154}\text{Sm}$  and  $^{160}\text{Gd}$  were compared to the predictions of the Bohr-Mottelson collective model. The results indicate that these nuclei are good rotors.

The  $^7\text{Li}(p,n)^7\text{Be}$  reaction was used as a neutron source. Analysis of the  $\gamma$ -ray data requires an accurate knowledge of the angular distribution of neutrons from this reaction. Consequently a systematic measurement of absolute differential cross section as a function of both energy and angle for the  $^7\text{Li}(p,n_0)^7\text{Be}$  and



${}^7\text{Li}(\text{p}, \text{n}_1){}^7\text{Be}$  reactions has been carried out at proton energies from 2.60 to 5.40 MeV and laboratory angles between  $0^\circ$  and  $150^\circ$ .





## ACKNOWLEDGEMENTS

I would like to thank my supervisor, Dr. G.C. Neilson, not only for suggesting this project but also for his active participation and continuous support.

I am greatly indebted to Dr. I.J. van Heerden of the Southern Universities Nuclear Institute in South Africa. Without his help the experimental part would not have been finished in so short a time. Thanks are also extended to Dr. J.W. McDonald for his interest and contribution.

I would like to express my gratitude to Dr. H.S. Sherif, who gave freely of his time to explain many points during the analysis and for his valuable comments on the theoretical chapter. Discussions with him were a delight and have considerably added to my knowledge of nuclear theory.

The assistance of Dr. B.C. Robertson is also appreciated.

I am grateful to Dr. D. Gill, who read the manuscript, and to Drs. J. Cameron and D. Hutcheon who also read some sections, and made many valuable comments.

Thanks are extended to Dr. W.K. Dawson and Mr. J. Easton for providing an excellent data acquisition system, and also to the technical staff, in particular, Miss Greta Tratt, J. Elliott, P. Ford, L. Holm, P. Karvonen, R. Popik, C. Green and H. Nielsen. In addition I would like to thank Dr. M.G. Faulkner and Mr. A. Smart of the





Department of Mechanical Engineering for their assistance in making the scatterers.

The cooperative and friendly attitude of my colleagues, W. Chung, P. Green, A. Hussein, T. Sharma, J. Soukup, D. White E. Wong and my 'always drunk' friend Jim, is highly appreciated. Farewell to our dirty noon shows.

Many thanks to Mrs. J. Korte and Mr. R. Teshima, who helped in computer programming and to Miss Barbara Podmore who carefully proofread this thesis.

My sincere thanks to Miss Audrey Forman for the excellent typing of the manuscript in spite of "many" last minute changes.

I am grateful to my wife Mona for her patience and understanding and also to my daughter Suzanne.

Finally I wish to thank the University of Alberta for financial assistance during the years of graduate study.



## TABLE OF CONTENTS

	Page
CHAPTER I INTRODUCTION	1
CHAPTER II STATISTICAL THEORY OF NUCLEAR REACTIONS	5
2.1 Introduction	5
2.2 Statistical Theory Predictions for Average Cross Sections	6
2.3 Refinements —The Hauser-Feshbach Formula	13
2.4 The Width Fluctuation Correction	17
CHAPTER III THE SMALL SAMPLE METHOD FOR INVESTIGATION OF THE (n,n' $\gamma$ ) REACTION	20
3.1 Experimental Method	20
3.2 Data Reduction	23
3.3 Experimental Results	32
CHAPTER IV APPLICATIONS: STUDY OF LEVELS IN $^{154}\text{Sm}$ AND $^{160}\text{Gd}$ NUCLEI	37
4.1 Experimental and Data Reduction	37
4.2 Statistical Theory Calculations	42
4.3 The Sm Results	47
4.3.1 The 921, 1202 and 1286 keV levels	47
4.3.2 The 1012 and 1099 keV levels	51
4.3.3 The 1178 and 1182 keV levels	53
4.3.4 The 1338, 1440 and 1707 keV levels	53
4.3.5 The 1475, 1662 and 1515 keV levels	56
4.3.6 The 1539 and 1585 keV levels	58
4.3.7 Other levels	60
4.3.8 Level scheme and band structure of $^{154}\text{Sm}$	62





	Page
4.4 The Gd Results	64
4.4.1 The 989 keV level	66
4.4.2 The 1058 keV level	69
4.4.3 The 1071 and 1149 keV levels	69
4.4.4 The 1225 and 1290 keV levels	73
4.4.5 Other levels	76
4.4.6 Level scheme and structure of $^{160}\text{Gd}$	82
4.5 Interpretation of Results in Terms of the Collective Model	84
4.5.1 Background	84
4.5.2 Comparison of experimental and theoretical B(EL) ratios	88
CHAPTER V CONCLUSIONS	93
REFERENCES	95
APPENDIX A MEASUREMENT OF NEUTRON DISTRIBUTIONS FROM THE $^7\text{Li}(p,n)^7\text{Be}$ REACTION	
APPENDIX B GEOMETRICAL INTEGRATION OF NEUTRON FLUX	





## LIST OF TABLES

	Page
Table 4.1      Weight and dimensions of scatterers	38
Table 4.2      Excitation energies and branching ratios of levels in $^{154}\text{Sm}$	48
Table 4.3      Excitation energies and branching ratios of levels in $^{160}\text{Gd}$	65
Table 4.4      Experimental and theoretical ratios of transition probabilities from members of the octupole band in $^{154}\text{Sm}$ and $^{160}\text{Gd}$	89
Table 4.5      Experimental and theoretical ratios of transition probabilities from members of the $\gamma$ -band in $^{154}\text{Sm}$ and $^{160}\text{Gd}$	90
Table 4.6      Experimental and theoretical ratios of reduced E2 transition probabilities from members of the $\beta$ - band in $^{154}\text{Sm}$	91



## LIST OF FIGURES

	Page
Figure 3.1 Schematic diagram of experimental set-up	21
Figure 3.2 Schematic drawing of a cylindrical scatterer	26
Figure 3.3 Side view of the scatterer indicating the limits of integration over $\rho$ and $z$ variables	29
Figure 3.4 Time spectrum from the TAC associated with the Ge(Li) detector	33
Figure 3.5 Fe( $n, n'\gamma$ ) spectrum	35
Figure 3.6 Excitation curve for the 847 keV $\gamma$ -ray from $^{56}\text{Fe}$	36
Figure 4.1 $^{160}\text{Gd}(n, n'\gamma)$ spectrum	39
Figure 4.2 $^{154}\text{Sm}(n, n'\gamma)$ spectrum	41
Figure 4.3 Experimental and theoretical inelastic scattering cross sections of neutrons leading to the 847 keV state of $^{56}\text{Fe}$	46
<u>For <math>^{154}\text{Sm}</math>:</u>	
Figure 4.4 Excitation curves for the 921 keV level and the 1120 and 1204 keV $\gamma$ -rays which depopulate the 1202 and 1286 keV levels, respectively.	49





	Page
Figure 4.5    Excitation curves for the 1012 (a) and 1099 (b) keV levels	52
Figure 4.6    Excitation curves for the 1178 and 1182 keV levels	54
Figure 4.7    Excitation curves for the 1388 (a), 1440 and 1707 (b) keV levels	55
Figure 4.8    (a) Excitation curve of the 1393 keV $\gamma$ -ray from the 1475 and 1662 keV levels (b) The excitation curve of the 1515 keV level	57
Figure 4.9    Excitation curve of the 1539 (a) and 1585 (b) keV levels	59
Figure 4.10   Excitation curve of (a) the 1755 keV level and (b) the 753 keV $\gamma$ -ray	61
Figure 4.11   Level scheme of $^{154}\text{Sm}$	63
<u>For <math>^{160}\text{Gd}</math>:</u>	
Figure 4.12   The neutron transmission functions of $^{160}\text{Gd}$ for various partial waves using Rosen and Moldauer potentials	67
Figure 4.13   Excitation curve of the 989 keV level	68
Figure 4.14   Excitation curve of the 1058 keV level	70



Figure 4.15	Excitation curve of the 1071 keV level	Page 72
Figure 4.16	Excitation curve of the 1149 keV level	74
Figure 4.17	Excitation curve of the 1225 keV level	75
Figure 4.18	Excitation curve of the 1215 keV $\gamma$ -ray and 1290 keV level	77
Figure 4.19	Excitation curves of the 1187 and 1013 keV $\gamma$ -rays and the 1262 keV levels	78
Figure 4.20	Excitation curve of the 1351 keV level	79
Figure 4.21	Excitation curves of the 1303 and 1306 keV $\gamma$ -rays	80
Figure 4.22	Level decay scheme of $^{160}\text{Gd}$	83





## CHAPTER I

### INTRODUCTION

Measurements of  $\gamma$ -ray energies and intensities emitted after neutron inelastic scattering, coupled with the application of the statistical theory of nuclear reactions, can provide useful information about the energy, decay mode and spin of excited states of the scattering nuclei.

The use of neutrons to excite levels for decay studies is experimentally favorable over that of charged particles. With neutrons one can, by adjusting their energy, excite and observe each level in turn so that the  $\gamma$ -spectrum is not complicated by radiation due to higher levels. With charged particles, however, higher bombarding energies are required to overcome the Coulomb barrier, resulting in excitation of a large number of levels at once and increasing the probability of occurrence of competing reactions which contribute to the complexities of the  $\gamma$ -spectrum.

The possibility of exciting only a few final states in neutron inelastic scattering leads to a simple situation in which the theory can predict the magnitude of the cross section within 10% (Vo 68). This remarkable success of the theory has greatly enhanced the effectiveness of these reactions for establishing level spins.

The number of nuclei which can be studied by neutron inelastic



scattering is normally limited by the necessity of using large scattering samples containing 1 - 2 mol of material. Many of the elements of interest, especially in the  $A > 100$  mass region where the statistical theory should be particularly applicable, occur in an isotopically impure form and this obviously complicates the interpretation of results. It is often prohibitively expensive or physically impossible to obtain such large quantities of the enriched isotope.

This thesis describes a new method which has been developed to carry out  $(n,n'\gamma)$  reactions with only 0.01 mol of scattering material. This has been accomplished by placing the scatterer in close proximity to the neutron source to make the neutron flux as large as possible in the scatterer. Two difficulties then occur. Firstly, the neutron beam through the scatterer is neither mono-energetic nor of constant flux; this is because energy and cross section are quite angle dependent for all the commonly used neutron producing reactions (Go 63). Secondly, there is no possibility of shielding the  $\gamma$ -detector from the neutron beam. An analysis routine has been developed which overcomes the first difficulty. In addition, time-of-flight gating of the  $\gamma$ -ray spectra has proven to be adequate to reduce background to acceptable levels despite the lack of shielding. In order to check whether this method would give reliable cross section information, the excitation curve of the 847 keV  $\gamma$ -ray of  $^{56}\text{Fe}$  was measured using this technique with a 3.147 g sample of natural iron. When the results were compared





with those of the conventional technique, good agreement was obtained.

The method was then applied to the study of nuclei in the rare-earth region, namely  $^{154}\text{Sm}$  and  $^{160}\text{Gd}$ . Although the structure of  $^{154}\text{Sm}$  has been the subject of several studies (Ke 64, Yo 65, Bj 66, Ze 66, Se 66, Ve 68, Da 71), relatively little information about the levels of  $^{160}\text{Gd}$  is available (Yo 65, Sh 66, Bl 67). Prior to the initiation of the present work, knowledge of the decay properties of both nuclei were incomplete and severely limited by the poor resolution of NaI detectors. Moreover, level spins were not well established. The reactions previously used to study these nuclei preferentially excite some states depending on their structure. The present investigation has been carried out using the  $(n,n'\gamma)$  reaction which has the advantage of populating levels independent of their character, provided that the statistical theory requirements are satisfied. Furthermore, the measured inelastic cross sections can be compared with the predictions of the statistical theory to determine level spins.

In the present study we have utilized the high resolution of Ge(Li) detectors to observe  $\gamma$ -rays following neutron-inelastic scattering on  $^{154}\text{Sm}$  and  $^{160}\text{Gd}$ . Level excitation energies and decay modes have been inferred from measurements of  $\gamma$ -ray energies and intensities, respectively. Inelastic cross sections for the observed levels were determined at incident neutron energies of 1 to 2 MeV and compared with theoretical calculations to obtain level spins.



Reduced  $\gamma$ -ray transition probabilities have been interpreted in the framework of the Bohr and Mottelson (Bo 53) collective model of deformed nuclei.

It is worth mentioning that while the analysis of the present data was in progress, the  $\gamma$ -decay work of D'Auria et al. (Da 71) came to our attention prior to its publication and the results were exchanged.

An outline of the statistical theory of nuclear reactions is given in Chapter II. The small sample method has been described in Chapter III, where a measurement of the excitation curve of the 847 keV  $\gamma$ -ray from  $^{56}\text{Fe}$  and its comparison to previous results are reported. Chapter IV contains the application of this method to the study of levels in  $^{154}\text{Sm}$  and  $^{160}\text{Gd}$ , whereas the conclusions of the present work are summarized in Chapter V.



## CHAPTER II

### THE STATISTICAL THEORY OF NUCLEAR REACTIONS

#### 2.1 Introduction

The statistical theory is based on the compound nucleus (CN) picture of nuclear reactions. According to this picture the incident projectile is absorbed by the target nucleus to form an excited compound system. This compound nucleus subsequently decays, generally after a time long compared with the nuclear transit time, into the energetically allowed channels. At low incident energies, compound nucleus processes are characterized by the appearance of isolated resonances in their excitation functions; these resonances correspond to levels in the CN. As the energy increases, the number of resonances increases and their widths  $\Gamma$  become greater than the spacings  $D$  between them so that they overlap with each other. If the energy spread of the incident beam  $\Delta E$  is such that  $\Delta E \gg \Gamma$ , then the measured cross sections represent an energy average over many resonances that are covered by the energy spread of the incident beam. The statistical theory of nuclear reactions deals with such average cross sections.

Mathematical development of the statistical theory is given in numerous publications which are referred to in the recent review article by Vogt (Vo 68). In this chapter, we give a brief outline of the ideas involved in the statistical model treatment.





## 2.2 Statistical Theory Predictions for Average Cross Sections

Consider the reaction

$$\alpha \rightarrow \beta$$

where  $\alpha$  labels the incident particle, the target nucleus and their state of excitation.  $\alpha$  is called the entrance channel.

$\beta$  labels the outgoing particle, the residual nucleus and their state of excitation.  $\beta$  is one of many possible exit channels.

In the absence of spins, the cross section for this reaction can be written as (Fr 55)

$$\sigma_{\alpha\beta} = \frac{\pi}{k_{\alpha}^2} \left| \delta_{\alpha\beta} - S_{\alpha\beta} \right|^2 \quad [2.1]$$

where  $k_{\alpha}$  is the wave number of the relative motion of the pair  $\alpha$ , and  $S_{\alpha\beta}$  is the scattering matrix element which is the amplitude of the outgoing wave in the channel  $\beta$  when there is an incoming wave of unit amplitude in the channel  $\alpha$ . In general, this reaction can occur directly without passing through the CN state and/or by forming a CN which decays into the channel  $\beta$ . Thus the cross section  $\sigma_{\alpha\beta}$  will have two components; a direct interaction (DI) component and a CN component. The DI component



varies smoothly with energy. If the CN is formed at a high excitation where the levels strongly overlap then the CN component of  $\sigma_{\alpha\beta}$  will fluctuate rapidly with energy. These fluctuations are indicative of rapid variations of  $S_{\alpha\beta}$ . It is then convenient to decompose the S-matrix into two parts --  $\bar{S}$  which varies smoothly with energy and  $\tilde{S}$  which fluctuates rapidly with energy. Thus

$$S_{\alpha\beta} = \bar{S}_{\alpha\beta} + \tilde{S}_{\alpha\beta} \quad [2.2]$$

Eq. (2.1) then becomes

$$\sigma_{\alpha\beta} = \frac{\pi}{k_{\alpha}^2} | \delta_{\alpha\beta} - \bar{S}_{\alpha\beta} - \tilde{S}_{\alpha\beta} |^2 \quad [2.3]$$

If the energy spread of the incident beam is large enough to excite many levels of the CN, then the measured cross section represents an energy average. Therefore we average expression (2.3) over the beam energy spread to get:

$$\langle \sigma_{\alpha\beta} \rangle = \frac{\pi}{k_{\alpha}^2} \langle | (\delta_{\alpha\beta} - \bar{S}_{\alpha\beta}) - \tilde{S}_{\alpha\beta} |^2 \rangle \quad [2.4]$$

$$\begin{aligned} &= \frac{\pi}{k_{\alpha}^2} [ \langle | \delta_{\alpha\beta} - \bar{S}_{\alpha\beta} |^2 \rangle - \langle (\delta_{\alpha\beta} - \bar{S}_{\alpha\beta}) \tilde{S}_{\alpha\beta}^{\dagger} \rangle \\ &\quad - \langle (\delta_{\alpha\beta} - \bar{S}_{\alpha\beta}^{\dagger}) \tilde{S}_{\alpha\beta} \rangle + \langle | \tilde{S}_{\alpha\beta} |^2 \rangle ] \end{aligned} \quad [2.5]$$



This hypothesis allows the factorization of the cross section into a formation part and a decay part:

$$\langle \sigma_{\alpha\beta}^{\text{CN}} \rangle = \sigma_{\alpha} P_{\beta} \quad [2.10]$$

where  $\sigma_{\alpha}$  is the cross section for formation of the CN and  $P_{\beta}$  is its decay probability through the channel  $\beta$ .

Since the CN must decay, then

$$\sum_{\beta} P_{\beta} = 1, \quad [2.11]$$

and hence

$$\sum_{\beta} \langle \sigma_{\alpha\beta}^{\text{CN}} \rangle = \sigma_{\alpha} \sum_{\beta} P_{\beta} = \sigma_{\alpha} \quad [2.12]$$

But from (2.8) and (2.9) we have

$$\langle \sigma_{\alpha\beta}^{\text{CN}} \rangle = \frac{\pi}{k_{\alpha}^2} \langle |\tilde{S}_{\alpha\beta}| \rangle \quad [2.13]$$

therefore

$$\sigma_{\alpha} = \frac{\pi}{k_{\alpha}^2} \sum_{\beta} \langle |\tilde{S}_{\alpha\beta}| \rangle \quad [2.14]$$

From conservation of flux, it follows that

*the S-matrix is unitary, i.e.*

$$\sum_{\beta} S_{\alpha\beta}^{\dagger} S_{\alpha\beta} = 1$$





The corresponding energy-averaged expression is

$$\sum_{\beta} \langle S_{\alpha\beta}^{\dagger} S_{\alpha\beta} \rangle = 1 \quad [2.15]$$

then we get

$$\sum_{\beta} \langle (\bar{S}_{\alpha\beta}^{\dagger} + \tilde{S}_{\alpha\beta}^{\dagger}) (\bar{S}_{\alpha\beta} + \tilde{S}_{\alpha\beta}) \rangle = 1$$

$$\sum_{\beta} |\bar{S}_{\alpha\beta}|^2 + \sum_{\beta} \langle |\tilde{S}_{\alpha\beta}|^2 \rangle = 1 \quad [2.16]$$

Substituting (2.16) in (2.14) we obtain

$$\sigma_{\alpha} = \frac{\pi}{k_{\alpha}^2} (1 - \sum_{\beta} |\bar{S}_{\alpha\beta}|^2) \quad [2.17]$$

This equation shows that the elements of the DI part of the S-matrix are capable of determining the CN formation cross section. In pursuing the consequences of this striking observation, we note that eq. (2.17) can be written in terms of a transmission coefficient  $\bar{T}_{\alpha}$ ,

$$\bar{T}_{\alpha} = 1 - \sum_{\beta} |\bar{S}_{\alpha\beta}|^2 \quad [2.18]$$

which expresses the loss so far as the DI processes are concerned. Eq. (2.17) then takes the form

$$\sigma_{\alpha} = \frac{\pi}{k_{\alpha}^2} \bar{T}_{\alpha} \quad [2.19]$$



The optical model permits, in a phenomenological way, the calculation of the diagonal elements  $S_{\alpha\alpha}$  of the S-matrix. These are related to the optical model phase shifts  $\delta_\alpha$  by the relation

$$\overline{S}_{\alpha\alpha} = e^{2i\delta_\alpha} \quad [2.20]$$

The transmission coefficients (2.18) are then approximated by the optical model transmission coefficient

$$T_\alpha = 1 - |e^{2i\delta_\alpha}|^2 \quad [2.21]$$

For low energy reactions where nonelastic direct reactions ( $\alpha \neq \beta$ ) are negligible, eq. (2.21) is considered to be a good approximation.

The cross section  $\langle \sigma_{\alpha\beta}^{CN} \rangle$  is now given by:

$$\langle \sigma_{\alpha\beta}^{CN} \rangle = \frac{\pi}{k_\alpha^2} T_\alpha P_\beta \quad [2.22]$$

To calculate  $P_\beta$  we assume that

*the S-matrix is invariant under time-reversal, i.e.*

$$S_{\alpha\beta} = S_{\beta\alpha}^* \quad [2.23]$$

where reversed arrows denote time-reversed channels. This implies that the amplitude for the reaction  $\alpha \rightarrow \beta$  is the same



as the amplitude for the time-reversed reaction  $\beta \rightarrow \alpha$ ; this is known as the reciprocity theorem. (Although spin projections will be reversed, we are going to ignore that here since it does not effect the final result because we always sum over spin projections.) The reciprocity property for the fluctuating part of the S-matrix leads to the following relation between cross sections:

$$k_{\alpha}^2 \langle \sigma_{\alpha\beta}^{CN} \rangle = k_{\beta}^2 \langle \sigma_{\beta\alpha}^{CN} \rangle \quad [2.24]$$

which, together with eq. (2.22), gives

$$T_{\alpha} P_{\beta} = T_{\beta} P_{\alpha} \quad [2.25]$$

Similarly, for another exit channel  $\gamma$ ,

$$T_{\alpha} P_{\gamma} = T_{\gamma} P_{\alpha} \quad [2.26]$$

from (2.25) and (2.26) we get

$$P_{\beta} / P_{\gamma} = T_{\beta} / T_{\gamma}$$

which allows us to write:

$$P_{\beta} = a T_{\beta} \quad [2.27]$$

where  $a$  is constant. If we sum eq. (2.27) over all outgoing channels





$$\sum_{\beta} P_{\beta} = a \sum_{\beta} T_{\beta} = 1$$

we get

$$a = \frac{1}{\sum_{\beta} T_{\beta}} \quad [2.28]$$

substituting (2.27) in (2.26) yields

$$P_{\beta} = T_{\beta} / \sum_{\gamma} T_{\gamma} \quad [2.29]$$

The CN cross section can now be written in terms of transmission coefficients as

$$\langle \sigma_{\alpha\beta}^{CN} \rangle = \frac{\pi}{k_{\alpha}^2} \frac{T_{\alpha} T_{\beta}}{\sum_{\gamma} T_{\gamma}} \quad [2.30]$$

This equation gives the energy average CN cross section in the absence of spin.

### 2.3 Refinements - The Hauser-Feshbach Formula

Although it is assumed that the processes of formation and decay of the CN are independent, the energy, total angular momentum and parity must all be conserved. When these restrictions are taken into account a refined version of eq. (2.30) is obtained; it is often referred to as the Hauser-Feshbach formula after the authors who first added conservation of total angular momentum and parity to the calculation of neutron inelastic cross sections (Ha 52).



To incorporate angular momentum and parity in eq. (2.30) we shall use  $\alpha$  to denote the pair of particles and their state of excitation as well as the following set of quantum numbers:

$s$  = intrinsic spin of the incident particle

$I$  = intrinsic spin of the target nucleus

$s$  = channel spin formed by coupling  $s$  with  $I$

$\ell$  = orbital angular momentum

$J$  = total angular momentum formed by coupling  $\ell$  with  $s$

$M_J$  = z-component of  $J$

$\Pi$  = total parity which is the product of  $(-1)^\ell$  with the intrinsic parities of the pair  $\alpha$ .

In what follows, we shall assume that all reactions are independent of  $M_J$  and that  $M_J$  can be averaged over and ignored.

Following the same steps given in §2.2 and applying spin and parity conservation restrictions, we can write  $\langle \sigma_{\alpha\alpha'}^{CN} \rangle$  explicitly as (Vo 68)

$$\langle \sigma_{\alpha\alpha'}^{CN} \rangle = \frac{\pi}{k_\alpha^2} \sum_{J\Pi} \frac{(2J+1)}{(2s+1)(2I+1)} \left\{ \sum_{s\ell} T_\ell(\alpha) \right\} \left\{ \frac{\sum_{s'\ell'} T_{\ell'}(\alpha')}{\sum_{\alpha''s''\ell''} T_{\ell''}(\alpha'')} \right\} \quad [2.31]$$

where the unprimed quantities refer to incoming channels of the reaction, the primed quantities refer to the outgoing channels, and the double primed quantities in the denominator are summed over all channels to which the CN can decay. The sums in eq. (2.31) run over the following values:  $\Pi$  is positive or negative;



$J$  has the values  $0, 1, 2, \dots$  if the CN has an even mass number and the values  $1/2, 3/2, 5/2, \dots$  otherwise;  $S$  takes on all integer values between  $|J - s|$  and  $J + s$  if the pair  $\alpha$  has the same parity as  $\Pi$  and over all odd values otherwise.

It is clear from eq. (2.31), known as the Hauser-Feshbach formula, that the transmission coefficients are independent of  $s$  and  $J$ . This is true only if the optical model potential has no spin dependent terms. If a spin-orbit coupling term is present in the potential, then the transmission coefficients will depend on the angular momentum  $j$  of the projectile ( $\underline{j} = \underline{\ell} + \underline{s}$ ). In this case it is more convenient to change to a coupling scheme where the intrinsic spin of the incident particle  $s$  couples to its orbital angular momentum  $\ell$  to give a total angular momentum  $j$ , which then couples to the intrinsic spin of the nucleus to give the total  $J$ . This presents no problem since the transmission coefficients in the two coupling schemes are related

$$T_{s\ell J}(\alpha) = \sum_j (2j+1) (2S+1) W^2(\ell s J I; j S) T_{\ell j}(\alpha) \quad [2.32]$$

where  $T_{s\ell J}(\alpha)$  are now the transmission coefficients that depend on  $s$  and  $J$  to be used in place of  $T_{\ell}(\alpha)$  of eq. (2.31),  $W$  is the Racah coefficient, and  $T_{\ell j}$  are related to the optical model phase shifts  $\delta_{\ell j}(\alpha)$  by

$$T_{\ell j}(\alpha) = 1 - |e^{2i\delta_{\ell j}(\alpha)}|^2 \quad [2.33]$$





Therefore, with the transformation (2.32) we can still use eq. (2.31) to get the cross section even if the optical potential contains a spin-orbit term.

The cross section given by eq. (2.31) is, of course, the total cross section, i.e., angle integrated. The differential cross section may be derived from somewhat more complicated calculations involving Racah algebra; the explicit form is given in many books and articles (e.g. Vo 68).

Inspection of eq. (2.31) indicates that if the angular momenta and parities involved in the different reaction channels are known, then the numerical calculation of the CN cross section requires only a knowledge of the respective transmission coefficients, and these, as we have seen, are determined by the diagonal elements of the direct part of the S-matrix. In practice, the parameters of an appropriate optical model are determined from an optimum fit to DI elastic scattering data. Once the potential is determined, one can solve Schrödinger's equation with such a potential to get the phase shifts.



## 2.4 The Width-Fluctuation Correction

In cases where the CN levels are non-overlapping and only a few channels are open, the HF formula is not sufficiently accurate mainly because the HF theory inherently presupposes constancy in the partial widths of the CN levels. This may be brought out more clearly by derivation of the formula of the CN cross section by averaging over all the CN resonances, using the Briet-Wigner formula (La 57).

If the Briet-Wigner single level formula is integrated over the energy region around the resonance, and averaged over the resonances of the same spin in the region of excitation covered by the energy spread of the incident beam, one gets (neglecting interference between neighboring CN levels) (Mo 64)

$$\langle \sigma_{\alpha\alpha'}^{\text{CN}} \rangle = \frac{\pi}{k_{\alpha}^2} \sum_{\alpha\alpha'} \frac{(2J+1)}{(2s+1)(2I+1)} \frac{2\pi}{D_{J\Pi}} \left\langle \frac{\Gamma_{\mu\alpha} \Gamma_{\mu\alpha'}}{\Gamma_{\mu}} \right\rangle_{\mu(J\Pi)} \quad [2.34]$$

where  $D_{J\Pi}$  is the mean level spacing of resonances with angular momentum  $J$  and parity  $\Pi$ , the total width  $\Gamma_{\mu}$  in the denominator is the sum over all competing partial widths  $\Gamma_{\mu} = \sum_{\alpha''} \Gamma_{\mu\alpha''}$ , and  $\langle \rangle_{\mu(J\Pi)}$  denotes an average over resonances  $\mu$  with angular momentum  $J$  and parity  $\Pi$ .

To put this expression into a form comparable to the HF formula (eq. 2.31) we use the following expression for the transmission coefficient (Mo 64)



$$T_{\alpha} \approx \frac{2\pi}{D_{J\Pi}} \langle \Gamma_{\mu\alpha} \rangle_{\mu} (J\Pi) \quad \text{if } \langle \Gamma_{\mu\alpha} \rangle \ll D \quad [2.35]$$

The HF formula follows from eqs. (2.34), (2.35) if one sets

$$\left\langle \frac{\Gamma_{\mu\alpha} \Gamma_{\mu\alpha'}}{\Gamma_{\mu}} \right\rangle = \frac{\langle \Gamma_{\mu\alpha} \rangle \langle \Gamma_{\mu\alpha'} \rangle}{\langle \Gamma_{\mu} \rangle} \quad [2.36]$$

It is then apparent that the HF formula ignores the effect of fluctuations of CN level widths about their average values. This cannot be a good assumption even if widths in different channels are completely independent, because fluctuations in the numerator are correlated to fluctuations in the denominator. Each term in the HF formula should be multiplied by a correction factor of the form

$$W_{\alpha\alpha'} = \left\langle \frac{\Gamma_{\mu\alpha} \Gamma_{\mu\alpha'}}{\Gamma_{\mu}} \right\rangle / \frac{\langle \Gamma_{\mu\alpha} \rangle \langle \Gamma_{\mu\alpha'} \rangle}{\langle \Gamma_{\mu} \rangle} \quad [2.37]$$

This width fluctuation correction can be evaluated as a function of the average values  $\langle \Gamma_{\mu\alpha} \rangle$  from knowledge of the form of the statistical distribution of the widths about their average values. A useful form is the Porter-Thomas distribution (Po 56)

$$P(y) dy = (2\pi y)^{-\frac{1}{2}} e^{-y/2} dy \quad [2.38]$$

where  $y = \Gamma_{\alpha} / \langle \Gamma_{\alpha} \rangle$ . For this distribution  $W_{\alpha\alpha'}$  can be expressed as a definite integral. Writing  $W_{\alpha\alpha'}$  in terms of T's, instead of





$\Gamma$ 's, one obtains (Mo 61)

$$W_{\alpha\alpha'} = (1 + 2\delta_{\alpha\alpha'}) \left( \sum_{\alpha''} T_{\alpha''} \right) \int_0^{\infty} (1 + 2yT_{\alpha})^{-1} (1 + 2yT_{\alpha'})^{-1} \\ \times \prod_{\alpha''} (1 + 2yT_{\alpha''})^{-\frac{1}{2}} dy \quad [2.39]$$

This integral can be evaluated analytically only for  $\alpha'' \leq 2$  but if  $\alpha'' > 2$  it can be evaluated numerically. With very few open channels  $W_{\alpha\alpha'}$  may be as small as one-half for  $\alpha \neq \alpha'$  (i.e. inelastic scattering) but as large as three for  $\alpha = \alpha'$  (elastic scattering), but it rapidly approaches unity when the number of channels becomes large (Mo 64a, Vo 68).



## CHAPTER III

### THE SMALL SAMPLE METHOD FOR INVESTIGATION OF THE $(n,n'\gamma)$ REACTION

#### 3.1 Experimental Method

The experimental arrangement is shown in fig. 3.1. Neutrons were produced using the  ${}^7\text{Li}(p,n){}^7\text{Be}$  reaction. A metallic  ${}^7\text{Li}$  target on a 0.254 cm thick Ta backing was bombarded with 0.5 ns proton pulses from the 6 MV van de Graaff accelerator in conjunction with the Mobley magnet bunching system. The average beam intensity was 1  $\mu\text{A}$  during the course of the experiment; the beam spot size was approximately 0.2 cm in diameter. To reduce background from surrounding materials, the end of the proton beam tube was made of nylon with a gold inner lining. In order to ensure that the proton beam was always positioned on the same target spot during the experiment, the beam was passed through a pre-target slit system. It consisted of two gold plates independently mounted on two micrometers and connected to two microammeters. A negative bias of 300 V was applied to each plate to prevent secondary electrons from leaving the target. The Mobley magnet current was adjusted during the experiment to ensure a balanced minimum current on the plates.

The scatterer, placed immediately behind the Ta backing, consisted of 3.147 g of natural Fe in the form of a disc, 1.584 cm in diameter and 0.204 cm thick.

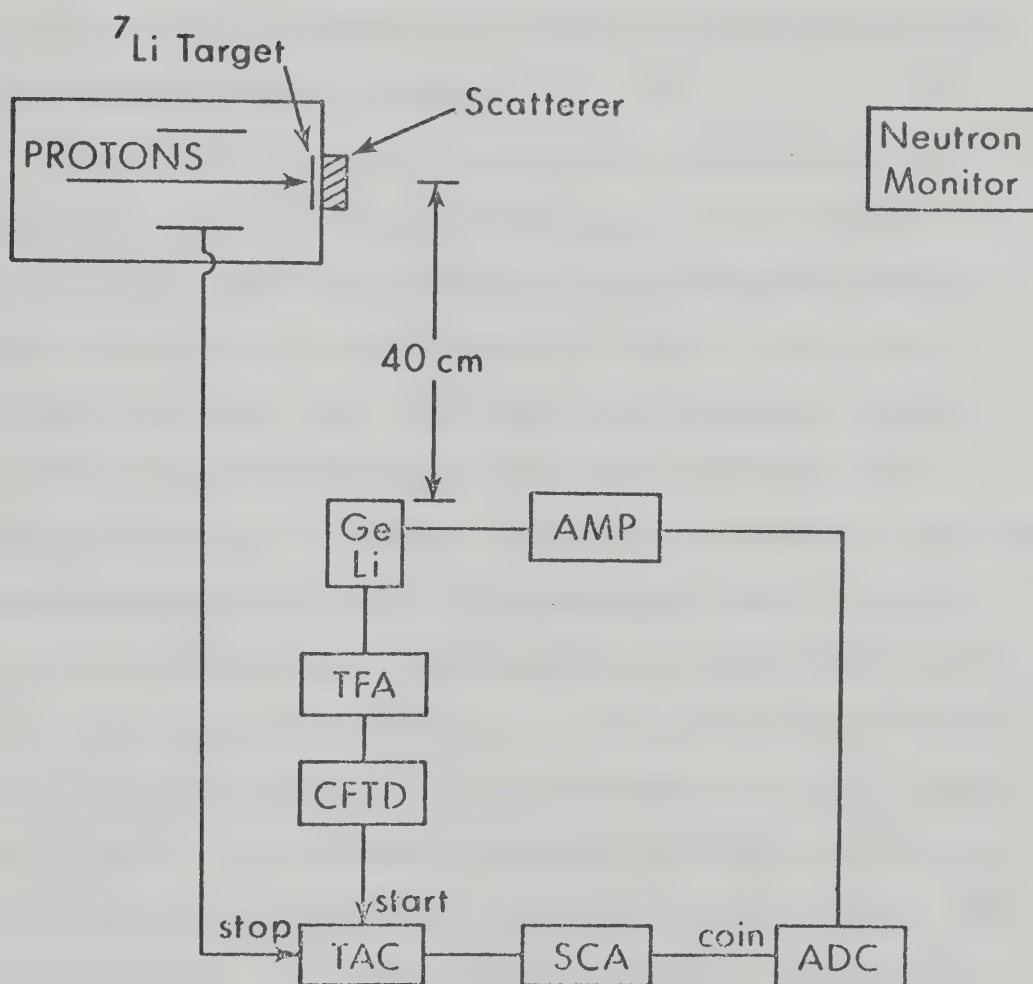
Gamma rays were detected in a 48 cm<sup>3</sup> Ge(Li) detector placed





Figure 3.1 Schematic diagram of the experimental set-up.







40 cm from the scatterer at an angle of  $90^\circ$  with respect to the incident proton beam. Since the detector itself is sensitive to fast neutrons, it is necessary to discriminate against background  $\gamma$ -rays resulting from neutron interactions with the Ge(Li) crystal and the surrounding materials. The technique adopted utilizes the timing capability of the detector.

Signals from the Ge(Li) detector were used to obtain both energy and timing information. Timing signals were extracted using a timing filter amplifier (TFA) and a constant-fraction timing discriminator (CFTD) and provided the start signal for the time-to-amplitude converter (TAC). The stop signal was derived from a cylindrical capacitive time pick-off placed in the beam tube immediately ahead of the target. Due to the difference in velocities between neutrons and  $\gamma$ -rays the corresponding signals triggered the TAC at different times. Consequently the output signals of the TAC were essentially sorted out into two groups separated by the time difference between the arrival of neutrons and  $\gamma$ -rays to the Ge(Li) crystal. The scatterer-to-detector distance was sufficient to yield a good time separation between neutrons and  $\gamma$ -rays in the TAC time spectrum. To reduce background  $\gamma$ -rays a single-channel analyser (SCA) was used to set a window on the  $\gamma$ -peak of the time spectrum. The SCA output signals were then used to gate the energy signals; both were fed to an amplitude-to-digital converter (ADC) running in a coincidence mode and interfaced to a Honeywell 316 on-line computer.



The neutron flux was monitored by a fixed position Ne 213 neutron detector employing time-of-flight techniques. The neutron spectrometer has previously been described in detail (El 69).

Gamma ray spectra from the  $^{56}\text{Fe}(n,n'\gamma)$  reaction were obtained at maximum neutron energies ranging from 0.89 to 1.92 MeV. The corresponding energies of protons falling on the Li target range from 2.60 to 3.60 MeV. "Scatterer-in" and "scatterer-out" runs were made at each energy for a predetermined charge collected on target. Peak areas of the 847 keV  $\gamma$ -ray were extracted from the gated  $\gamma$ -ray spectra. At each energy the intensity of the ground state neutron group of the  $^7\text{Li}(p,n)^7\text{Be}$  reaction was also extracted from the neutron monitor spectrum.

The efficiency of the Ge(Li) detector was determined using calibrated  $\gamma$ -ray sources (Ro 72), and the neutron detection efficiency was calculated using a Monte Carlo routine (see Appendix A).

### 3.2 Data Reduction

The quantity measured experimentally is the yield  $Y_\gamma(E_p, \psi_\gamma)$  for a particular  $\gamma$ -ray at a proton energy  $E_p$  and observation angle  $\psi_\gamma$  with respect to the proton beam. It is desirable to describe this yield in terms of a  $\gamma$ -ray differential production cross section at an effective neutron energy. Because of the nature of the experimental arrangement, this description must explicitly take into account the effect due to averaging the neutron energy and flux variation over the scatterer geometry.



Neutrons produced by the  ${}^7\text{Li}(p,n){}^7\text{Be}$  reaction are considered to come from a point source placed at the centre of a circular disc of radius  $R$  and thickness  $T$ . The  $\gamma$ -yield for a particular  $\gamma$ -ray is given by:

$$Y_{\gamma}(E_p, \psi_{\gamma}) = N_s \epsilon_{\gamma} \int_V [I_n(E_p, \theta_n)] \left[ \frac{d\sigma_{\gamma}}{d\Omega}(E_n, \theta_{\gamma}) \right] \cdot [\exp(-\mu_{\gamma} \ell_{\gamma})] dV \quad [3.1]$$

where  $N_s$  is the number of scatterer nuclei per unit volume in the sample,  $\epsilon_{\gamma}$  is the total efficiency of the  $\gamma$ -detector including the solid angle,  $I_n(E_p, \theta_n)$  is the neutron intensity ( $\text{cm}^{-2} \text{s}^{-1}$ ) in the volume element  $dV$  at a proton energy  $E_p$  and neutron emission angle  $\theta_n$  with respect to the proton beam,  $\frac{d\sigma_{\gamma}}{d\Omega}(E_n, \theta_{\gamma})$  is the differential production cross section for the  $\gamma$ -ray of interest at a neutron energy  $E_n$  and angle  $\theta_{\gamma}$  with respect to the neutron direction,  $\mu_{\gamma}$  is the  $\gamma$ -absorption coefficient and  $\ell_{\gamma}$  is the distance in the sample through which the  $\gamma$ -ray has to pass. The integration extends over "the active volume" of the scatterer which will be defined later.

The first step is to calculate  $I_n(E_p, \theta_n)$ . This must take into account the angular distribution and attenuation of neutrons in the scatterer. The  ${}^7\text{Li}(p,n){}^7\text{Be}$  reaction yields two neutron groups,  $n_0$  and  $n_1$ , leading to the ground and first excited states of  ${}^7\text{Be}$ , respectively. For simplicity we will neglect in the following derivation the small contribution to the neutron intensity from the  $n_1$  group. The differential cross section for the  ${}^7\text{Li}(p, n_0){}^7\text{Be}$





reaction can be described in terms of a Legendre polynomial series (see Appendix A):

$$\frac{d\sigma_n}{d\Omega}(E_p, \theta_n) = \sum_{i=0}^3 A_i(E_p) P_i(\cos \theta_n) \quad [3.2]$$

If the neutron source is considered to be at the origin of a cylindrical coordinate system with the proton beam in the z-direction (fig. 3.2a), then  $I_n$  is given by:

$$I_n(E_p, \theta_n) = N_{Li} N_p \left[ \sum_{i=0}^3 A_i(E_p) P_i(\cos \theta_n) \right] \frac{1}{\rho^2 + z^2} \quad [3.3]$$

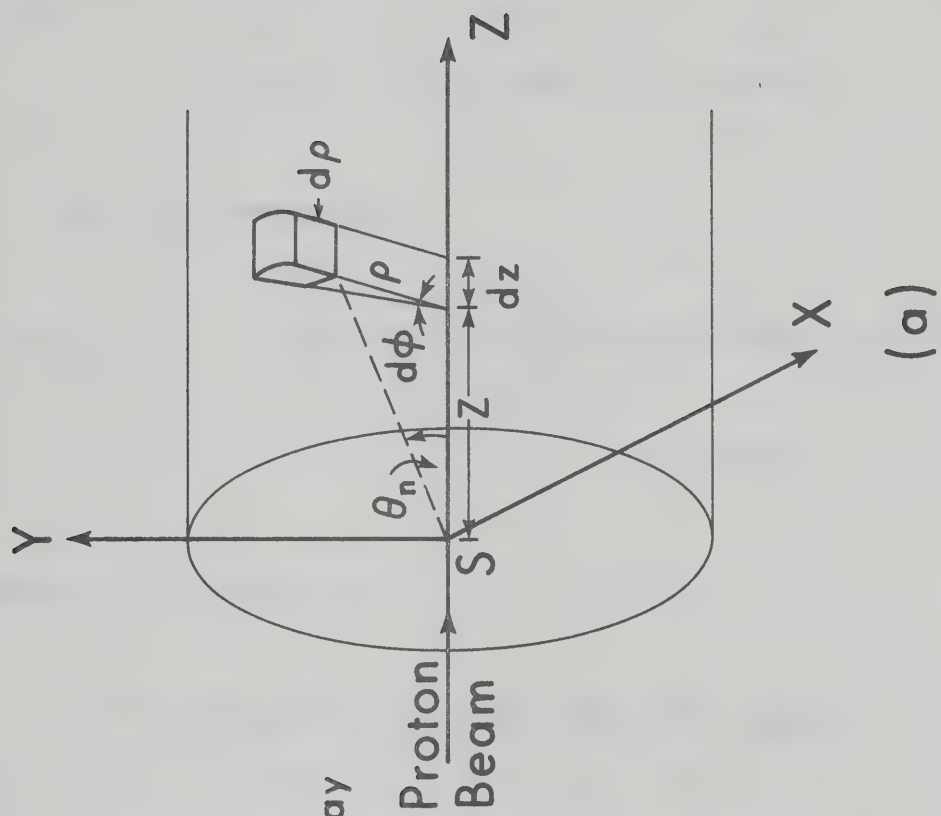
where  $N_{Li}$  is the number of  ${}^7\text{Li}$  nuclei per  $\text{cm}^2$ ,  $N_p$  is the number of protons falling on this target per second and  $\theta_n = \tan^{-1}(\rho/z)$ . Due to the small size of the sample, neutron attenuation is expected to be small. However, it can be accounted for in the determination of the factor  $N_{Li} N_p$  as described below.

Attenuation of  $\gamma$ -rays in the scatterer must be calculated explicitly because typical  $\gamma$ -ray absorption lengths are comparable to the scatterer dimensions. The expression for the  $\gamma$ -ray path through the scatterer,  $\ell_\gamma$ , can be determined with the aid of fig. 3.2b. In the present experimental arrangement, where  $\psi_\gamma = 90^\circ$  and the scatterer-to-detector distance is large compared to the sample dimensions, the  $\gamma$ -rays emitted within the solid angle of the detector are essentially perpendicular to the z-axis. Thus  $\ell_\gamma$  is independent

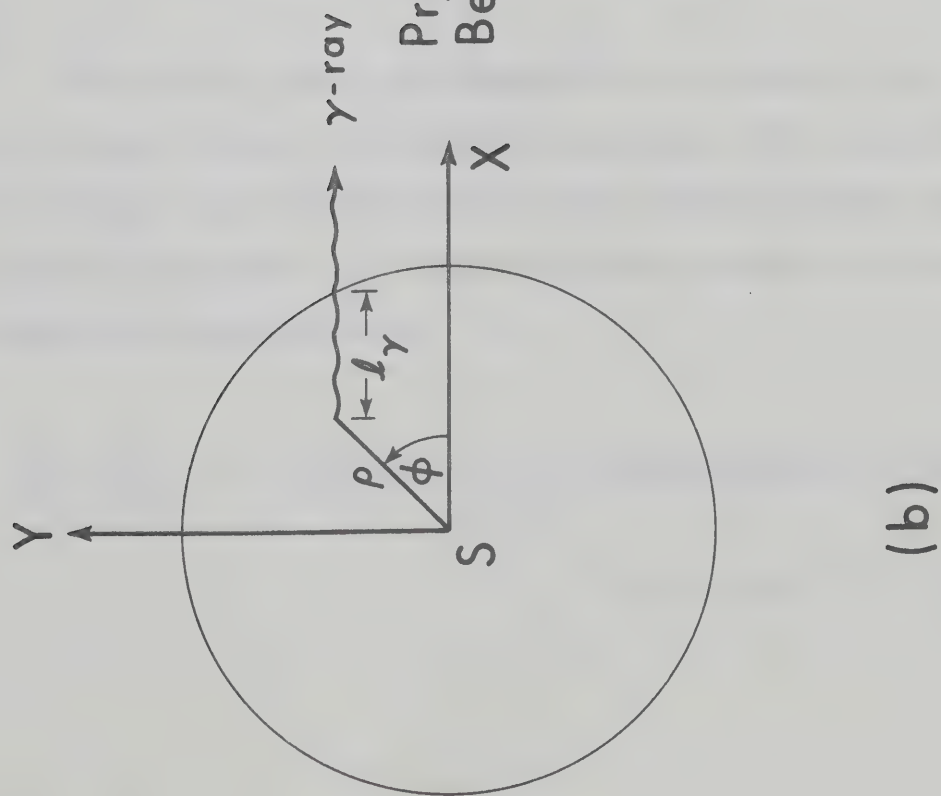




- Figure 3.2
- (a) Schematic drawing of a cylindrical scatterer and a point source located at S.
  - (b) Front-view of the scatterer with the z-axis perpendicular to the plane of the page and passing through the neutron source.



(a)



(b)





of  $z$  and is given by

$$l_{\gamma}(\rho, \phi) = [R^2 - \rho^2 \sin^2 \phi]^{\frac{1}{2}} - \rho \cos \phi \quad [3.4]$$

Eq. (3.1) then becomes

$$Y_{\gamma}(E_p, \psi_{\gamma}) = C \int \{ [I'_n(A_i; \rho, z)] \cdot \left[ \frac{d\sigma_{\gamma}}{d\Omega}(E_n, \theta_{\gamma}) \right] \cdot [\exp(-\mu_{\gamma} l_{\gamma}(\rho, \phi))] \} \rho \, d\rho \, d\phi \, dz \quad [3.5]$$

where  $C = N_{Li} N_p N_s \epsilon_{\gamma}$ ,

$$I'_n(A_i; \rho, z) = \left[ \sum_{i=0}^3 A_i p_i (\cos \theta_n) \right] \frac{1}{\rho^2 + z^2}$$

Since both  $E_n$  and  $\theta_{\gamma}$  are dependent on the value of  $\rho/z$ , it is clear from eq. (3.5) that the measured  $\gamma$ -yield represents an average over both the neutron energy spread and the  $\gamma$ -ray angular distribution. It is then possible to define this average production cross section as

$$\overline{\frac{d\sigma}{d\Omega}}(E_n, \psi_{\gamma}) = [Y_{\gamma}(E_p, \psi_{\gamma})] \{ C \int [I'_n(A_i; \rho, z)] [\exp(-\mu_{\gamma} l_{\gamma}(\rho, \phi))] \rho \, d\rho \, d\phi \, dz \}^{-1} \quad [3.6]$$



This average differential cross section is associated with an "effective" neutron energy  $\bar{E}_n$  defined by

$$\bar{E}_n = \left\{ \int [I'_n(A_i; \rho, z)] \cdot [\sigma_{n,n'}(E_n)] \cdot [E_n(\rho, z)] \rho d\rho dz \right\} \\ \times \left\{ \int [I'_n(A_i; \rho, z)] \cdot [\sigma_{n,n'}(E_n)] \rho d\rho dz \right\}^{-1}, \quad [3.7]$$

where  $\sigma_{n,n'}(E_n)$  is a function that describes the dependence of the inelastic cross section on energy. It is taken to be (B1 52)

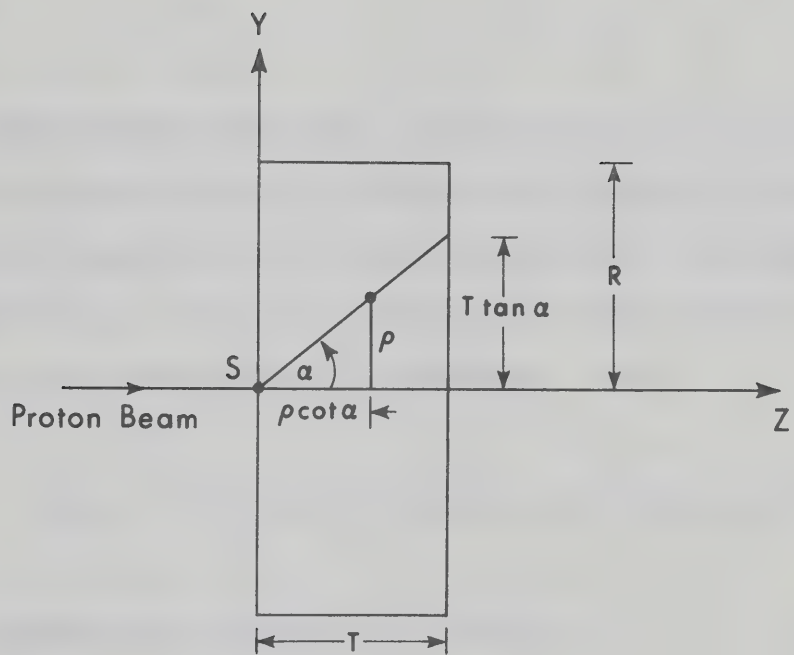
$$\sigma_{n,n'}(E_n) \propto (E_n - E_{th})^{\frac{1}{2}} \quad [3.8]$$

The limits of integration over the  $\rho$  and  $z$  variables can be determined in the following manner. For a proton energy  $E_p$ , let  $E_n^{\max}$  be the neutron energy at  $0^\circ$  and  $E_n^{th}$  be the neutron threshold energy for the level decaying by the particular  $\gamma$ -ray of interest. If  $\alpha$  is the angle that corresponds to  $E_n^{th}$ , then only neutrons emerging in the cone  $\alpha$  will have enough energy to produce that  $\gamma$ -ray. This cone will define what we called "the active volume" of the scattering sample. The angle  $\alpha$  can be calculated for a particular level at each proton energy from the kinematics of the  ${}^7\text{Li}(p, n_0){}^7\text{Be}$  and the  $(n, n')$  reactions. A maximum value of  $\pi/2$  is used for  $\alpha$  since backward-angle neutrons will not interact with the scatterer. Referring to fig. 3.3, the limits of integration are:





Figure 3.3 Side-view of the scatterer indicating the limits of integration over  $\rho$  and  $z$  variables.







Variable	Lower limit	Upper limit
$\rho$	0	or $\frac{T \tan \alpha}{R}$ if $\alpha \leq \tan^{-1} R/T$ if $\alpha > \tan^{-1} R/T$
$z$	$\rho \cot \alpha$	$T$
$\phi$	0	$2\pi$

The integration over the  $z$ -variable in eq. (3.6) can be carried out analytically (see Appendix B), whereas the integrations over  $\rho$  and  $\phi$  have to be done numerically. The double integral of eq. (3.7) can be reduced to a single one over the angle  $\theta_n$  by using spherical coordinates. Thus

$$\bar{E}_n(E_p) = \left[ \int_0^\alpha f(\theta_n) E_n(\theta_n) d\theta_n \right] \times \left[ \int_0^\alpha f(\theta_n) d\theta_n \right]^{-1} \quad [3.9]$$

with the weighting function  $f(\theta_n)$  given by

$$f(\theta_n) = \frac{d\sigma_n}{d\Omega}(E_p, \theta_n) \cdot \ell_n(\theta_n) \cdot \sin\theta_n \cdot \sigma_{n,n'}(E_n) \quad [3.10]$$

where  $\ell_n(\theta_n)$  is the distance travelled by a neutron emitted at an angle  $\theta_n$ . The function  $f(\theta_n)$  represents the number of interactions occurring at neutron energy  $E_n$ .

Since the differential cross section given by eq. (3.6) "averages over the  $\gamma$ -ray angular distribution", the total cross sections can be obtained from the relation:

$$\bar{\sigma}_\gamma(\bar{E}_n) = 4\pi \overline{\frac{d\sigma_\gamma}{d\Omega}}(\bar{E}_n, \psi_\gamma) \quad [3.11]$$



A computer program was written to manipulate the raw data according to the above formulation (E172). The average differential production cross sections and effective neutron energies were calculated using eqs. (3.6) and (3.8), respectively. Legendre polynomial expansion coefficients for the  ${}^7\text{Li}(p,n_0){}^7\text{Be}$  reaction were obtained from a separate experiment (Appendix A). A correction for the small contribution from neutrons leading to the first excited state of  ${}^7\text{Be}$  was included in the determination of neutron intensity. The product  $N_{\text{Li}} N_p$  was obtained for each run from the yield of the  $n_0$  group observed in the neutron monitor detector and the known  ${}^7\text{Li}(p,n_0){}^7\text{Be}$  cross section. The neutron yield was corrected for detection efficiency and attenuation in the sample. The ratio of the  $n_0$  yield in two consecutive runs with and without the scatterer provided the attenuation factor.

Experimental errors for the average differential cross sections evolve from uncertainties in the determination of the following quantities:

- (i) peak areas of  $\gamma$ -rays and neutrons
- (ii) detection efficiency for  $\gamma$ -rays and neutrons
- (iii) cross sections for the  ${}^7\text{Li}(p,n){}^7\text{Be}$  reaction
- (iv) number of scattering nuclei
- (v)  $\gamma$ -ray absorption coefficients and neutron attenuation
- (vi) integration over scatterer geometry.

The overall errors in absolute differential cross sections were estimated to be  $\leq 25\%$ .

For the total cross section obtained from eq. (3.11), an additional error arises from the assumption that the present



geometrical arrangement averages over the  $\gamma$ -ray angular distribution. In order to estimate this error, let us write the differential cross section as:

$$\frac{d\sigma_{\gamma}}{d\Omega}(E_n, \theta_{\gamma}) = A_0 [1 + a_2 p_2(\cos \theta_{\gamma})] \quad [3.12]$$

The above assumption implies that the integration of the second term of this equation over the scatterer geometry is negligible. To show that this is true the following integration was carried out:

$$I = \left[ \int f(\theta_{\gamma}) p_2(\cos \theta_{\gamma}) d\theta_{\gamma} \right] \cdot \left[ \int f(\theta_{\gamma}) d\theta_{\gamma} \right]^{-1} \quad [3.13]$$

where  $f(\theta_{\gamma})$  is the corresponding  $f(\theta_n)$  as given by eq. (3.9).

The limits of integration were set according to the range of  $\theta_n$  as determined by the angle  $\alpha$  of the neutron cone. It was found that the maximum value of  $I = -0.17$  for  $E_n^{\max} = 100$  keV above threshold and rapidly decreases to 0.01 with increasing energy. Assuming a value of 1.0 for  $a_2$  the total cross section might be subjected to a maximum systematic error of 17% just above threshold.

### 3.3 Experimental Results

The timing characteristics of the  $\gamma$ -ray spectrometer are indicated in the time-spectrum shown in fig. 3.4. The effect of the electronic time window on the observed  $\gamma$ -ray spectrum is



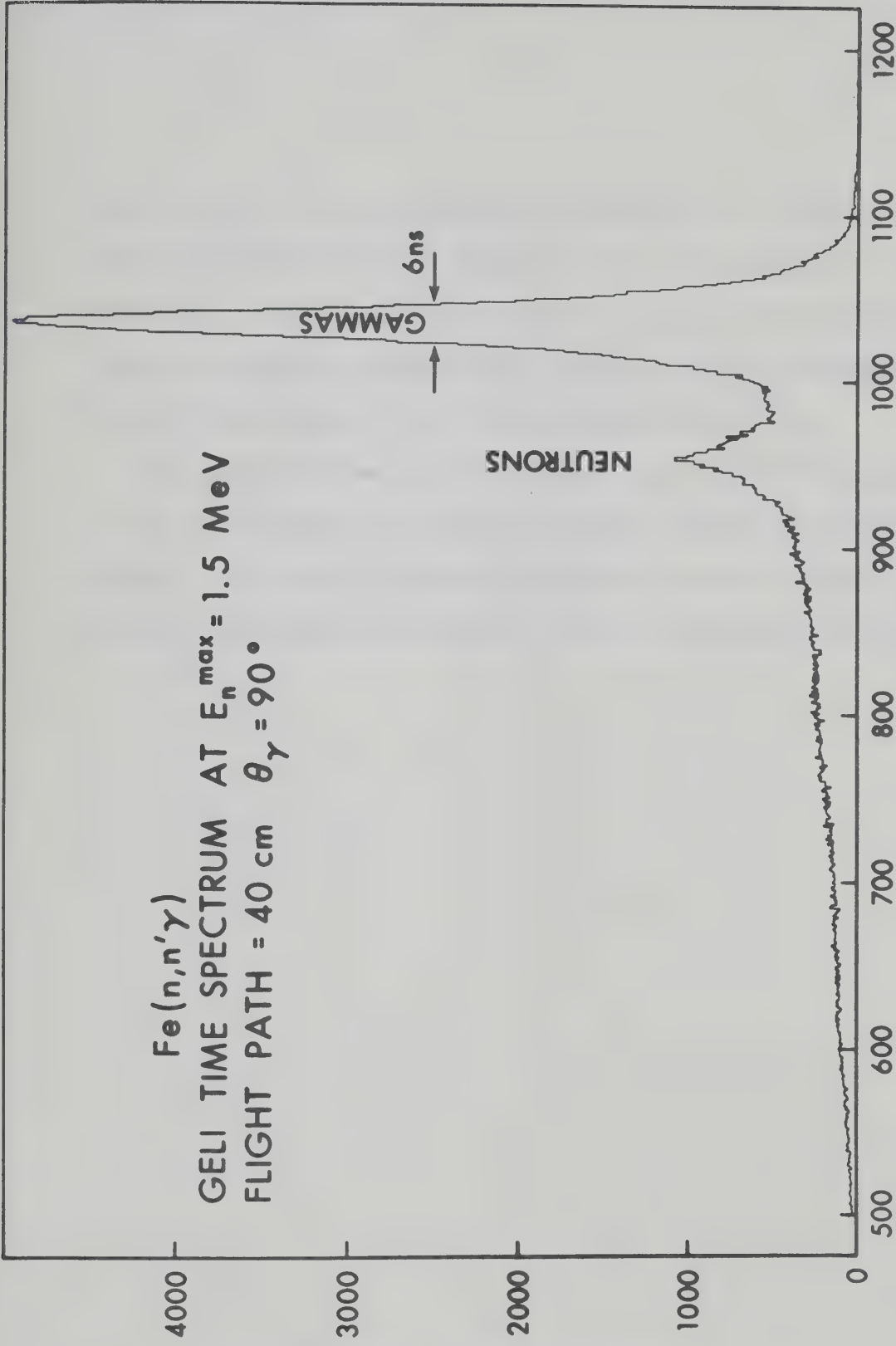




Figure 3.4 Time spectrum from the TAC associated with the Ge(Li) detector (see fig. 3.1).

$\text{Fe}(n,n'\gamma)$   
GELI TIME SPECTRUM AT  $E_n^{\text{max}} = 1.5 \text{ MeV}$   
FLIGHT PATH = 40 cm  $\theta_\gamma = 90^\circ$

COUNTS PER CHANNEL



CHANNEL NUMBER



shown in fig. 3.5. The suppression of events due to time-uncorrelated room background and neutron induced events in the detector is quite effective. The 431 and 478 keV  $\gamma$ -rays are due to the  ${}^7\text{Li}(p,n\gamma)$  and  ${}^7\text{Li}(p,p'\gamma)$  reactions, respectively; the 847 keV  $\gamma$ -ray corresponds to the well-known decay of the first excited state of  ${}^{56}\text{Fe}$ .

The excitation curve of the 847 keV  $\gamma$ -ray from  ${}^{56}\text{Fe}$  is shown in fig. 3.6, together with previous results obtained by conventional methods. It is quite clear that the present source-scatterer geometry performs a good energy average and yields reliable cross sections.





Figure 3.5       $\text{Fe}(n,n'\gamma)$  spectrum obtained in a 51 min. run. The gated and ungated spectra were collected simultaneously. Peaks are labelled by their corresponding  $\gamma$ -ray energies in keV and the material from which they originate.

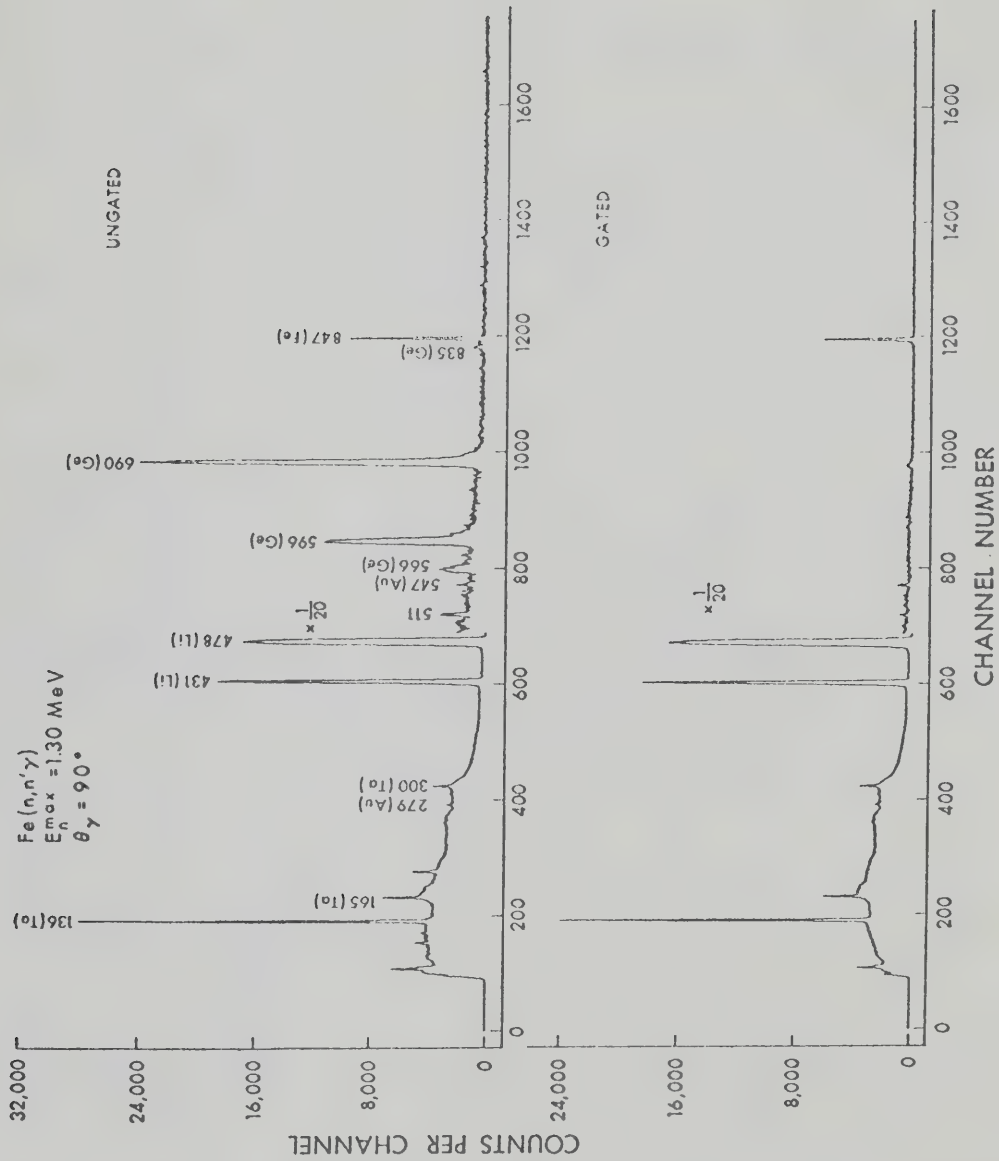
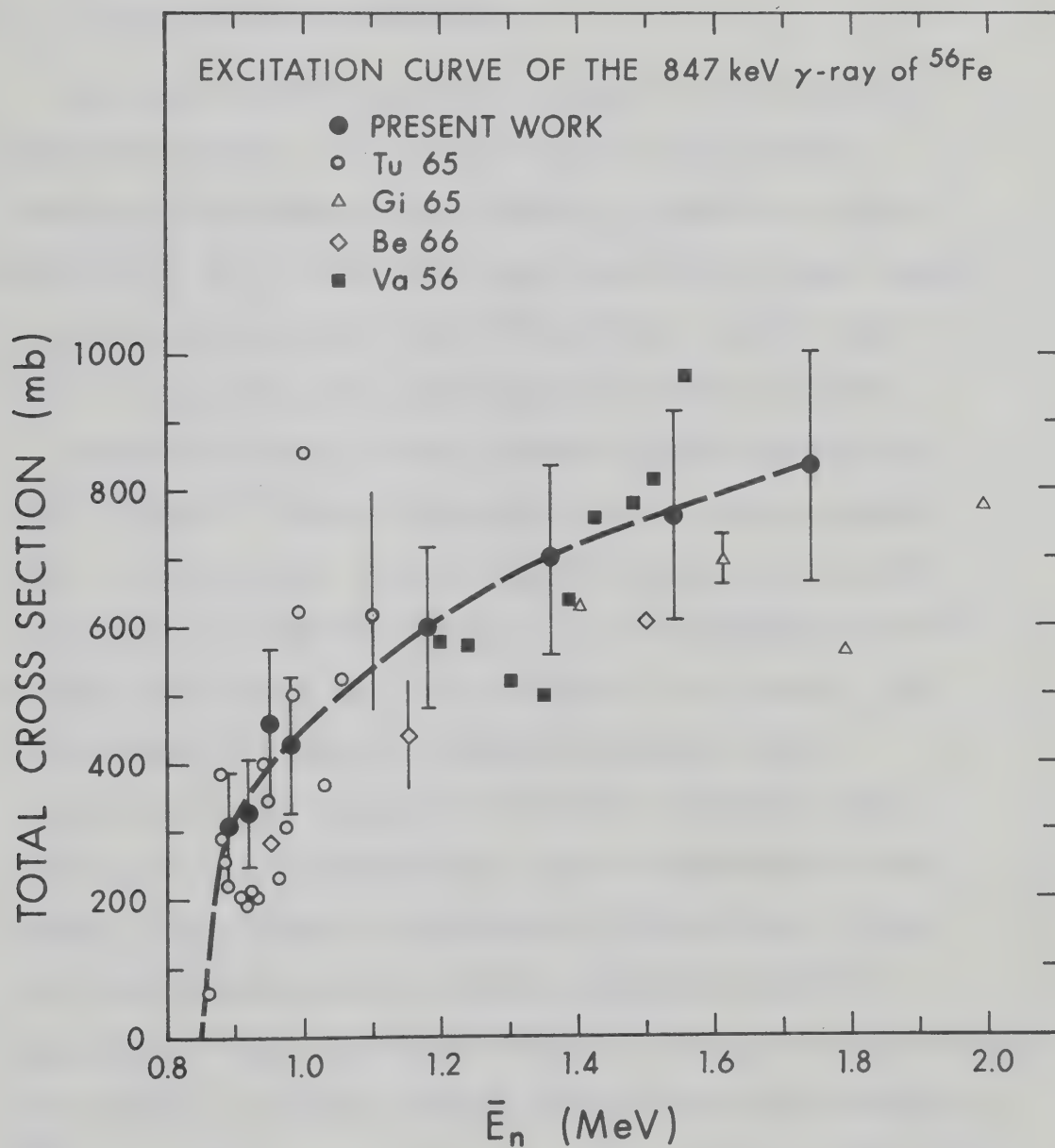








Figure 3.6      Excitation curve for the 847 keV  $\gamma$ -ray from  $^{56}\text{Fe}$ .  
The average total cross section is plotted against  
the effective neutron energy. Error bars represent  
absolute errors. Previous results of the conven-  
tional technique are also shown.





## CHAPTER IV

### APPLICATIONS: STUDY OF LEVELS IN $^{154}\text{Sm}$ AND $^{160}\text{Gd}$ NUCLEI

#### 4.1 Experiment and Data Reduction

The experimental arrangement described in § 3.1 was used. Scattering materials were obtained from Oak Ridge National Laboratory in the form of  $\text{Sm}_2\text{O}_3$  and  $\text{Gd}_2\text{O}_3$  powders enriched to 99.54 and 95.95% in  $^{154}\text{Sm}$  and  $^{160}\text{Gd}$ , respectively. These powders have been compressed into a solid disc inside a nylon ring. Table 4.1 gives the weight and dimensions of both scatterers.

Gamma-ray spectra following neutron inelastic scattering from  $^{154}\text{Sm}$  and  $^{160}\text{Gd}$  were obtained at maximum neutron energies from 1.10 to 2.32 MeV. At each energy three separate runs were made: (i) a run with the scatterer (ii) a background run with an empty nylon ring, and (iii) a run with an Fe sample. The Fe run served as a check on cross section normalization.

"Scatterer-out" runs were used to identify background  $\gamma$ -rays observed in the time-gated spectra due to contaminant reactions created in the immediate surroundings of the scatterer. After normalizing "scatterer-out" runs and subtracting them from "scatterer-in" runs, spectra due entirely to the scattering material were obtained. A typical spectrum obtained with the Gd scatter at  $E_n^{\text{max}} = 1.71$  MeV is shown in fig. 4.1. These runs were taken with a wider time gate admitting some of the  $\gamma$ -rays generated in the  $\text{Ge(Li)}$



TABLE 4.1  
Weight and dimensions of scatterers

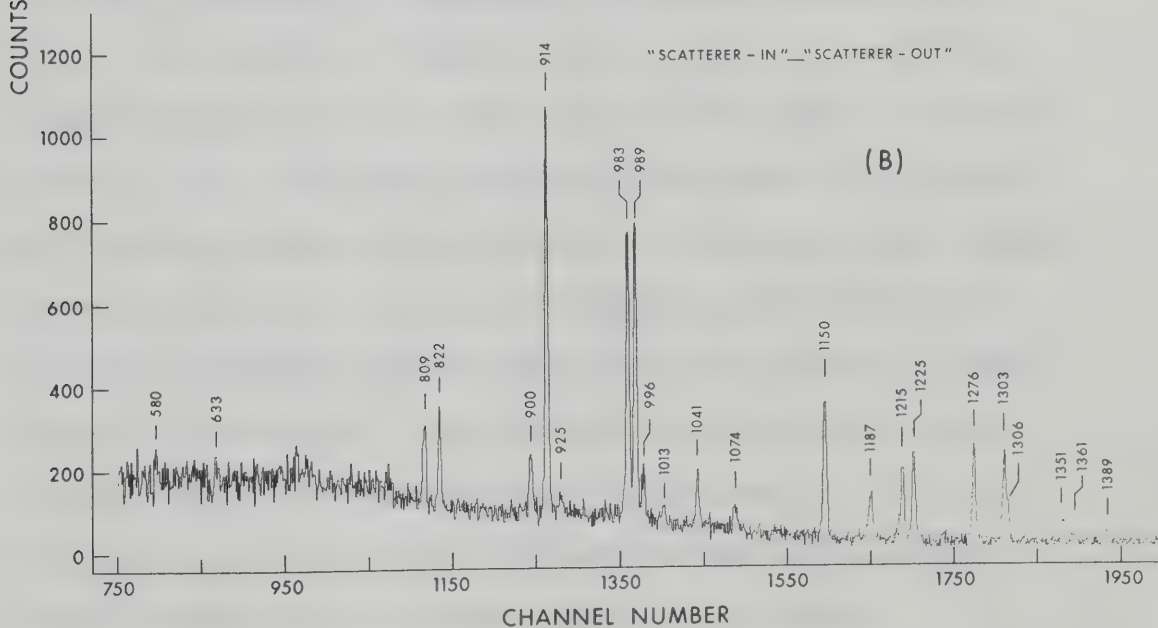
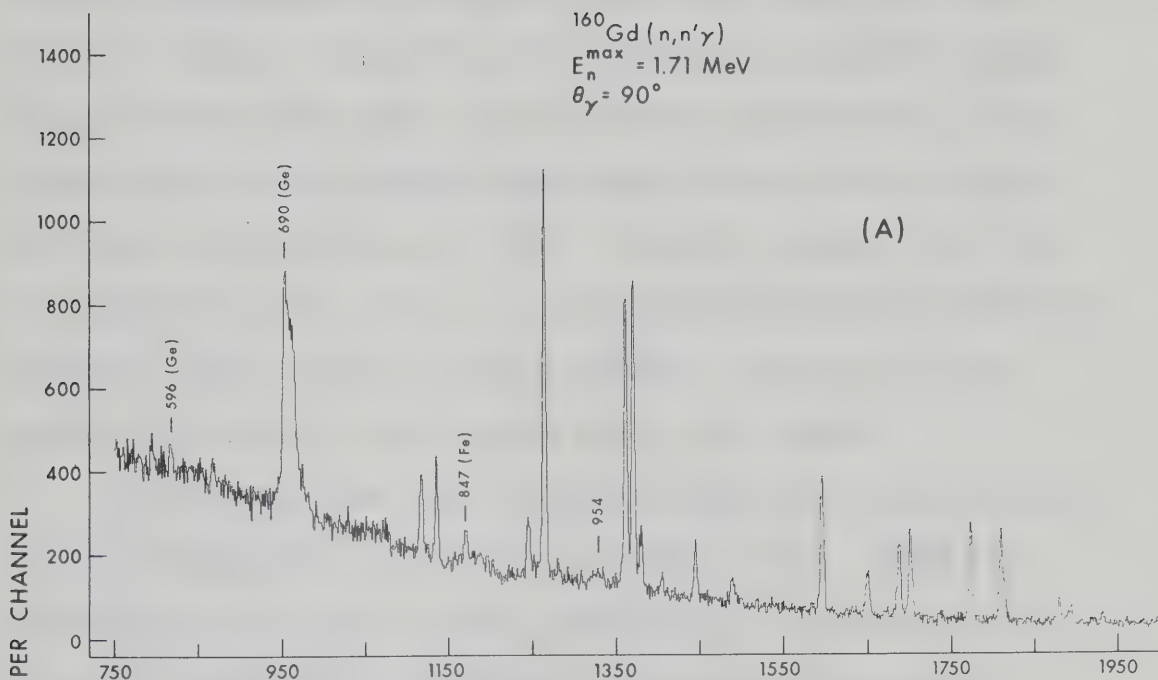
Material	Diameter (cm)	Thickness (cm)	Weight ( g )
$\text{Sm}_2\text{O}_3$ (99.54% enriched in $^{154}\text{Sm}$ )	1.58	1.63	6.96
$\text{Gd}_2\text{O}_3$ (95.95% enriched in $^{160}\text{Gd}$ )	1.58	0.56	3.46







- Figure 4.1
- (a)  $^{160}\text{Gd}(n,n'\gamma)$  spectrum obtained in a 3 hour run. Contaminant peaks are labelled by their energies in keV and, whenever possible, the material from which they originate.
  - (b)  $^{160}\text{Gd}(n,n'\gamma)$  spectrum after subtracting a background run collected for the same neutron flux. The peaks which are labelled by their energies in keV correspond to transitions in  $^{160}\text{Gd}$ .





detector. In fig. 4.1a, the 596 and 690 keV  $\gamma$ -rays are due to neutron interactions with the Ge crystal while the 847 keV  $\gamma$ -ray is due to neutron interaction with Fe materials around the target. None of these lines appear in the subtracted spectrum (fig. 4.1b). Gamma-rays for which energies have been assigned in fig. 4.1b are attributed to transitions in  $^{160}\text{Gd}$ . A similar spectrum for  $^{154}\text{Sm}$  is shown in fig. 4.2. Due to the very high background below 500 keV from the  $^7\text{Li}(p,p'\gamma)$  and  $^7\text{Li}(p,n\gamma)$  reactions, (see fig. 3.5) no quantitative analysis was carried out in this region.

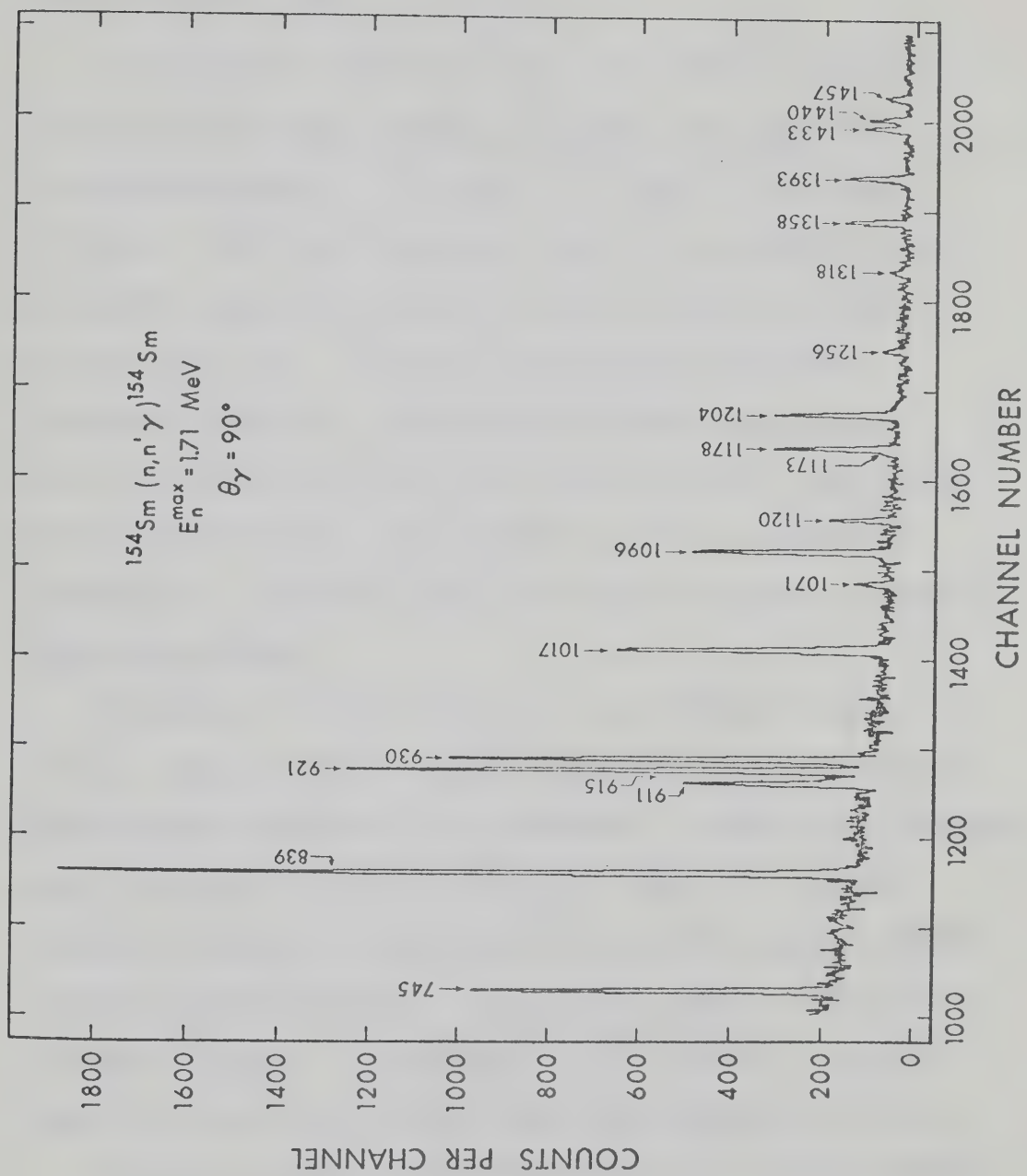
Peak centroids and areas of the observed  $\gamma$ -rays were extracted at each energy using a peak fitting program (Ea 72). Gamma ray energies were obtained from peak centroids and a calibration line that was independently determined using radioactive sources of known  $\gamma$ -ray energies. Production cross sections and effective neutron energies were calculated employing the method of analysis given in § 3.2. The  $\gamma$ -ray absorption coefficients for  $\text{Sm}_2\text{O}_3$  and  $\text{Gd}_2\text{O}_3$  were estimated using the tables of Davison and Evans (Da 52). Branching ratios for  $\gamma$ -rays associated with a particular level have been determined from the production cross sections of these  $\gamma$ -rays at all energies. The inelastic cross section for a given level was obtained by summing the cross sections for all  $\gamma$ -rays originating at this level and subtracting from this value the cross sections for all cascades feeding this level.







Figure 4.2  $^{154}\text{Sm}(n,n'\gamma)$  spectrum after subtracting a background run collected for the same neutron flux. The peaks which are labelled by their energies in keV correspond to transitions in  $^{154}\text{Sm}$ .





## 4.2 Statistical Theory Calculations

As mentioned in Chapter II, the cross sections predicted by the statistical theory represent an average over many levels in the compound nucleus. Since nuclei of interest in this work ( $^{154}\text{Sm}$  and  $^{160}\text{Gd}$ ) have a high mass number, the excitation energy of the CN is then great enough ( $\sim 8$  MeV) so that the density of levels is large. In addition, the present experimental arrangement utilizes a neutron beam of a wide energy spread, thus resulting in the excitation of many CN levels. Accordingly, the measured inelastic cross sections are energy averages and therefore the statistical theory can safely be applied to predict such cross sections.

The nuclei  $^{154}\text{Sm}$  and  $^{160}\text{Gd}$  fall in the deformed region of nuclei. Thus one would not expect to be able to fit experimental data assuming a spherical optical potential. However, the extensive work of Auerbach and Moore (Au 64) has revealed that one can reproduce, quite well, both elastic and inelastic neutron scattering data on deformed nuclei in the region between Ta and U using a spherical, local, spin-dependent optical potential. Similar results for Ta, Re and Pt were reported by Smith et al. (Sm 68).

A computer code has been written (Sh 72) to calculate neutron transmission coefficients. We have employed a spherical local optical potential of the form



$$U(r) = -V f(r, r_{or}, a_r) + 4i a_i W \frac{d}{dr} [f(r, r_{oi}, a_i)] + \left( \frac{\hbar}{m_\pi c} \right)^2 V_s \frac{1}{r} \frac{d}{dr} [f(r, r_{os}, a_s)] \vec{L} \cdot \vec{\sigma} \quad [4.1]$$

where  $V$ ,  $W$  and  $V_s$  are the depths of the real, imaginary, and spin-orbit wells, respectively, and  $m_\pi$  is the mass of the pion.

$f(r, r_0, a)$  are taken to have the Saxon-Woods shape

$$f(r, r_0, a) = \{1 + \exp [(r - r_0 A^{\frac{1}{3}})/a]\}^{-1}$$

where  $r_0$  and  $a$  are the radius and diffuseness parameters respectively. In what follows, the depths are given in MeV and the geometrical dimensions in fm.

Four "global" sets of potential parameters are available from analysis of neutron data over a substantial energy range and for a series of nuclei. These are:

- (a) Perey and Buck non-local potential (Pe 62) that fits neutron scattering data from 1 to 25 MeV. An equivalent over-all local potential has been obtained by Wilmore and Hodgson (Wi 64); this is specified by the parameters

$$V = 47.01 - 0.267 E - 0.0018 E^2$$

$$r_{or} = 1.322 - 0.00076 A + (4 \times 10^{-6}) A^2 - (8 \times 10^{-9}) A^3$$

$$a_r = 0.66$$

$$W = 9.52 - 0.053 E$$



$$r_{oi} = 1.266 - 0.00037 A + (2 \times 10^{-6}) A^2 - (4 \times 10^{-9}) A^3$$

$$a_i = 0.48$$

$$V_S = 0.0$$

where  $E$  is the incident neutron lab energy in MeV.

- (b) Moldauer potential (Mo 63): The Perey-Buck potential is not able to fit the neutron  $s$ -wave strength function around  $A = 100$ . Moldauer (Mo 63) was able to show that this could be corrected by allowing the absorbing part of the potential to peak sharply just outside the nuclear surface. Analysis of available data for neutrons of energy below 1 MeV led to the potential (given according to the geometry specified in eq. (4.1))

$$V = 46.0 \quad r_{or} = 1.25 \quad a_r = 0.62$$

$$W = 14.0 \quad r_{oi} = 1.38 \quad a_i = 0.24$$

$$V_S = 0.0$$

- (c) Rosen potential (Ro 66): This potential was determined by fitting 14 MeV neutron elastic-scattering data on a wide range of nuclei. It is specified by the following parameters

$$V = 49 - 0.33 E \quad r_{or} = 1.25 \quad a_r = 0.65$$

$$W = 5.75 \quad r_{oi} = 1.25 \quad a_i = 0.7$$

$$V_S = 5.5 \quad r_{os} = 1.25 \quad a_s = 0.65$$

The energy dependence of the real part of the potential was obtained from analysis of proton polarization data at different energies.

- (d) Becchetti and Greenlees potential (Be 69) which was determined from analysis of neutron data for energies  $< 14.5$  MeV and nuclei





with  $A > 40$ . They utilized differential cross sections, polarizations, reaction cross sections and total cross sections and obtained excellent over-all fits. The optimum neutron parameters were found to be (for energies  $\leq 7.1$  MeV)

$$\begin{array}{lll} V = 56.3 - 0.32 E - 24 \frac{N-Z}{A} & r_{or} = 1.17 & a_r = 0.75 \\ W = 13 - 0.25 E - 12 \frac{N-Z}{A} & r_{oi} = 1.26 & a_i = 0.58 \\ V_S = 6.2 & r_S = 1.1 & a_S = 0.75 \end{array}$$

where  $N$  and  $Z$  are the number of neutrons and protons in the nucleus, respectively.

It should be noted that all these potentials yielded a reasonably good overall fit to neutron elastic scattering data down to  $\approx 1$  MeV incident energy, provided that one takes account of compound elastic scattering.

In order to test the sensitivity of inelastic cross sections to these different potential sets, we have compared the measured and calculated cross sections for the 847 keV state of  $^{56}\text{Fe}$  (fig. 4.3). The experimental results are in good agreement with the curves predicted by the potentials (a), (c) and (d) but in poor agreement with that predicted by the potential of Moldauer. Thus, it seems that Moldauer's average potential does not describe iron very well. Similar results were reported by Gilboy and Towle (Gi 65).

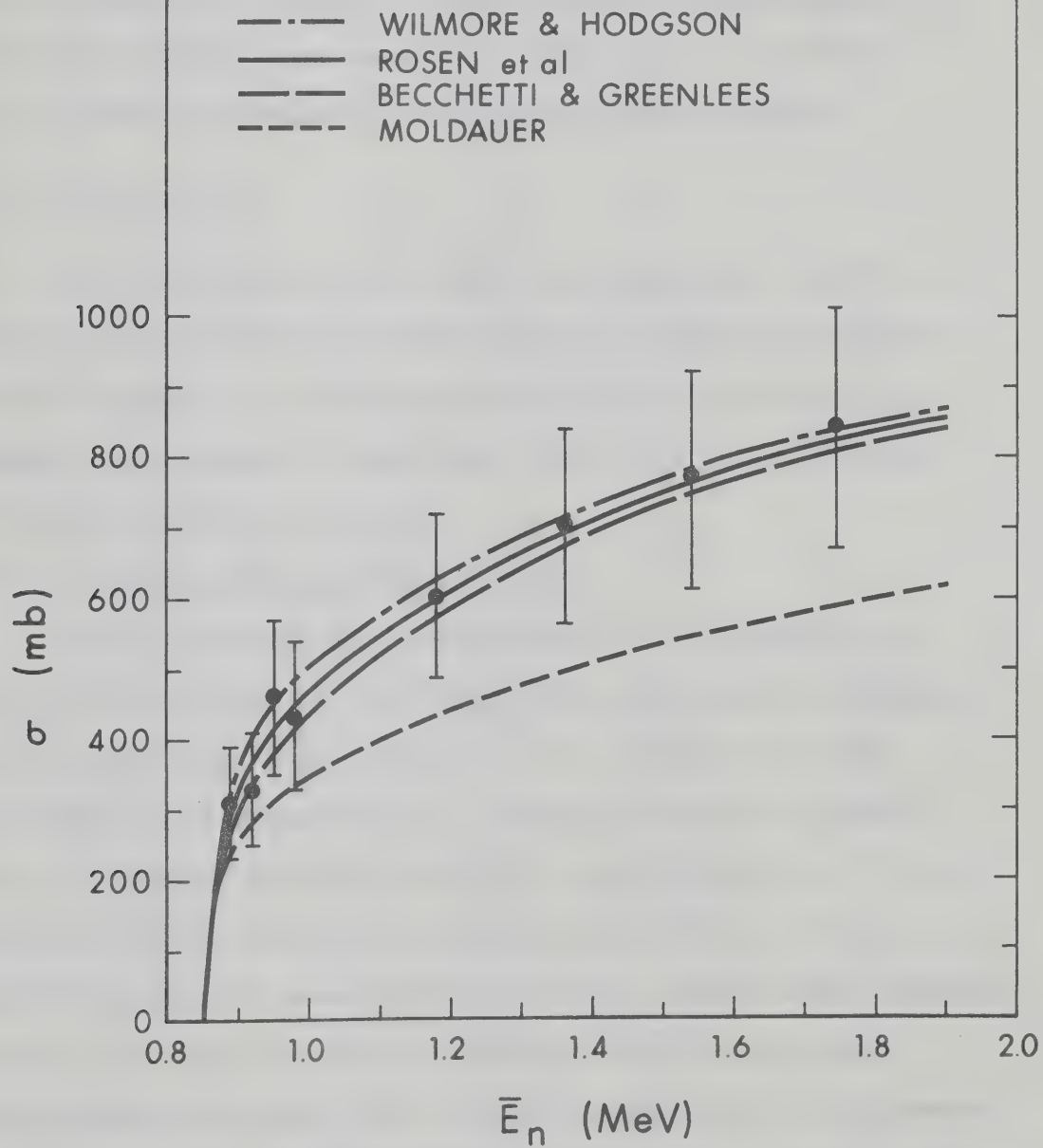
Since the potentials (a,c and d) give similar results, we have arbitrarily chosen the Rosen potential for calculations carried out for Sm and Gd nuclei. Inelastic calculations reported in this





Figure 4.3      Inelastic scattering cross sections of neutrons leading to the 847 keV state in  $^{56}\text{Fe}$ . Theoretical curves were calculated using the potentials of Wilmore and Hodgson (Wi 64), Rosen et al. (Ro 66), Becchetti and Greenlees (Be 69) and Moldauer (Mo 63).

INELASTIC SCATTERING CROSS SECTIONS  
FOR THE 847 keV STATE OF  $^{56}\text{Fe}$





thesis were carried out using Moldauer's code "NEARREX" (Mo 64a). The width fluctuation correction was applied and the  $(n,\gamma)$  exit channel was taken into account. Input parameters required for this channel were obtained from the tables of Goldberg et al. (Go 66) and Gilbert and Cameron (Gi 65a). However, the effect of including the radiative capture channel was negligible.

### 4.3 The Sm Results

Level positions and decay modes are summarized in table 4.2. These were obtained from an error-weighted average of the results at all energies. The values obtained at the different energies showed good agreement in each case. The levels will be discussed in order of increasing energies.

#### 4.3.1 The 921, 1202 and 1286 keV levels

The 921 keV level has been assigned  $J^\pi = 1^-$  by Veje et al. (Ve 68) from a study of  $(d,d')$  excitation cross section systematics. The observed decay modes (table 4.2) are consistent with this assignment. The present  $(n,n'\gamma)$  excitation function is shown in fig. 4.4 together with the excitation cross section for a  $1^-$  level predicted by the statistical compound nuclear theory. It was not possible to fit the observed yield more than 200 keV above threshold. As the two  $\gamma$ -rays assigned to the 921 keV level have the same excitation curve shape, and as the present branching ratio determination is in good agreement with that of D'Auria et al. (Da 71) from  $\beta$ -decay studies, it is most likely that the cross section





TABLE 4.2

Excitation energies and branching ratios  
of levels in  $^{154}\text{Sm}$

Initial state (keV)	Final state (keV)	E $\gamma$ (keV)	Branching ratios	
			Present work	D'Auria <i>et al.</i>
921 $\pm$ 1	g.s.	921	42 $\pm$ 1	40
	82	839	58 $\pm$ 1	60
1012 $\pm$ 1	82	930	62 $\pm$ 1	58
	267	745	38 $\pm$ 1	42
1099 $\pm$ 1	82	1017	100	100
1178 $\pm$ 1	g.s.	1178	26 $\pm$ 2	28
	82	1096	40 $\pm$ 2	40
	267	911	34 $\pm$ 2	32
1182 $\pm$ 2	267	915	100	
1202 $\pm$ 1	82	1120	(50)	
	921	281	(50)	
1286 $\pm$ 1	82	1204	(75)	
	921	365	(25)	
1338 $\pm$ 1	82	1256	46 $\pm$ 3	
	267	1071	54 $\pm$ 3	
1440 $\pm$ 1	g.s.	1440	40 $\pm$ 2	44
	82	1358	52 $\pm$ 2	51
	267	1173	8 $\pm$ 2	5
1475 $\pm$ 1	82	1393		90
	1099	375*		10
1515 $\pm$ 1	82	1433	100	
1539 $\pm$ 1	82	1475	75 $\pm$ 2 <sup>†</sup>	72
	267	1272	25 $\pm$ 2	14
	1012	527		14
1585 $\pm$ 2	82	1503	7 $\pm$ 2	33
	267	1318	64 $\pm$ 2	67
	921	664	29 $\pm$ 2	0
1755 $\pm$ 2	921	834	$\sim$ 75 <sup>†</sup>	37
	1012	743	$\sim$ 25	30
	1585	170*		33

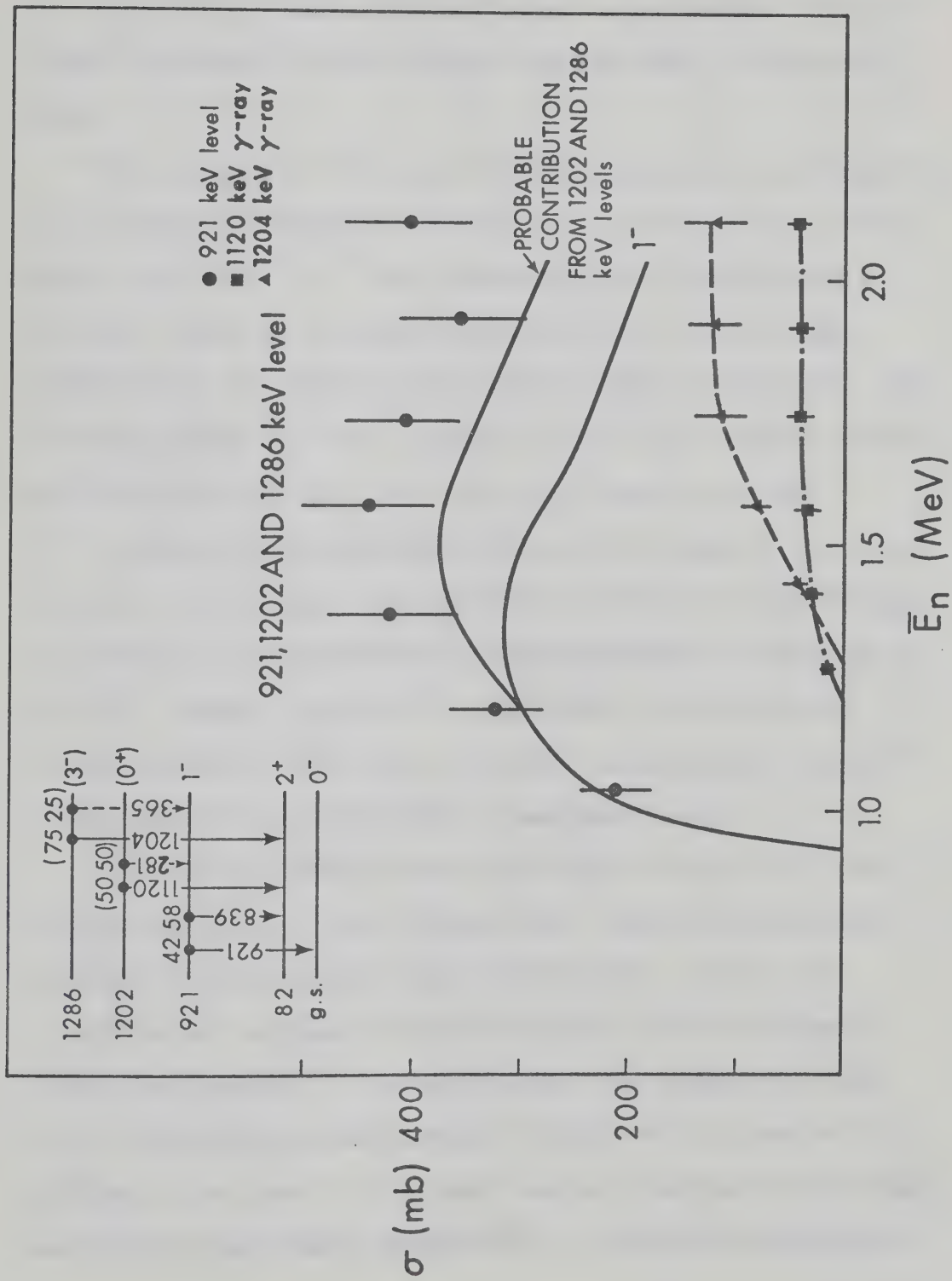
<sup>†</sup> Intensity ratio (see text).

\* These  $\gamma$ -rays could not be observed in the present experiment (see text).





Figure 4.4      Excitation curves for the 921 keV level and the 1120 and 1204 keV  $\gamma$ -rays which depopulate the 1202 and 1286 keV levels, respectively. The probable contribution from the latter two levels to the 921 keV level, as discussed in §4.3.1, is also indicated. The experimental points for the 921 keV level above a neutron energy of 1.5 MeV contain a  $\sim 15\%$  correction due to feeding from the 1585 and 1755 keV levels.





discrepancy is due to unaccounted-for cascade feeding from a level or levels between 200 and 500 keV higher in excitation. The most likely candidates are the 1202 and 1286 keV levels, as discussed below.

The presence of a level at 1202 keV excitation is indicated by the excitation function of the 1120 keV  $\gamma$ -ray (fig. 4.4). This is most likely the  $J^\pi = 0^+$  level observed in the (t,p) reaction at 1218 keV. Also the excitation function of the 1204 keV  $\gamma$ -ray shown in fig. 4.4 indicates an origin at 1286 keV excitation. This is most probably the level observed via the (p,p') reaction (Ke 64) at 1295 keV and at 1299 keV via the (t,p) reaction (Bj 66).

It should be mentioned that at the early stages of the present analysis it was thought that the 1120 and 1204 keV  $\gamma$ -rays belonged to a level at 1204 keV which is quoted in the paper of D'Auria et al. (Da 71). However, as the two  $\gamma$ -rays appear to have different threshold energies (fig. 4.4) it has been concluded that the two  $\gamma$ -rays belong to separate levels as mentioned above.

The 1202 and 1286 keV levels can decay to the 921 keV level via 281 and 365 keV  $\gamma$ -rays, respectively. Both  $\gamma$ -rays have been observed in the previous  $\gamma$ -decay work (Da 71). The 281 keV transition was assigned to two other levels, but the assigned transition strengths in the decay scheme only account for some 75% of the total observed strength; the 365 keV  $\gamma$ -ray was not assigned to any level. A 365 keV  $\gamma$ -ray was observed in the present work with an approximate threshold of 1.3 MeV but no quantitative





yield measurements could be obtained (§ 4.1).

The 1120 keV  $\gamma$ -ray excitation curve is in agreement with the predicted shape for a  $0^+$  level, but is only approximately half the expected strength. The 1204 keV  $\gamma$ -ray yield can be fitted by either a  $J=3$  curve scaled by a factor of 0.75, or  $J=4$  scaled by 1.5. The observed branch to the 921 keV  $1^-$  level and the excitation of the level via the (t,p) reaction then strongly suggest an assignment of  $J^\pi = 3^-$  for the 1286 keV level. The expected contribution to the 921 keV level from these two states then brings the experimental yield curve into fair agreement with the expected excitation function.

#### 4.3.2 The 1012 and 1099 keV levels

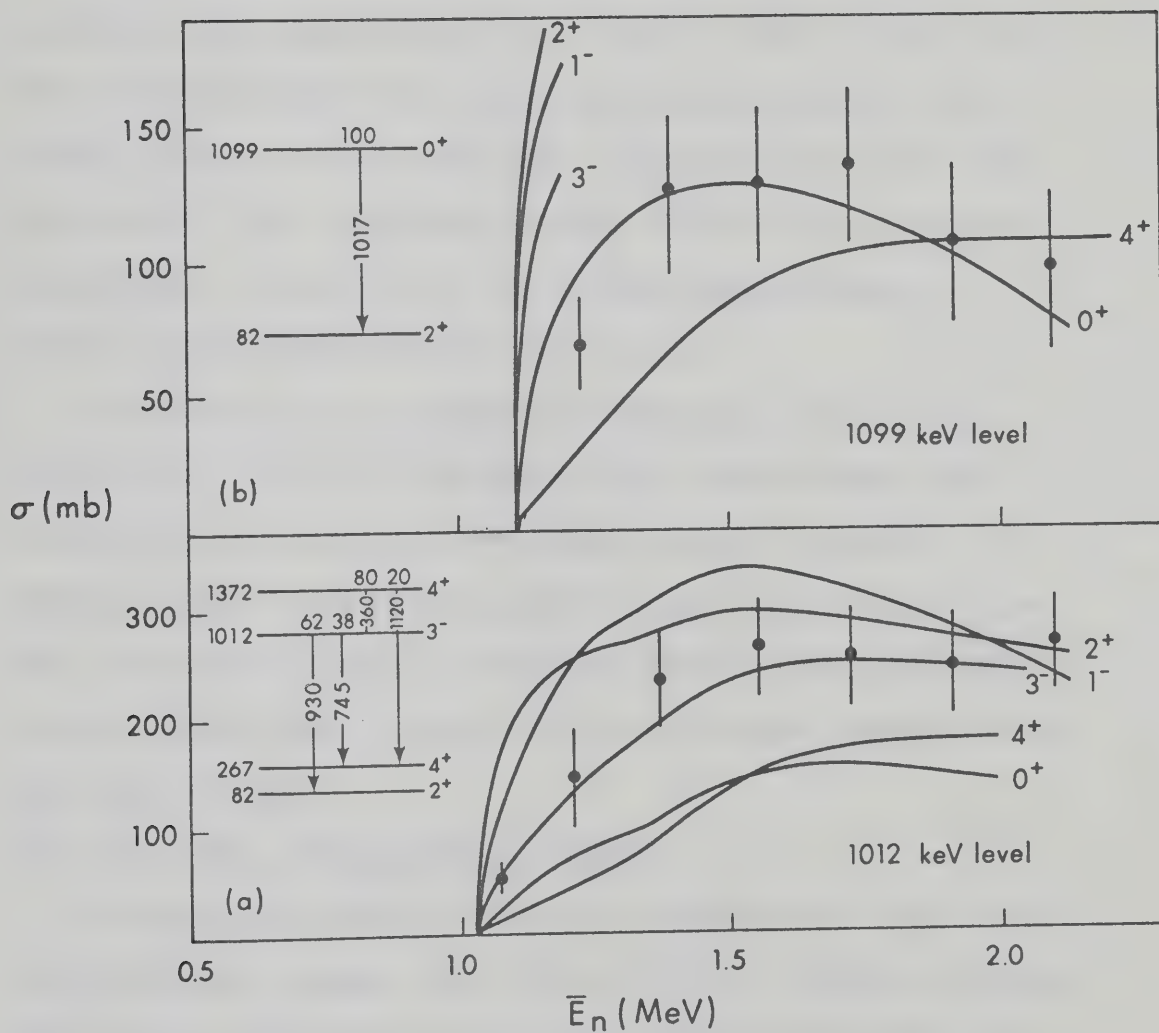
The 1012 keV level has been observed in several reactions (Ke 64, Bj 66, Se 66, Ve 68, Da 71), and has been assigned  $J^\pi = 3^-$  (Ha 63, Ve 68). The present experimental yield curve for this level is shown in fig. 4.5a. Also shown are various yield curves which also include the expected contribution from the 1372 keV  $4^+$  level and the known (Da 71) decay scheme for the 1372 keV level. The experimental points indicate a preferred assignment of  $J^\pi = 3^-$ , in good agreement with the previous results.

The 1099 keV level decays entirely to the 82 keV ( $2^+$ ) level and has been assigned  $J^\pi = 0^+$  (Bj 66, Ve 68). The experimental yield curve of the 1099 keV level has been corrected for cascade feeding from the 1475 keV level using the measured  $1475 \rightarrow 82$  keV transition yield and the known (Da 71) decay scheme for the 1475 keV





Figure 4.5      Excitation curves for the 1012 (a) and 1099 (b) keV levels. The calculated curves for the 1012 keV level also contain the expected contribution from the 1372 keV  $4^+$  level, and the experimental points above 1.7 MeV have been corrected for feeding from the 1707 and 1755 keV levels.





level. The resulting yield curve (fig. 4.5b) indicates a preferred assignment of  $J^\pi = 0^+$ , in agreement with the previous results.

#### 4.3.3 The 1178 and 1182 keV levels

A close doublet has been observed at approximately 1.18 MeV excitation with suggested spins of  $2^+$  and  $5^-$  (Yo 65, Se 66, Ve 68). The present experiment has clearly resolved the members of this doublet to be at 1187 and 1182 keV. The yield curves (fig. 4.6) indicate a  $2^+$  and  $5^-$  assignment for the 1178 and 1182 keV levels, respectively. D'Auria et al. (Da 71) have also been able to measure the decay modes of these two levels.

The 636 keV  $\gamma$ -ray, assigned by Seaman et al. (Se 66) and D'Auria et al. (Da 71) to the decay of the 1182 keV level, was not observed in the present work below a neutron bombarding energy of about 1.8 MeV and so cannot belong to the 1182 keV level. This  $\gamma$ -ray could be due to a transition from a level at 1818 keV to the 1182 keV level; a level at 1811 keV has been reported in the (d,d') work (Ve 68).

#### 4.3.4 The 1338, 1440 and 1707 keV levels

The excitation function of the 1071 and 1256 keV  $\gamma$ -rays (fig. 4.7a) indicates a common origin from a level at 1338 keV excitation. This probably corresponds to the level observed by Kennefick and Sheline at  $1344 \pm 10$  keV. The observed decay scheme and excitation curve indicate an assignment of  $4^+$  for the 1338 keV level.

The 1440 keV  $2^+$  level decays via 1440, 1358 and 1173 keV  $\gamma$ -rays







Figure 4.6      Excitation curves for the 1178 and 1182 keV levels.

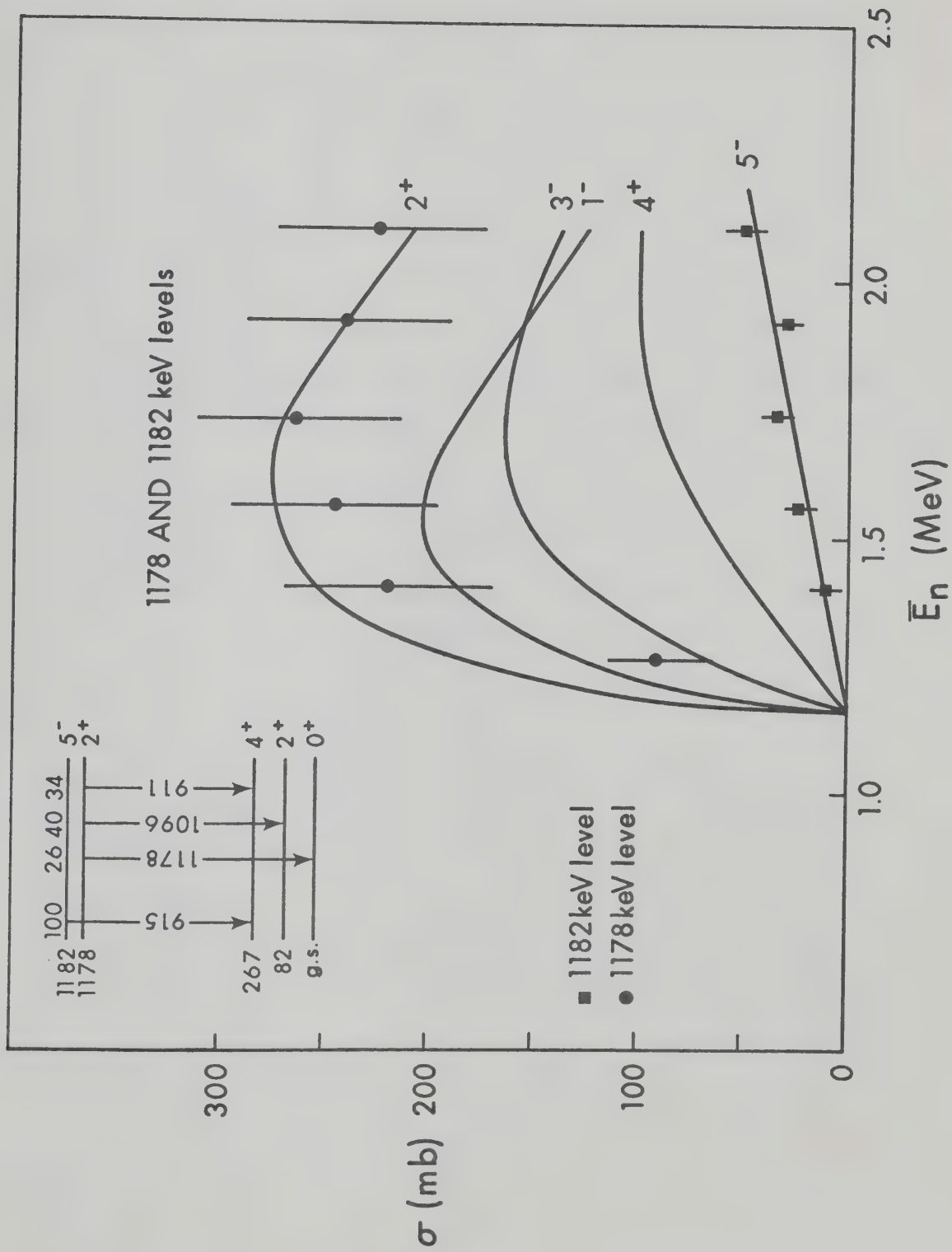
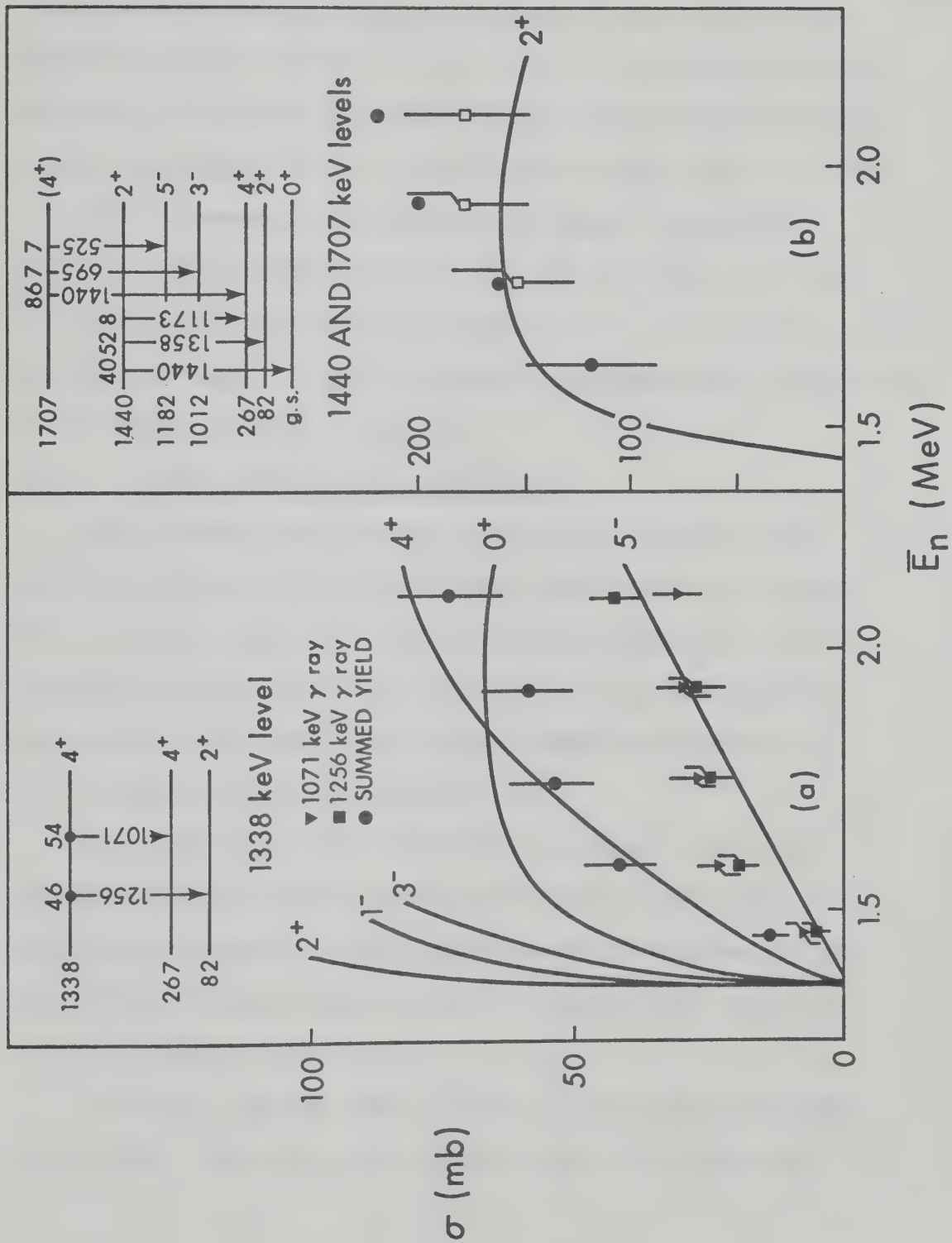






Figure 4.7      Excitation curves for the 1338 (a), 1440 and 1707 (b) keV levels. The square points in the excitation curve of the 1440 keV level have been corrected for the contribution from the 1707 keV level using the previously measured (Da 71) branching ratio and the expected  $4^+$  excitation cross section.







to the ground, 82 keV and 267 keV levels, respectively. The 1440 keV  $\gamma$ -ray has also been assigned to the decay of the 1707 keV level which has a spin of either  $3^-$  or  $4^+$  (Da 71). The contribution to the yield curve due to the 1707 keV level was estimated using its known decay scheme (Da 71) and the expected cross section for both  $3^-$  and  $4^+$ . However, it was possible to obtain a consistent branching ratio determination for the 1440 keV level only if the spin of the 1707 keV level was assumed to be  $4^+$ . The yield curve for the 1440 keV level is then in reasonable agreement with the predicted  $2^+$  excitation function (fig. 4.7b).

#### 4.3.5 The 1475, 1662 and 1515 keV levels

The 1393 keV  $\gamma$ -ray belongs to the decay of both the 1475 and 1662 keV levels (Da 71) which have been tentatively assigned  $J^\pi = 1^-$  (Ve 68) and  $J^\pi = 4^+$  (Ve 68, Yo 65) respectively. The assumption of two origins for the 1393 keV  $\gamma$ -ray is supported by an observed 2 keV energy shift between bombarding energies of  $E_n = 1.6$  and 2.1 MeV in the present work.

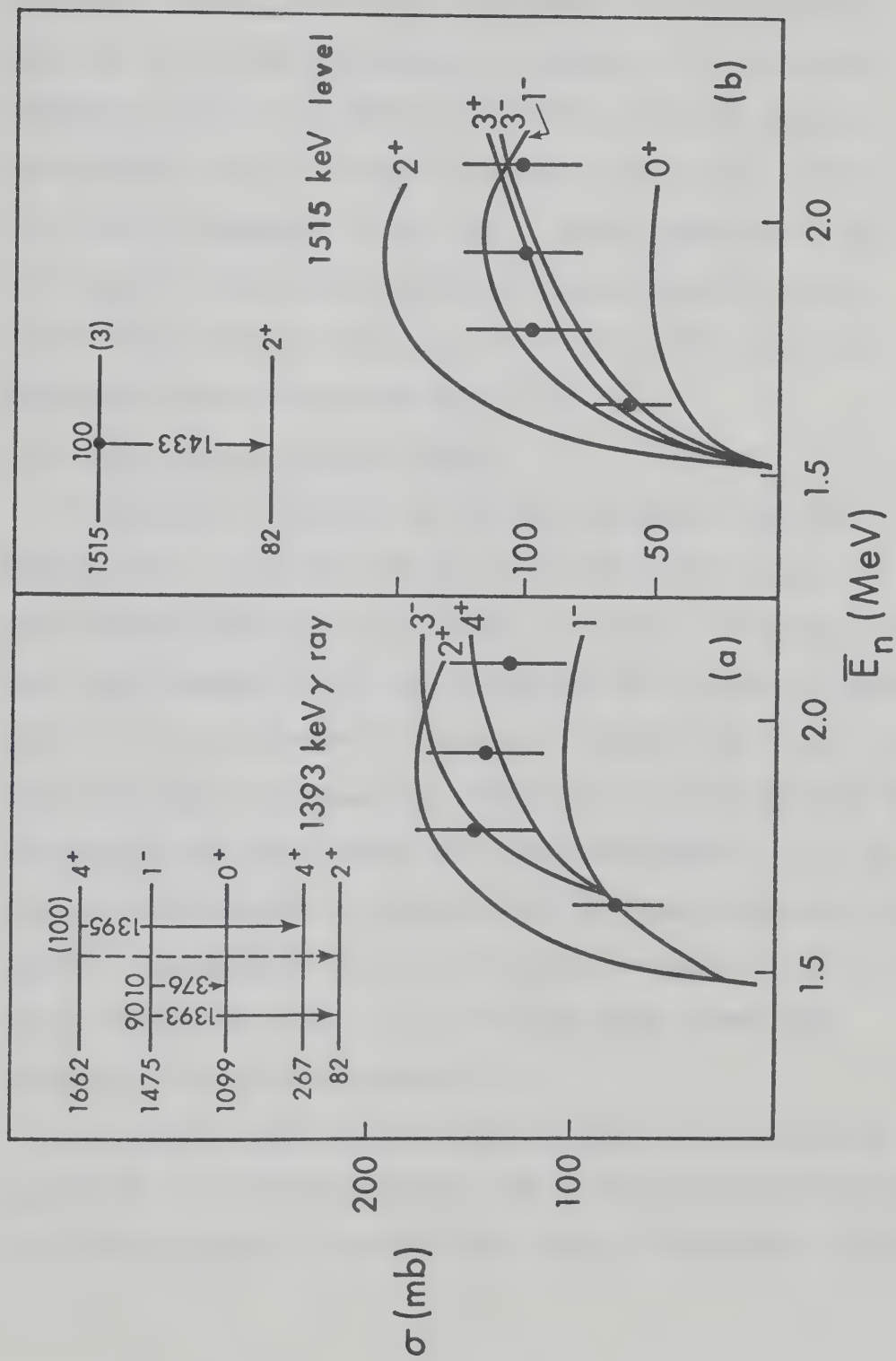
The yield curve of the 1393 keV  $\gamma$ -ray shown in fig. 4.8a is compared with the expected contribution from the two levels using the above assignments. Reasonable agreement is obtained for both the 1475 and 1662 keV levels using the expected yield curves for  $1^-$  and  $4^+$  levels, respectively.

At neutron energies above 1.6 MeV, a 1433  $\gamma$ -ray was observed (fig. 4.8b). The yield curve indicates that this  $\gamma$ -ray could





- Figure 4.8 (a) Excitation curve of the 1393 keV  $\gamma$ -ray depopulating the 1475 and 1662 keV levels. The predicted curves for the 1475 keV levels have been adjusted to account for the (unmeasured) 10% decay to the 1099 keV level. The  $\gamma$ -ray from the 1662 keV level to the 82 keV level was weakly observed in the work of D'Auria et al. (Da 71).
- (b) Excitation curve of the 1515 keV level.





belong to a level at either 1433 or 1515 keV excitation. No previously reported level would correspond to an excitation of 1433 keV, but a level, tentatively assigned  $J = 3^+$ , has been observed at 1522 keV by Kenefick and Sheline (Ke 64), and so the 1433 keV  $\gamma$ -ray is assumed to belong to that level. No other  $\gamma$ -ray could be assigned to the level. From a comparison of the observed yield with that expected for various possible spins, the 1515 keV level can have a spin of  $1^-$  or 3. Of these, the decay mode is more consistent with  $J = 3$ .

#### 4.3.6 The 1539 and 1585 keV levels

Transitions to the 82, 267 and 1012 keV levels have been observed from a level at 1539 keV. Although D'Auria et al. (Da 71) have proposed this level as a new one, it is more likely to be the same level reported in the (p,p') work (Ke 64) at 1547 keV (note also the 7 keV difference in the case of the 1515 keV level). In the present work the transition strength to the 1012 keV level was not measured and consequently the yield curve shown in fig 4.9a has been corrected for this decay using the known branching ratio (Da 71). The measured excitation function for the 1539 keV level can be fitted with either  $J = 1$  or 3; the decay scheme then indicates a preferred assignment of 3.

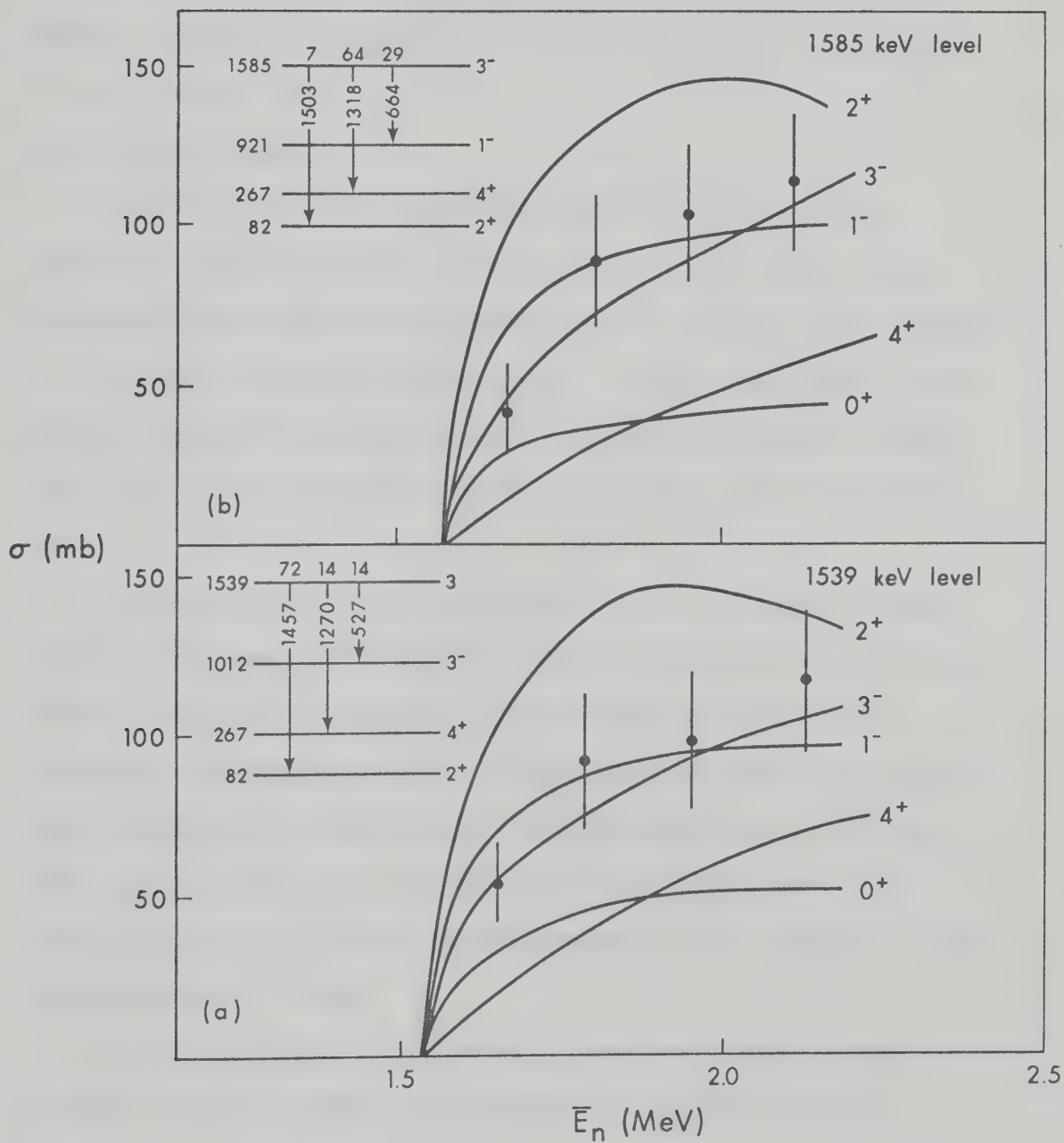
The level at 1585 keV has been assigned  $J^\pi = 3^-$  by Veje et al. (Ve 68). The present results (fig. 4.9b) are in good agreement with that assignment. The 664.6 keV  $\gamma$ -ray was assigned by D'Auria







Figure 4.9      Excitation curve of (a) the 1539 and (b) the 1585 keV levels. Branching ratios of  $\gamma$ -rays from the 1539 keV level are those of D'Auria et al. (Da 71).





et al. to the decay of  $^{155}\text{Sm}$ , produced by neutron capture. However in the present work the excitation function of the 664  $\gamma$ -ray was entirely consistent with the decay of a level in  $^{154}\text{Sm}$  at approximately 1.58 MeV. Consequently it has been assigned to the decay of the 1585 keV level.

#### 4.3.7 Other levels

The 743 and 834 keV  $\gamma$ -rays from the 1755 keV level were observed at neutron energies greater than 1.8 MeV. There was no evidence at any energy for the existence of a 170 keV  $\gamma$ -ray assigned to the 1755 keV level by D'Auria et al. In the latter work,  $\gamma$ -rays within 1 keV of this energy were also assigned to decays in  $^{151}\text{Nd}$  and  $^{155}\text{Sm}$ , which may account for the discrepancy with the present work.

The close proximity of the 743 keV  $\gamma$ -ray to the much stronger 745 keV line made it difficult to obtain reliable estimates of the 743 keV  $\gamma$ -ray yield. However, the determined branching ratio obtained in the present work is in fair agreement with the intensity ratios obtained by D'Auria et al. The measured total yield curve (fig. 4.10a) suggests an assignment of  $2^+$  for the 1755 keV level. This is consistent with the observed decays to the 1012 keV  $3^-$  level and the 921 keV  $1^-$  level.

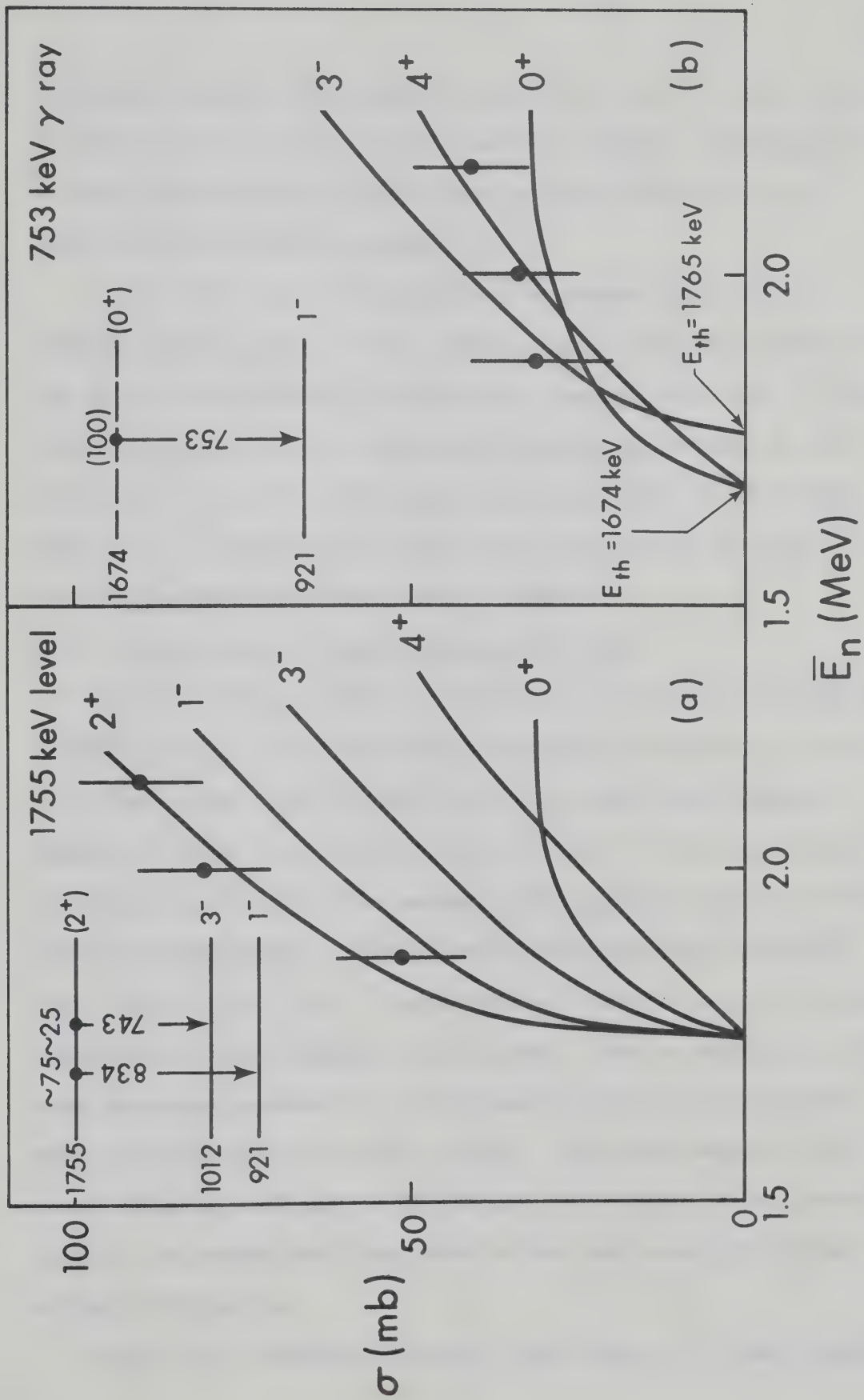
The 753 keV  $\gamma$ -ray was observed for neutron energies above 1.8 MeV. This  $\gamma$ -ray does not correspond to a decay from any previously observed level, and most likely indicates the existence of a new level at an excitation of either 1674 or 1765 keV. The







Figure 4.10      Excitation curve of (a) the 1755 keV level and  
                         (b) the 753 keV  $\gamma$ -ray. The calculated yield  
                         curve for the 753 keV level indicates the two  
                         possible level origins.





excitation function then suggests a spin of  $4^+$  or  $0^+$  if the level is at 1674 keV or  $3^-$  if it is at 1765 keV. (fig. 4.10b). The decay mode is most consistent with an assignment of the 753 keV  $\gamma$ -ray to a level at 1674 keV with a probable  $J^\pi = 0^+$ .

A 1550 keV  $\gamma$ -ray was observed in the present work only at neutron energies greater than 1.8 MeV. Most likely this transition and the 636 keV (see §4.3.3) belong to a level at 1817 keV. If this level corresponds to that observed by Veje et al. (Ve 68) at 1811 keV with  $J^\pi = 3^+$  or  $4^+$ , then the present decay mode is consistent with  $J = 4^+$ . D'Auria et al. (Da 71) has assigned the 1549 keV  $\gamma$ -ray to the decay of a new level at 1549 keV.

#### 4.3.8 Level scheme and band structure of $^{154}\text{Sm}$

The level decay scheme of  $^{154}\text{Sm}$  up to an excitation of 1755 keV is shown in fig. 4.11. Rotational bands built on octupole,  $\beta$ - and  $\gamma$ -vibrational modes were proposed in  $^{154}\text{Sm}$  by many investigators. Members of these bands are also shown in fig. 4.11. We have been able to clearly resolve the third member of the octupole band at 1182 keV from the second member of the  $\beta$ -band at 1178 keV and to determine their spins to be  $5^-$  and  $2^+$  respectively. The level at 1539 keV was identified as the  $3^+$  member of the  $\gamma$ -band. This is consistent with both the energy systematics of this band (Ku 67) and the observed decay mode and inelastic cross sections. The third member of the  $\beta$ -band shown at 1372 keV excitation was not included in the present study as the predominant decay mode is too low in energy to obtain reliable information.

Most of the unclassified levels shown in fig. 4.11 were reported





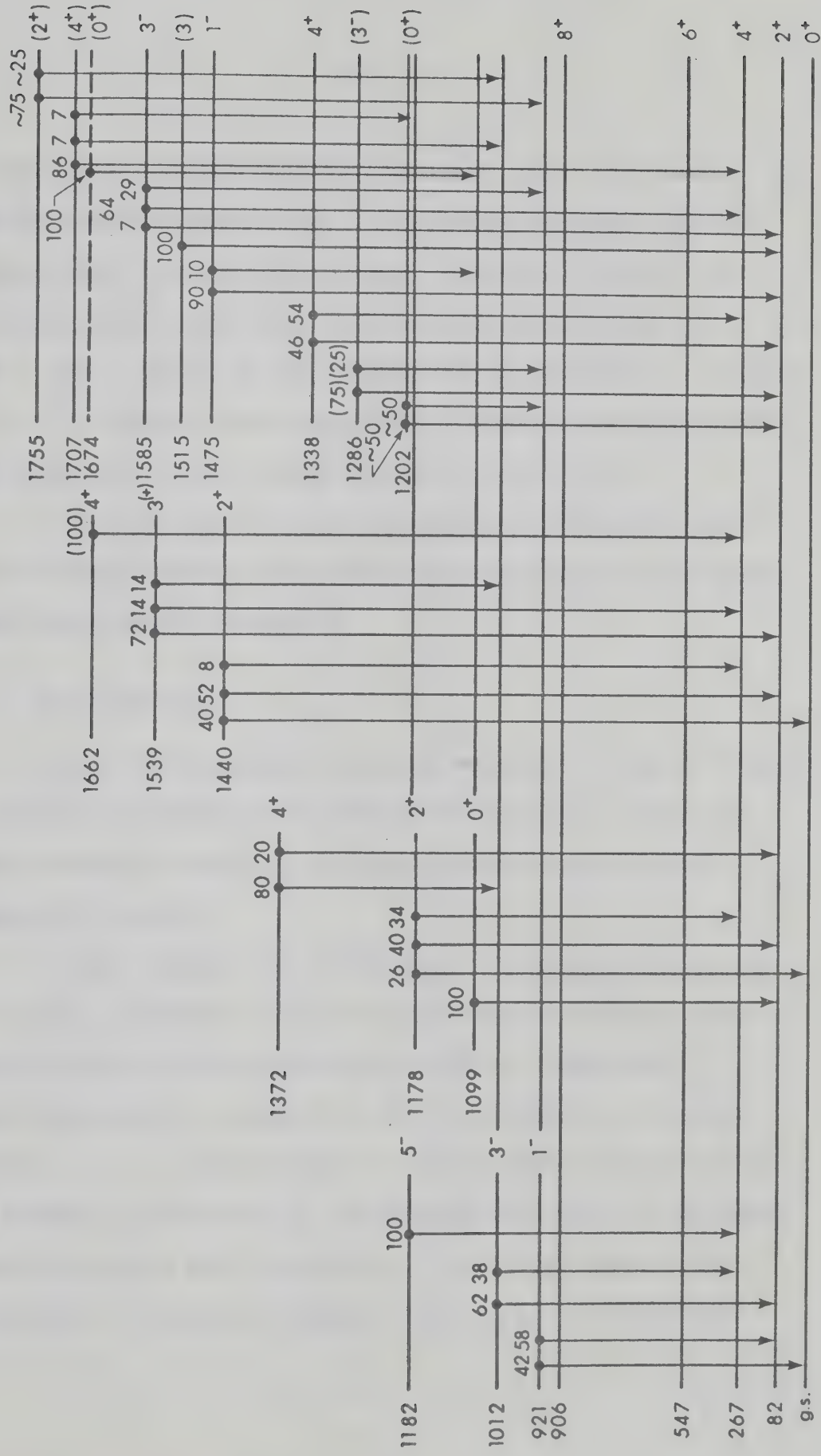
Figure 4.11 Level scheme of  $^{154}\text{Sm}$  excited states up to 1755 keV; known members of various bands are also indicated. The excitation energy of the  $8^+$  level shown at 906 keV is based on the energy of the  $8^+ \rightarrow 6^+$  transition measured by Diamond et al. (Di 72) and the position of the  $6^+$  level reported by D'Auria et al. (Da 71). The decay mode of the 1372, 1475, 1539 and 1707 keV levels are from D'Auria et al. (Da 71).

# OCTUPOLE BAND

## $\beta$ BAND

## $\gamma$ BAND

## UNASSIGNED LEVELS







in the (p,p') work but were not observed in other experiments. It was possible to populate them in the present reaction study and observe their de-excitation  $\gamma$ -rays. In addition, possible spin assignments for these levels were made and indicated in fig. 4.11. The  $1^-$  and  $3^-$  levels at 1475 and 1585 keV could possibly be members of a  $K = 1$  octupole vibrational band. It must be anticipated that any additional classification will be very difficult.

In general, the level spin assignments and branching ratio determinations obtained from the present study are in good agreement with previous information.

#### 4.4 The Gd Results

The excitation energies and decay modes for levels of  $^{160}\text{Gd}$  up to 1600 keV excitation are summarized in table 4.3. These are error-weighted averages of the results obtained at different bombarding energies.

It seems appropriate, before going into detailed discussion of results, to mention that the calculations of inelastic cross sections were carried out using four sets of transmission coefficients which correspond to the four potential parameters listed in §4.2. This was done in order to check the sensitivity of inelastic calculations in the deformed mass region to different spherical optical model potentials. Predictions based on the potentials of Wilmore and Hodgson, Rosen et al., and Becchetti



Excitation energies and branching ratios  
of levels in  $^{160}\text{Gd}$

Initial state (keV)	Final state (keV)	$E_\gamma$ (keV)	Branching ratios
$989 \pm 1$	g.s.	989	$46 \pm 1$
	75	914	$54 \pm 1$
$1058 \pm 1$	75	983	$83 \pm 1$
	249	809	$17 \pm 1$
$1071 \pm 1$	75	996	$36 \pm 1$
	249	822	$64 \pm 1$
$1149 \pm 1$	75	1074	$34 \pm 1$
	249	900	$66 \pm 1$
$1225 \pm 1$	g.s.	1225	$39 \pm 1$
	75	1150	$61 \pm 1$
$1262 \pm 1$	75	1187	$66 \pm 1$
	249	1013	$34 \pm 1$
$1290 \pm 1$	75	1215	$54 \pm 2^\dagger$
	249	1041	$46 \pm 2$
$1351 \pm 1$	g.s.	1351	$22 \pm 3$
	75	1276	$78 \pm 3$
$1378 \pm 1$	g.s.	1378	100
$1381 \pm 2$	g.s.	1381	100
$1464 \pm 1$	75	1389	
	249	1215	
$1569 \pm 2$	g.s.	1569	
	75	1494	
	989	580	
$1587 \pm 2$	g.s.	1587	
	75	1512	
$1599 \pm 2$	g.s.	1599	
	75	1524	

$^\dagger$  These are the values determined at  $E_n < 1.4$  MeV (see text).



and Greenlees (§ 4.2) were similar to within 10%. The "reasonable" agreement obtained between measured and calculated cross sections for the Sm (§ 4.4) and Gd (shown below) nuclei indicates that any one of these three potentials is good enough for inelastic calculations, even in the case of highly deformed nuclei. The Moldauer potential has yielded good fits to excitation functions of positive-parity states but underestimates, by a factor of  $\sim 2$ , the cross sections for levels of negative parity. In fact, the use of Moldauer transmission coefficients has improved the fits, especially just above threshold (in the case of positive parity states). Moldauer potential was designed to fit the s-wave neutron strength function and elastic scattering data for energies below 1 MeV. This probably explains why it yielded better fits at low energies for positive parity states. Fig. 4.12 displays the transmission functions calculated using both Rosen and Moldauer potentials. The difference between the values of  $T_\ell$ , especially for odd partial waves, is quite obvious.

In the following we will discuss the levels of  $^{160}\text{Gd}$  in order of increasing energy.

#### 4.4.1 The 989 keV level

This level has been observed in both (p,p') and (d,d') studies (Sh 66, Bl 67), and has been assigned  $J^\pi = 2^+$  from cross section systematics of the (d,d') reaction (Bl 67). The observed decay mode (fig. 4.13) is consistent with either  $J^\pi = 1^-$  or  $2^+$ . No







Figure 4.12      The neutron transmission functions of  $^{160}\text{Gd}$   
for various partial waves using Rosen and  
Moldauer potentials.

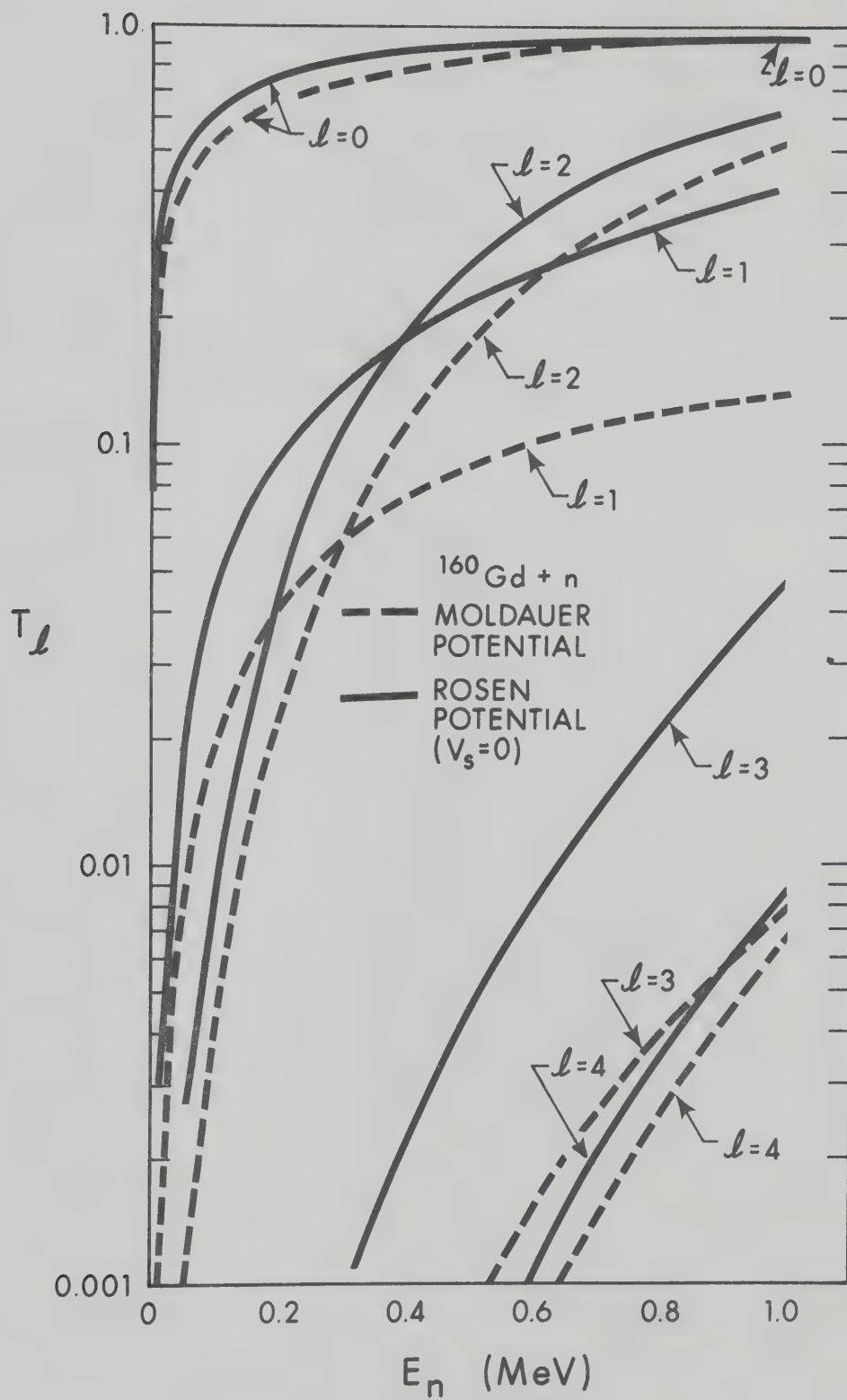
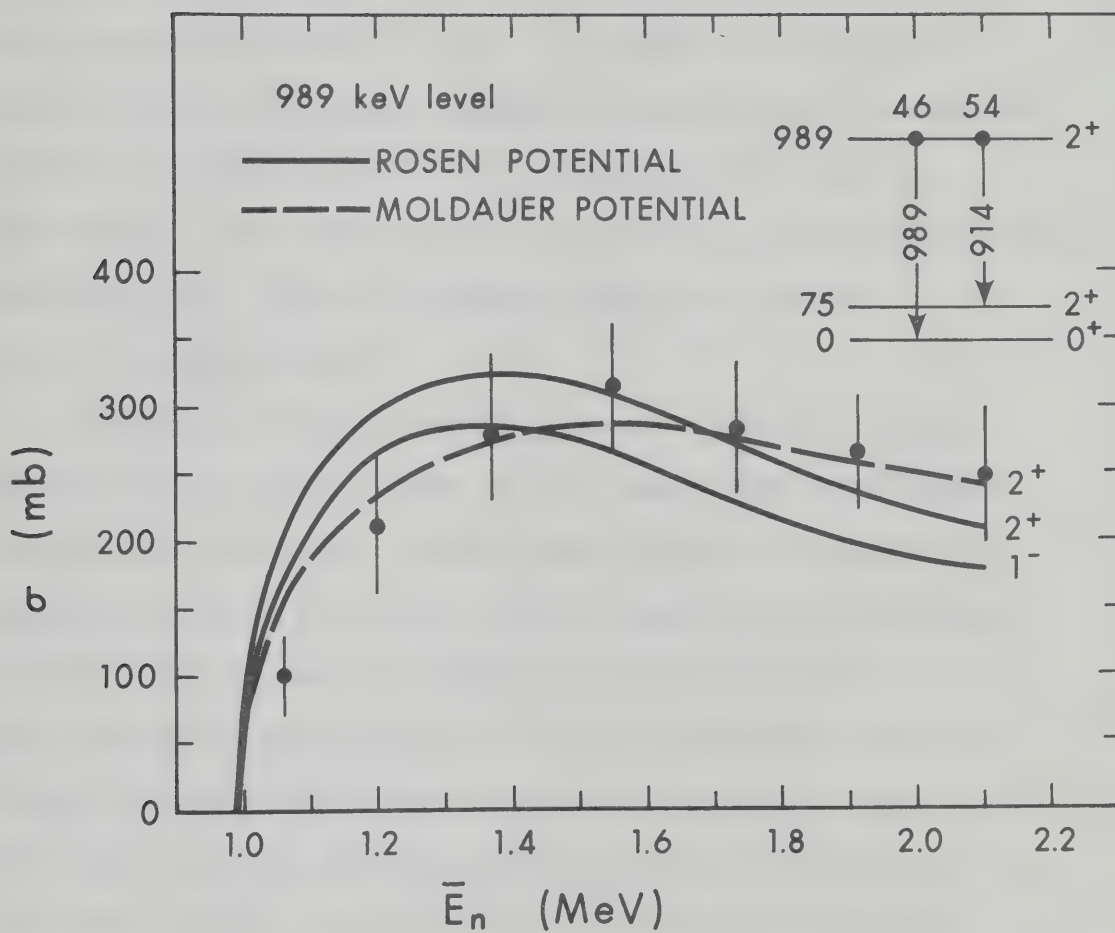






Figure 4.13      Excitation curve of the 989 keV level.





branch to the  $4^+$  level of the ground state band could be identified in the present results. The strength of such a transition is expected to be very small (3%). The measured neutron inelastic cross sections are shown in fig. 4.13 together with theoretical predictions using Rosen and Moldauer transmission coefficients. A good fit is obtained for  $J^\pi = 2^+$ , in agreement with previous assignments. This level has been identified by both Sheldon (Sh 66) and Bloch et al. (Bl 67) as the band head of the  $\gamma$ -band.

#### 4.4.2 The 1058 keV level

Sheldon (Sh 66) has reported a level at 1060 keV. If the 989 keV level is the  $2^+$  member of the  $\gamma$ -band, then the  $3^+$  member should lie at  $\sim 1057$  keV. On this basis, Sheldon has tentatively proposed a spin of  $3^+$  for this level. Since the (d,d') reaction preferentially excites  $3^-$  states (and not  $3^+$ ), this level has not been observed by Bloch et al. (Bl 67). In the present work the  $\gamma$ -rays of 983 and 809 keV have been associated with a level at 1058 keV. Its decay mode and excitation curve (fig. 4.14) are consistent with an assignment of  $J = 3$ . From potential energy systematics, this level has been identified as the  $3^+$  member of the  $\gamma$ -band.

#### 4.4.3 The 1071 and 1149 keV levels

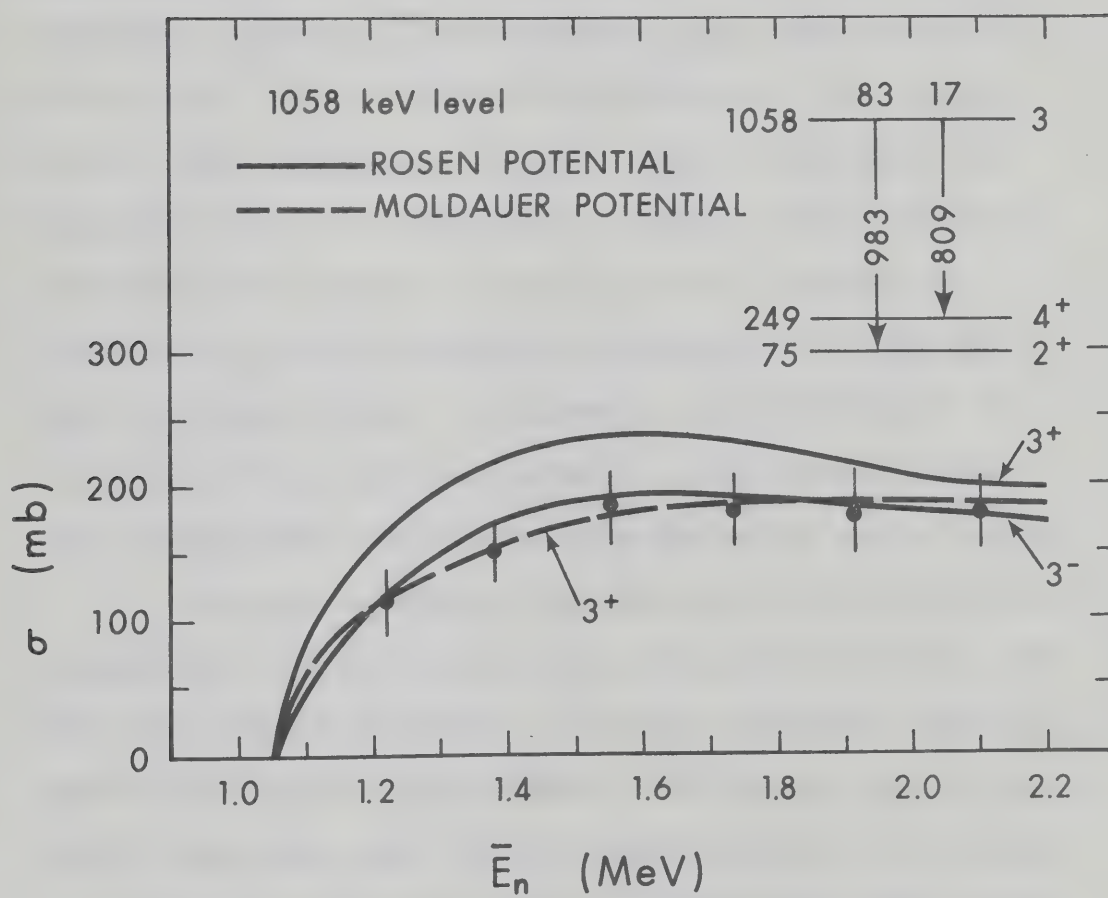
The level at 1071 was weakly excited by the (d,d') reaction (Bl 67) and tentatively assigned  $J^\pi = 2^+$ . It has not been reported in the (p,p') work (Sh 66). Two transitions (996 and







Figure 4.14      Excitation curve of the 1058 keV level.





822 keV) from this level to  $2^+$  and  $4^+$  levels of the ground state band have been observed in the present study (fig. 4.15). If this level has a spin of  $2^+$ , as suggested by Bloch et al. (Bl 67), it should decay by a relatively strong branch to the ground state. Assuming that the 1074 keV  $\gamma$ -ray observed in the present spectra corresponds to such a  $2^+ \rightarrow 0^+$  transition (note that its energy is off by 3 keV), it was found that the magnitude of cross section for this level (combining the three  $\gamma$ -rays) is only 40% of the theoretical values for a spin of  $2^+$ . Moreover, the shape of the excitation curve indicates a high spin state. Therefore the 1074 keV  $\gamma$ -ray has been assigned to the decay of the 1149 keV level as discussed below. Consequently, the possibility of  $J^\pi = 2^+$  for the 1071 keV level was ruled out. The measured inelastic cross sections were then compared with theoretical predictions for  $J^\pi = 4^+$ . Although the shape of the experimental excitation function is consistent with the one calculated using Rosen potential, only 60% of the strength is observed. The use of Moldauer transmission coefficients yielded a good agreement with measured cross sections only for the region about 400 keV above threshold. If this level is a  $4^+$  then the transition to the  $6^+$  member of the ground state band is expected to be very weak and was not observed.

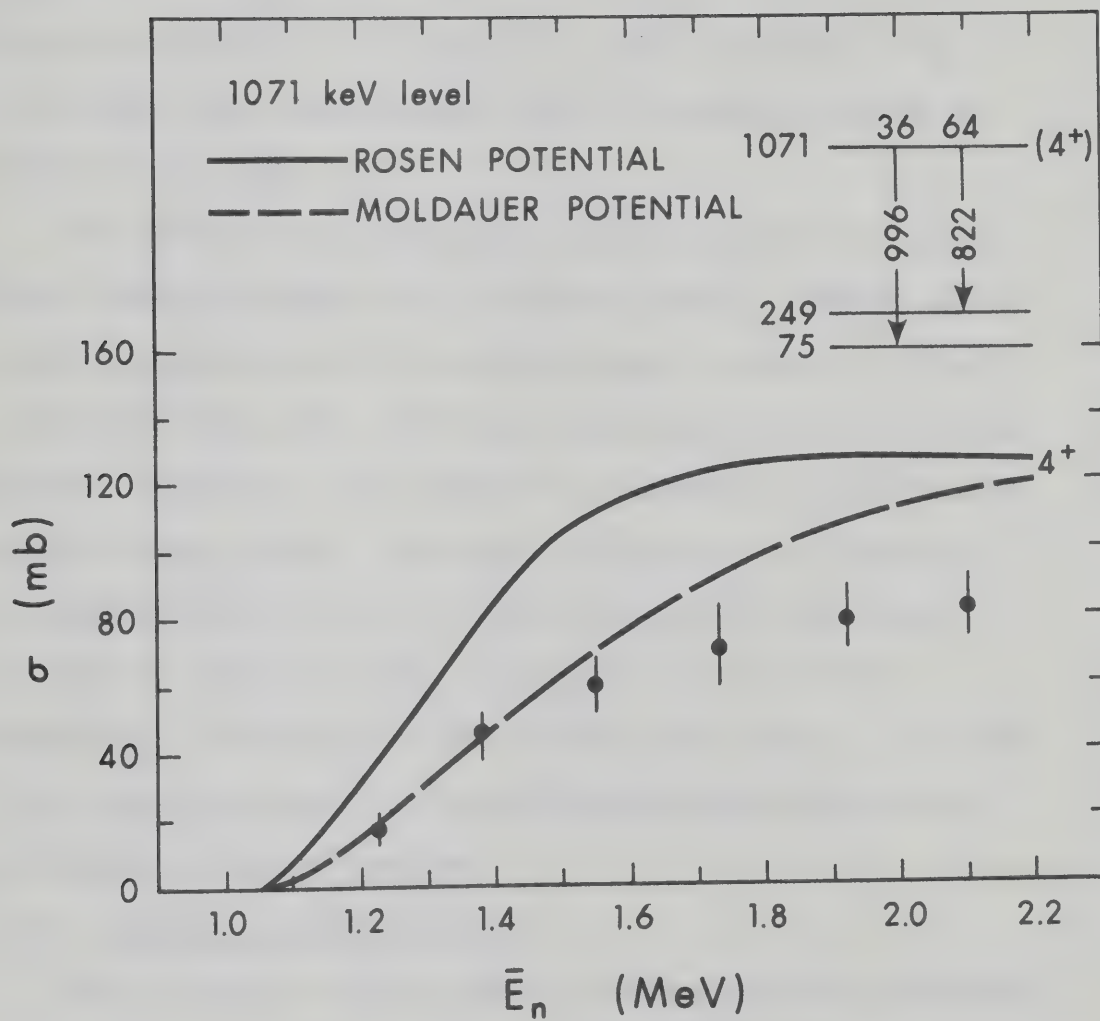
The level at 1149 keV has previously been identified as the  $4^+$  member of the  $\gamma$ -band (Sh 66, Bl 67). The 1074 and 900 keV  $\gamma$ -rays observed in the present experiment have been assigned to the decay of this level to  $2^+$  and  $4^+$  members of the ground state







Figure 4.15      Excitation curve of the 1071 keV level. Theoretical predictions are for  $J^\pi = 4^+$  using Rosen and Moldauer transmission coefficients.





band, respectively. Fig. 4.16 shows the decay mode and inelastic cross sections for this level. It is clear that the measured and calculated cross sections (for  $J^\pi = 4^+$ ) show a situation similar to that encountered in the case of the 1071 keV level. It is also noticed that the branching ratios of  $\gamma$ -rays from these two levels are the same.

The 1149 keV level can decay to the  $6^+$  member of the ground state band by a very weak  $\gamma$ -ray of 633 keV energy. Although such a  $\gamma$ -ray was observed, we feel uncertain about assigning it to such a transition due to the relatively high background in this energy region. In addition, its excitation curve shows a sudden rise at neutron energy around 1.7 MeV which indicates that it might be a transition from a level at 1691 keV to the 1058 keV state; a  $3^-$  level at 1688 keV has been observed in the (d,d') work. Regardless, the strength of this 633 keV  $\gamma$ -ray below  $E_n = 1.7$  MeV is too small to account for the difference between measured and calculated excitation functions.

#### 4.4.4 The 1225 and 1290 keV levels

The existence of these states is well established by previous studies. (Sh 66, Bl 67). A tentative assignment of  $1^-$  has been made by Bloch et al. (Bl 67) for the 1225 keV level. The present results (fig. 4.17) confirm this assignment.

The 1290 keV state has been observed to decay to the  $2^+$  and  $4^+$  states of the ground state band via 1215 and 1041 keV  $\gamma$ -rays.





Figure 4.16      Excitation curve of the 1149 keV level.  
Theoretical predictions are for  $J^\pi = 4^+$   
using Rosen and Moldauer transmission  
coefficients.

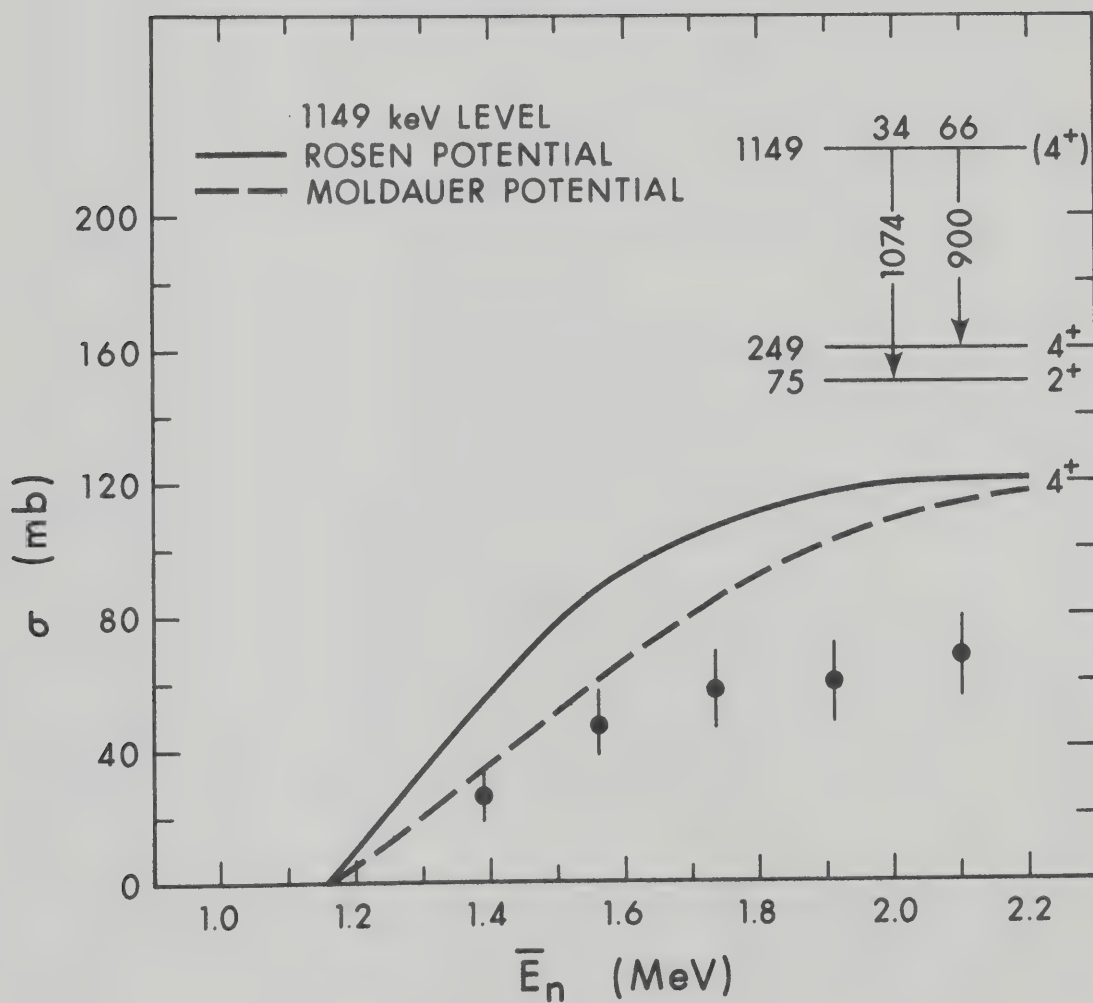
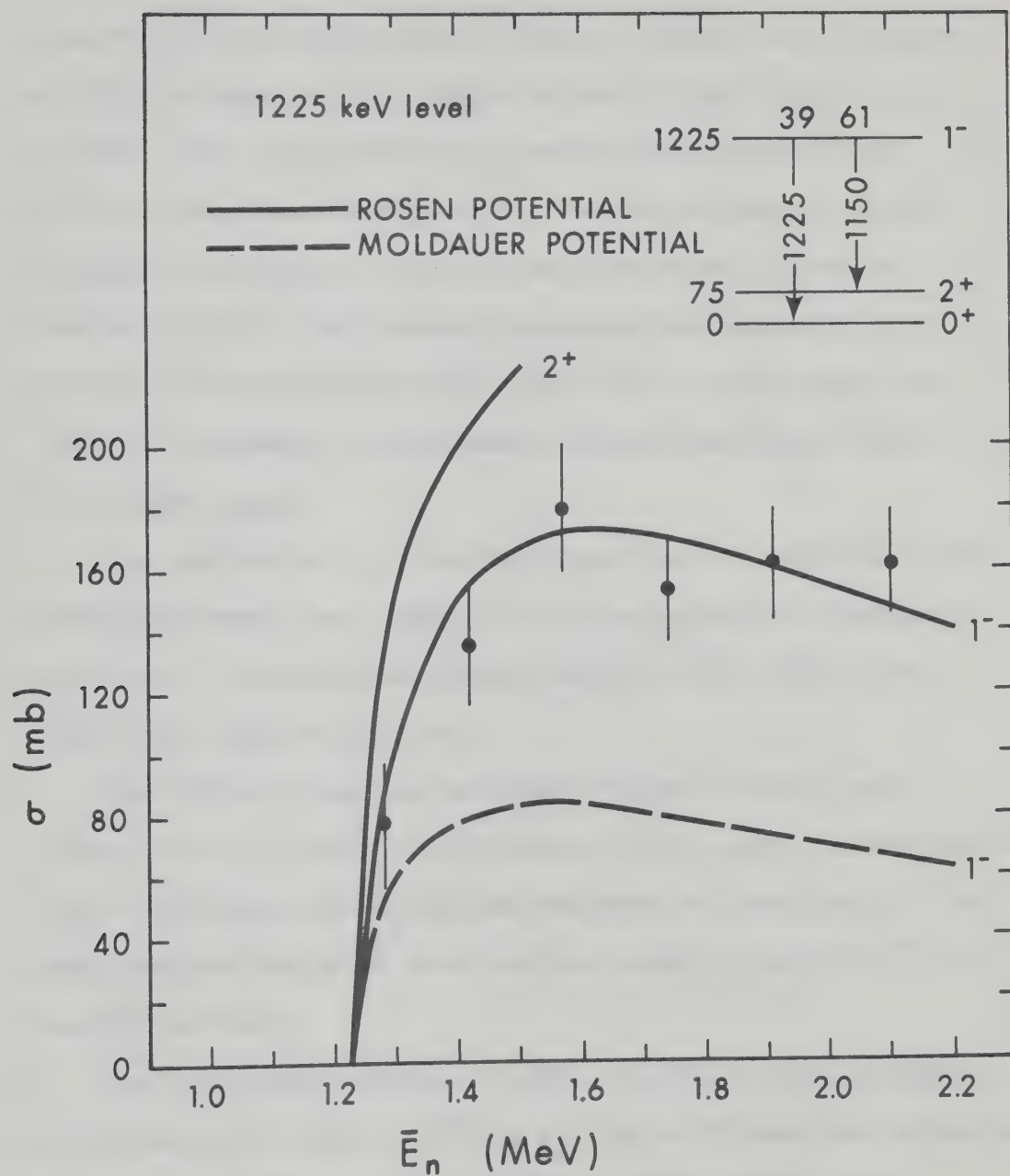








Figure 4.17      Excitation curve of the 1225 keV level.





Branching ratios determined at different energies have indicated a slight increase in the strength of the 1215 keV  $\gamma$ -ray at  $E_n \approx 1.5$  MeV. This can be noticed in the excitation curve of the 1215 keV  $\gamma$ -ray shown in fig. 4.18. The 1215 keV was partially assigned to the decay of the previously reported  $3^-$  level at 1464 keV (B1 67). The observed decay mode and inelastic cross sections for the 1290 keV state (fig. 4.18) are consistent with a  $J^\pi = 3^-$  assignment, in agreement with previous results (B1 67).

#### 4.4.5 Other levels

The observation of  $\gamma$ -rays which could not be fitted into the previously known level scheme of  $^{160}\text{Gd}$  indicates the existence of new levels. Therefore, we propose levels at 1262, 1351, 1378, 1381, 1569, 1587 and 1591 keV.

The 1262 keV level was observed to decay to the  $2^+$  and  $4^+$  states of the g.s. band via 1187 and 1013 keV  $\gamma$ -rays, respectively. Fig. 4.19 displays the excitation functions of these  $\gamma$ -rays. The decay mode and inelastic cross sections suggest a spin of  $4^+$  for the 1262 keV level.

Two  $\gamma$ -rays with energies of 1351 and 1276 keV were assigned to the decay of a level at 1351 keV. Fig. 4.20 shows the excitation curve of this level. A good agreement between measured and calculated cross sections was obtained for  $J^\pi = 1^-$ .

A  $\gamma$ -ray doublet of 1303 and 1306 keV was observed at neutron energies around 1.4 MeV. Fig. 4.21 displays the excitation function







Figure 4.18      Excitation curves of the 1215 keV  $\gamma$ -ray and the 1290 keV level.

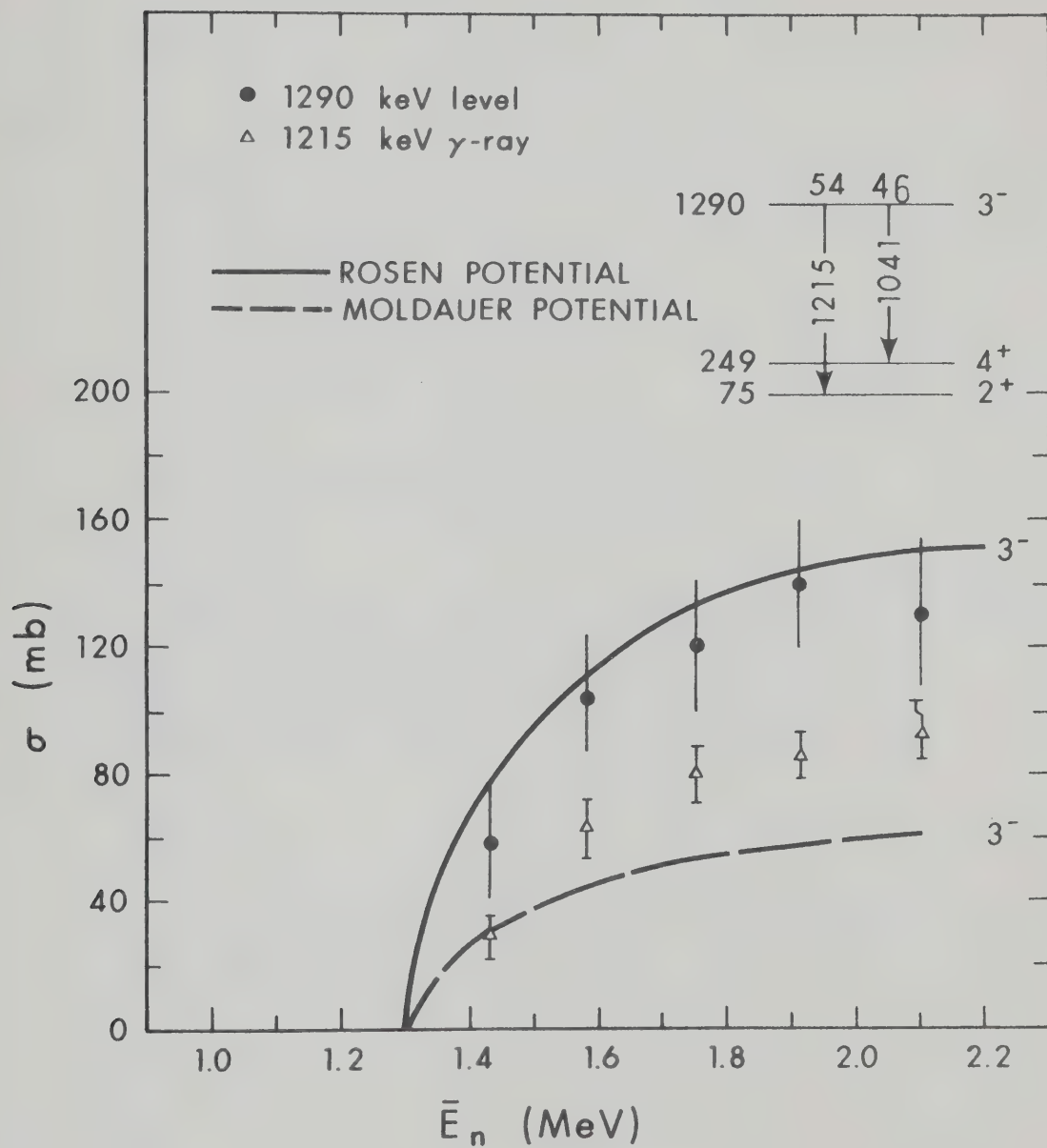






Figure 4.19      Excitation curves of the 1187 and 1013 keV  $\gamma$ -rays depopulating the 1262 keV level. Solid points are the total inelastic cross sections.

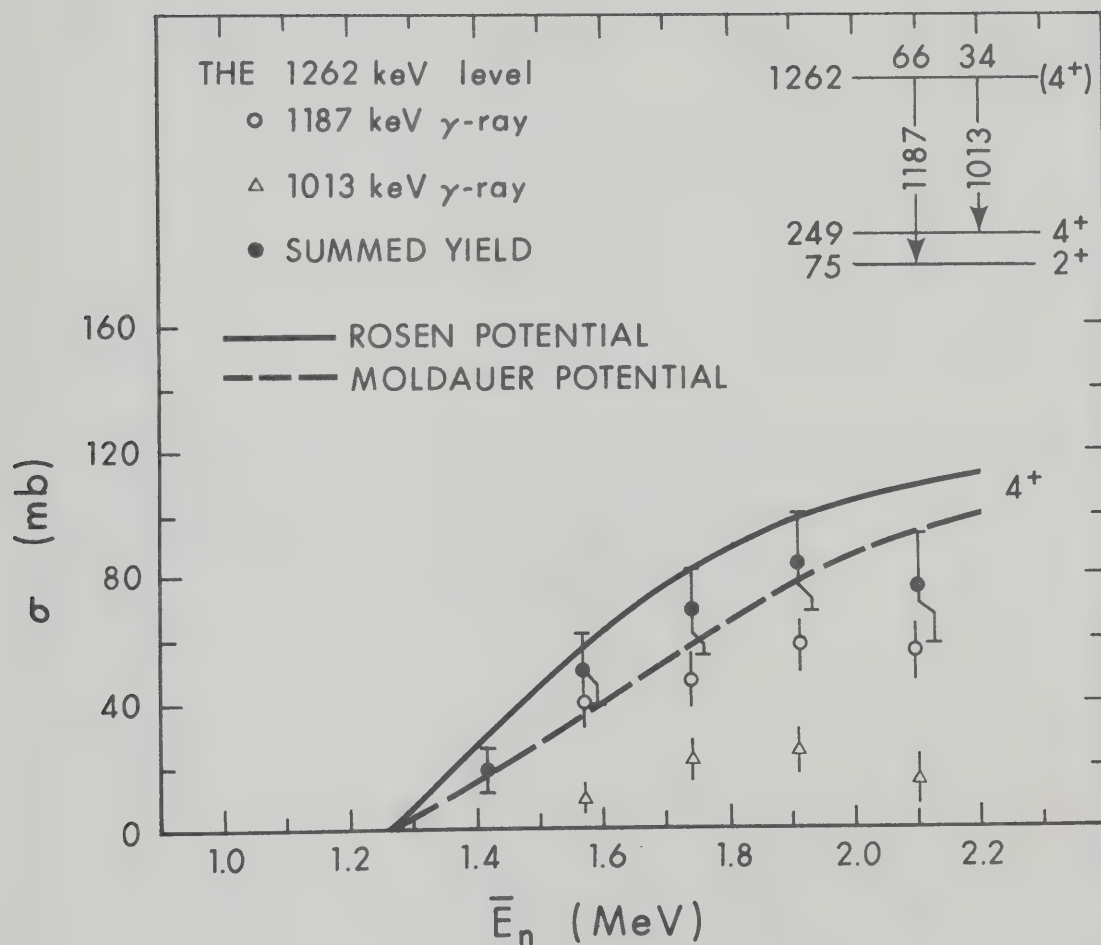








Figure 4.20      Excitation curve of the 1351 keV level. The solid line is the theoretical prediction based on Rosen potential and for  $J^\pi = 1^-$ .

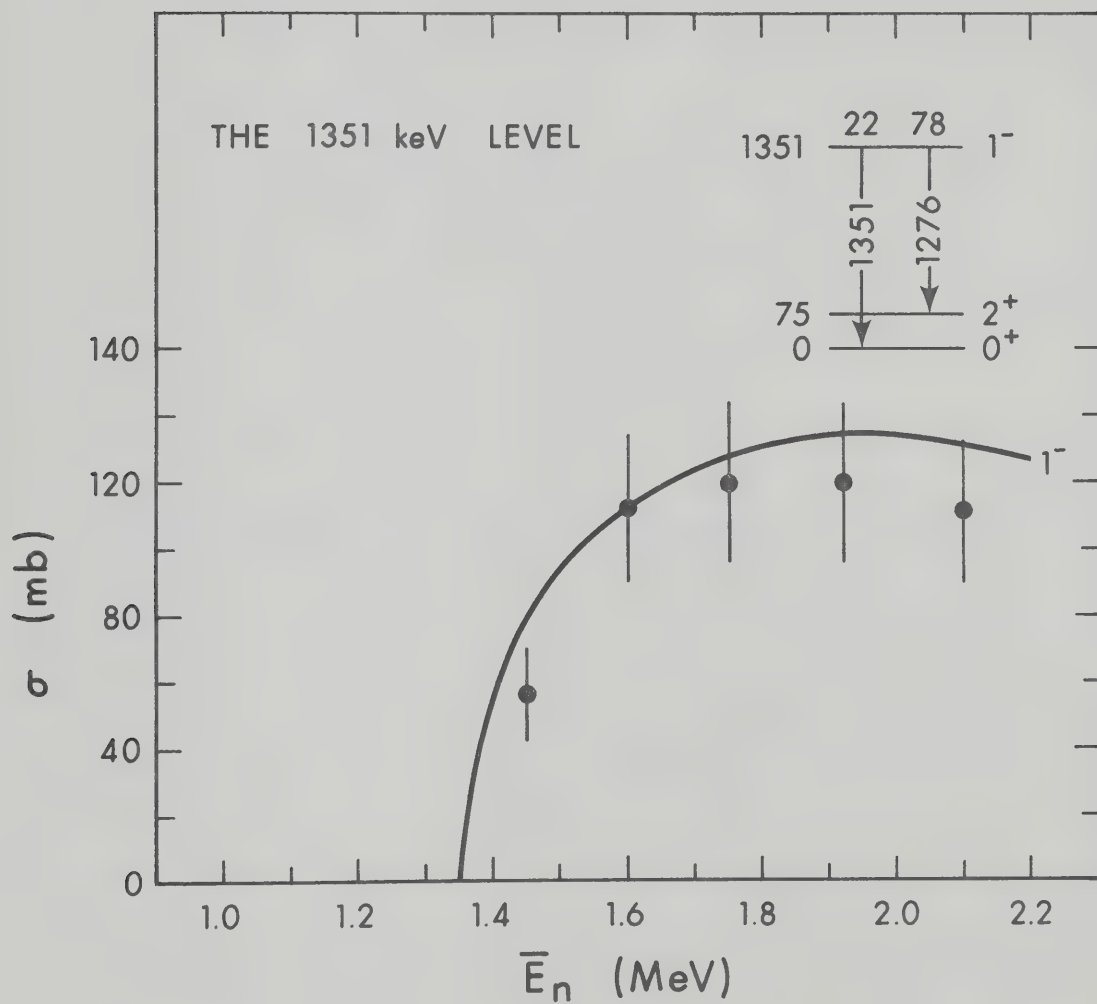
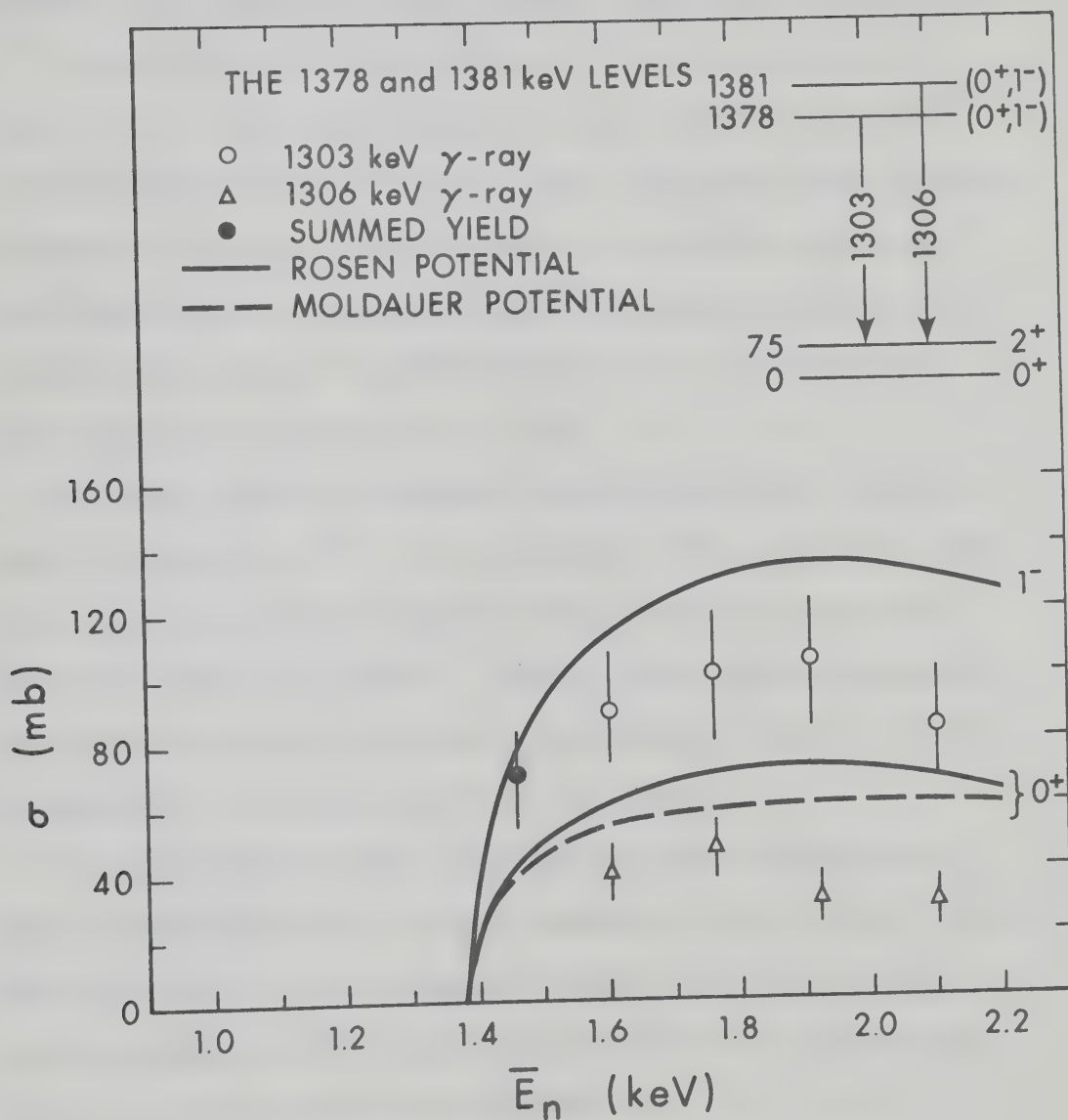






Figure 4.21      Excitation curves of the 1303 and 1306 keV  
γ-rays





of these  $\gamma$ -rays. They were assigned to the decay of two levels at 1378 and 1381 keV to the  $2^+$  state of the g.s. band. The measured cross sections for the 1378 keV level can be fitted with a  $1^-$  curve scaled by a factor of 0.8 or  $0^+$  curve scaled by a factor of 1.4. The cross sections for the 1381 keV level could not be fitted with either  $0^+$  or  $1^-$  curve. No other  $\gamma$ -rays could be assigned to the decay of these levels. It should be mentioned that because of the close proximity of the 1303 and 1306 keV  $\gamma$ -rays the extracted yield of the weak 1306 keV  $\gamma$ -ray was subjected to large statistical uncertainties ( $\sim 30\%$ )

No  $\gamma$ -rays could be identified from the previously reported  $5^-$  level at 1426 keV (B1 67). The production cross section of  $\gamma$ -rays from this level to the  $4^+$  state of the g.s. band is, as we have seen in the case of Sm, small. The fact that the weight of the Sm sample was twice that of the Gd possibly explains why we were able to see the  $5^- \rightarrow 4^+$  transition in the case of Sm.

The 1389 and 1215 keV  $\gamma$ -rays were assigned to the decay of a level at 1464 keV to the  $2^+$  and  $4^+$  members of the g.s. band. This level has previously been observed in (p,p') and (d,d') studies and was assigned by the latter a value of  $J^\pi = 3^-$ . The observed decay is consistent with this assignment.

The existence of levels at 1569, 1587 and 1591 keV was based on the observation of de-excitation  $\gamma$ -rays from these levels to the  $0^+$  and  $2^+$  states of the g.s. band.





No quantitative analysis has been made for levels above 1400 keV excitation due to the weakness of the observed  $\gamma$ -rays.

#### 4.4.6 Level scheme and band structure of $^{160}\text{Gd}$

The decay scheme of  $^{160}\text{Gd}$  revealed from the present study is shown in fig. 4.22, together with previous (p,p') and (d,d') results. The doubted levels at 946 and 1016 keV reported in the (d,d') work of Bloch et al. (Bl 67) were not seen in the present experiment. Except for the  $5^-$  level at 1426 keV observed in the (d,d') study, we have identified de-excitation  $\gamma$ -rays from all the previously reported levels in the 900 to 1600 keV excitation region. In addition, seven new states have been proposed and included in the level scheme of  $^{160}\text{Gd}$ .

Analysis of the present results has confirmed the previous spin assignment of  $2^+$  and  $3^-$  for the levels at 989 and 1290 keV, respectively. Also, the spins of the 1058 and 1225 keV states have been determined to be  $3^+$  and  $1^-$ , respectively. The new level at 1351 keV has been assigned a  $J^\pi = 1^-$ . In addition, tentative spin assignments have been made for the other levels shown in fig. 4.22.

Rotational bands built on the  $\gamma$ - and octupole vibrational modes were suggested by Bloch et al. (Bl 67). The present study has completed the information about members of these bands as indicated in fig. 4.22. No evidence of the  $\beta$ -band was found. This situation is similar to that reported in the case of  $^{158}\text{Gd}$  (Sh 71). The  $3^-$  level at 1464 keV might be a  $K = 1$  octupole





Figure 4.22      Level decay scheme of  $^{160}\text{Gd}$ . Members of octupole and  $\gamma$ -bands are also shown. The previous (p,p') and (d,d') results are from Shelton (Sh 66) and Bloch et al. (Bl 67), respectively.





vibration. The  $1^-$  member of the associated rotational band could be either the 1351 or 1378 keV level.

#### 4.5 Interpretation of Results in Terms of the Collective Model

##### 4.5.1 Background

According to the collective model of Bohr and Mottelson (Bo 53), nuclei whose equilibrium shape deviates from spherical symmetry can undergo two essentially different modes of excitation -- rotational and intrinsic. The former is associated with a collective motion which affects the orientation in space; the latter may be associated with the excitation of individual particles or with collective vibrations of the nuclear surface. Two assumptions were made:

- (i) The nuclear shape is axially symmetric. Thus the rotational motion can be characterized by the quantum numbers  $I$ ,  $K$  and  $M$  representing the angular momentum, its projection on the nuclear symmetry axis, and its projection on the space-fixed axis, respectively.
- (ii) The rotational and intrinsic motions of the nucleus do not disturb each other. This adiabatic assumption corresponds to the existence of an approximate nuclear wave function given by a simple product of the intrinsic and rotational wave functions.

The states in a rotational band are characterized by the same intrinsic wave function and are labelled by different values of  $I$ .





In an even-even nucleus, the ground state has  $K = 0$  and symmetrization of the wavefunction limits the rotational band to

$$I^\pi = 0^+, 2^+, 4^+, 6^+, \dots$$

The energies of these states are, to the first order

$$E_I = \frac{\hbar^2}{2\mathcal{I}} \{I(I+1)\} \quad [4.2]$$

where  $\mathcal{I}$  is the moment of inertia that depends on the nuclear deformation.

Vibrations of axially symmetric deformed nuclei may be characterized by the quantum number  $\lambda$  corresponding to the multipole order for small nuclear eccentricities [the parity of the vibration is  $(-1)^\lambda$ ] and by  $\nu$ , corresponding to the component of vibrational angular momentum around the symmetry axis. The lowest lying vibrations of a deformed axially symmetric nucleus are quadrupole vibrations,  $\lambda = 2$  ( $\beta$ -vibrations) and one with  $\nu = 2$  ( $\gamma$ -vibrations).  $\nu = \pm 1$  can be shown to be the same as a rotation.

Thus the  $\beta$ -vibration, having  $K = 0$ , is an axially symmetric vibration in which the eccentricity of the ellipsoid of revolution changes. In the  $\gamma$ -vibration, the axial symmetry is destroyed,  $K = 2$ ; that is if one looks along the symmetry axis, the outline is an ellipse.



In deformed nuclei the lowest lying negative parity vibrations should be octupole vibrations ( $\lambda = 3$ ,  $\nu = 0, \pm 1, \pm 2, \pm 3$ ). On the other hand, for a spherical nucleus the strength of this vibrational mode should be concentrated in a single  $I^\pi = 3^-$  state. Octupole vibrations with  $K = 0$  and  $I = 1^-, 3^-, 5^-$ , etc. have been observed in many deformed nuclei.

Deformed spheroidal nuclei can simultaneously rotate and vibrate. Thus, for each vibrational mode there is a band of rotational states whose energies are given by

$$E_I = \frac{\hbar^2}{2\mathcal{J}} [I(I + 1) - K^2] \quad [4.3]$$

since  $K$  is the  $z$ -component of  $I$ ,  $I$  must be equal to or greater than  $K$ . The lowest energy state is then the one with  $I = K$ . For  $\gamma$ -vibrations  $K = 2$ , so the values of  $I^\pi = 2^+, 3^+, 4^+, \dots$  and for  $\beta$ -vibrations  $K = 0$ , where the values of  $I^\pi$  are  $0^+, 2^+, 4^+$ , etc.

The adiabatic assumption of Bohr and Mottelson allows the reduced transition probability of a given multipole radiation  $L$  between two states to be expressed as a geometrical factor depending only on the angular momenta  $I$ ,  $K$  and  $L$ , and a matrix element involving integrations over the intrinsic wave function of the initial and final states. When one compares the reduced transition probability from a state  $i$  to different members  $f, f', \dots$  of a rotational family, the factor involving the intrinsic



wave functions is the same. One thus obtains (A1 55)

$$\frac{B(L, I_i K_i \rightarrow I_f K_f)}{B(L, I_i K_i \rightarrow I_f, K_f)} = \frac{\langle I_i L K_i \ K_f - K_i | I_f K_f \rangle^2}{\langle I_i L K_i \ K_f - K_i | I_f, K_f \rangle^2} \quad [4.4]$$

where  $\langle \rangle$  is the Clebsch - Gordan coefficient for the addition of angular momenta  $I_i$  and  $L$  to form the resultant  $I_f$ . This relation, of course, also holds where the states  $i$  and  $f$ ,  $f'$  belong to the same rotational band.

The simple separation of intrinsic excitations and collective rotations can be realized in the limit of large deformations, where the rotational motion is so slow that it does not disturb the nucleonic configuration or distort the nuclear shape. With decreasing deformation and increasing rotational frequency, the intrinsic structure is excited by the rotation motion, and the intrinsic quantum numbers are no longer constants of motion. This implies a modification in both the rotational spectrum (4.1) and the transition probability ratios (4.3). The correction term for rotational energies is usually taken to be proportional to  $I^2 (I + 1)^2$ , as is characteristic of the rotation-vibration interaction in molecules. The modified  $B(E2)$  for a transition from, say, the  $\beta$ -band to the ground state band can be written as, to the first order in spin-dependence (Fr 69)



$$B(E2; K=0, I_\beta \rightarrow K=0, I_g) = \langle 1020 | I_g 0 \rangle^2 |M_1^\beta|^2 \{1 + z_\beta [I_g(I_g+1) - I_\beta(I_\beta+1)]\}^2 \quad [4.5]$$

where  $M_1^\beta$  is the leading-order matrix element that connects the  $\beta$ -band with the ground state band, and  $z_\beta$  is called the band mixing parameter. A similar expression can be derived for the  $\gamma$ -band mixing with the ground state. Assuming that the intrinsic quadrupole moments for bands are equal, then  $z_\beta$  and  $z_\gamma$  can be determined from a ratio between relative  $B(E2)$  values of two transitions depopulating a particular  $\beta$ - or  $\gamma$ -band level. The magnitude of these mixing parameters provides a measure of the adequacy of the adiabatic assumption.

#### 4.5.2 Comparison of experimental and theoretical $B(EL)$ ratios

Using the branching ratios listed in tables 4.2 and 4.3, a series of transition probability ratios were calculated for  $\gamma$ -rays connecting vibrational bands with the ground state rotational band. For transitions which might contain an ML component, it was assumed that it is small and can be neglected. This is reasonable since the transition probability of the competing EL is large.

The experimental  $B(EL)$  ratios for  $\gamma$ -rays depopulating the octupole band observed in  $^{154}\text{Sm}$  and  $^{160}\text{Gd}$  are compared in table 4.4 with the predictions of the adiabatic intensity rule (eq. 4.4). Good agreement is obtained for a  $K = 0$  assignment.

Table 4.5 shows the results for the  $\gamma$ -band. The mixing parameter  $z_\gamma$  was obtained using eq. (4.5). Bés et al. (Be 65) have calculated  $z_\gamma$  for  $^{154}\text{Sm}$  and  $^{160}\text{Gd}$  to be 0.04 and 0.025, respectively.





TABLE 4.4

Experimental and theoretical ratios of transition probabilities  
from members of the octupole band in  $^{154}\text{Sm}$  and  $^{160}\text{Gd}$

Nucleus	$\frac{I_0 \rightarrow I_g}{I_0 \rightarrow I'_g}$	$B(E1; I_0 \rightarrow I_g)/B(E1; I_0 \rightarrow I'_g)$		
		Experiment		Theory <sup>a</sup>
		This work	D'Auria <u>et al.</u>	
<sup>154</sup> Sm	$\frac{1^- \rightarrow 2^+}{3^- \rightarrow 4^+}$	1.83 $\pm$ 0.1	1.96	1.997
	$\frac{3^- \rightarrow 4^+}{3^- \rightarrow 2^+}$	1.19 $\pm$ 0.06	1.25	1.33
<sup>160</sup> Gd	$\frac{1^- \rightarrow 2^+}{3^- \rightarrow 4^+}$	2.07 $\pm$ 0.1		1.997
	$\frac{3^- \rightarrow 4^+}{3^- \rightarrow 2^+}$	1.32 $\pm$ 0.07		1.33

a) Predictions from adiabatic symmetric-rotor model (eq. 4.4).



TABLE 4.5

Experimental and theoretical ratios of transition probabilities  
from members of the  $\gamma$ -band in  $^{154}\text{Sm}$  and  $^{160}\text{Gd}$

Nucleus	$\frac{I_\gamma \rightarrow I_g}{I_\gamma \rightarrow I'_g}$	$B(E2; I_\gamma \rightarrow I_g)/B(E2; I_\gamma \rightarrow I'_g)$			$Z_\gamma \times 10^2$
		Experiment		Theory <sup>a</sup>	
		This work	D'Auria <u>et al.</u>		
<sup>154</sup> Sm	$\frac{3^+ \rightarrow 4^+}{3^+ \rightarrow 2^+}$	$0.50 \pm 0.04$	0.4	0.4	$4.0 \pm 0.32$
	$\frac{2^+ \rightarrow 2^+}{2^+ \rightarrow 0^+}$	$1.82 \pm 0.11$	1.56	1.43	$4.0 \pm 0.25$
<sup>160</sup> Gd	$\frac{3^+ \rightarrow 4^+}{3^+ \rightarrow 2^+}$	$0.54 \pm 0.03$		0.4	$5.4 \pm 0.33$
	$\frac{2^+ \rightarrow 2^+}{2^+ \rightarrow 0^+}$	$1.75 \pm 0.1$		1.43	$3.3 \pm 0.20$
	$\frac{4^+ \rightarrow 4^+}{4^+ \rightarrow 2^+}$	$4.76 \pm 0.3$		2.94	$3.2 \pm 0.2$

a) Predictions from adiabatic symmetric-rotor model (eq. 4.4).



TABLE 4.6

Experimental and theoretical ratios of reduced E2 transition probabilities from members of the  $\beta$ -band in  $^{154}\text{Sm}$

$\frac{I_{\beta} \rightarrow I_g}{I_{\beta} \rightarrow I'_g}$	$B(E2; I_{\beta} \rightarrow I_g)/B(E2; I_{\beta} \rightarrow I'_g)$			$Z_{\beta} \times 10^2$
	Experiment		Theory <sup>a</sup>	
	This work	D'Auria <u>et al.</u>		
$\frac{2 \rightarrow 4}{2 \rightarrow 2}$	$2.13 \pm 0.16$	2.07	1.8	$0.63 \pm 0.05$
$\frac{2 \rightarrow 0}{2 \rightarrow 2}$	$0.45 \pm 0.03$	0.47	0.7	$3.3 \pm 0.2$
$\frac{2 \rightarrow 4}{2 \rightarrow 0}$	$4.74 \pm 0.33$	4.2	2.6	$1.6 \pm 0.1$
			Ave.	$1.8 \pm 0.1$

<sup>a</sup>) Predictions from adiabatic symmetric-rotor model (eq. 4.4).



The present values are in good agreement with these predictions.

The  $B(E2)$  ratios from members of the  $\beta$ -band in  $^{154}\text{Sm}$  are given in table 4.6. There is an apparent inconsistency with the angular momentum dependency of  $B(E2)$  ratios, which is characteristic of  $\beta$ -bands of nuclei in this region (Ri 69, Fr 69).

The values of  $Z_\beta$  and  $Z_\gamma$  obtained for  $^{154}\text{Sm}$  are  $\leq$  half those for  $^{152}\text{Sm}$  (Ri 69, Ru 71). This is expected since the latter nucleus is less deformed. Fraser et al. (Fr 69) and very recently Diamond et al. (Di 71) have determined the  $B(E2)$  values for transitions within the ground state band of  $^{154}\text{Sm}$ . They found that it is in good agreement with the adiabatic values and if there is mixing it is very small, thus, supporting the present results.

The smallness of band mixing parameters in  $^{154}\text{Sm}$  and  $^{160}\text{Gd}$  indicates that these nuclei can be represented by rigid rotors.





## CHAPTER V

### CONCLUSIONS

The small sample method that has been developed in the present study has proven to be very useful for the investigation of the  $(n,n'\gamma)$  reaction when only small quantities of the scattering material are available. It has been shown that the physical arrangement of source and scatterer used in this method performs a good energy average for inelastic cross sections, which can, therefore, be directly compared to the predictions of the statistical model.

Application of the method to the study of the structure of  $^{154}\text{Sm}$  and  $^{160}\text{Gd}$  has yielded information about excitation energies, principal decay modes and inelastic cross sections of levels in these nuclei. Interpretation of excitation functions in terms of the statistical model, together with the observed decay modes, has confirmed or determined level spins. The results are summarized in figs. 4.11 and 4.22.

A spherical optical model potential was found to be adequate in predicting inelastic cross sections on these highly deformed nuclei.

Previous reaction studies preferentially excited different levels in these nuclei. The fact that most of these levels were observed in the present experiment reflects the usefulness of the



'CN' (n,n') reaction in populating levels independent of their structure (subject, however, to energy, angular momentum and parity conservation restrictions).

Transition probability ratios obtained from the present study indicate that any coupling between the vibrational and rotational modes of excitation is very small. This means that the  $^{154}\text{Sm}$  and  $^{160}\text{Gd}$  nuclei are good rotors.

An improvement of the experimental method described in this thesis could be made. As mentioned in Chapter IV, the low-energy region of the  $\gamma$ -ray spectrum (below 500 keV) was badly masked by the intense  $\gamma$ -rays associated with the  $^7\text{Li} + p$  reaction that was used as a neutron source. By switching to the  $\text{T}(p,n)$  reaction it would be possible to obtain spectra free from these background  $\gamma$ -rays. Identification of low-energy  $\gamma$ -rays would be of assistance in assigning interband transitions and accounting for cascade feeding. However, other background problems would arise from the use of a tritium gas cell. For example, one would probably see neutron and proton induced  $\gamma$ -rays from the gas cell material.



## REFERENCES

- Al 55 G. Alaga, K. Alder, A. Bohr and B.R. Mottelson, Kgl. Danske Videnskab. Selskab, Mat.-Fys. Medd. 29, No. 9 (1955)
- Au 64 E.H. Auerbach and S.O. Moore, Phys. Rev. 135 (1964) B895
- Be 65 D.R. Bés, P. Federman, E. Magueda and A. Zuker, Nucl. Phys. 65 (1965) 1
- Be 66 R.W. Benjamin, P.S. Buchanan and I.L. Morgan, Nucl. Phys. 79 (1966) 241
- Be 69 F.D. Becchetti and G.W. Greenlees, Phys. Rev. 182 (1969) 1190
- Bj 66 J.H. Bjerregaard, O. Hansen, O. Nathan and S. Hinds, Nucl. Phys. 86 (1966) 145
- Bl 52 J.M. Blatt and V.F. Weisskopf, *Theoretical Nuclear Physics* (J. Wiley and Sons, New York, 1952) p. 394
- Bl 67 R. Bloch, B. Elbek and P.O. Tjom, Nucl. Phys. A91 (1967) 576
- Bo 53 A. Bohr and B.R. Mottelson, Kgl. Danske Videnskab. Selskab, Mat.-Fys. Medd. 27, No. 16 (1953) (Second edition, 1957)
- Da 52 C.M. Davisson and R.D. Evans, Revs. Mod. Phys. 24 (1952) 79
- Da 71 J.M. D'Auria, D. Ostrom and S.C. Gujrathi, Nucl. Phys. A178 (1971) 172
- Di 72 R.M. Diamond, G.D. Symons, J.S. Quebert, K.H. Maier, J.R. Leigh and F.S. Stephens, Nucl. Phys. A184 (1972) 481
- Ea 72 J.F. Easton and W.K. Dawson, University of Alberta, Nuclear Research Centre Internal Report UAE-NPL-38 (1972)
- El 69 S.A. Elbakr, M.Sc. thesis, University of Alberta (1969)



- El 72 S.A. Elbakr, University of Alberta, Nuclear Research Centre  
Internal Report UAE-NPL-49 (1972)
- Fr 55 F.L. Friedman and W. Weisskopf, "The Compound Nucleus", *Niels Bohr and the Development of Physics*, ed. W. Pauli with the assistance of L. Rosenfeld and W. Weisskopf (Pergamon Press, London, 1955) p. 134
- Fr 69 I.A. Fraser, J.S. Greenberg, S.H. Sie, R.G. Stockstad, G.A. Burginyon and D.A. Bromley, *Phys. Rev. Lett.* 23 (1969) 1047
- Gi 65 W.B. Gilboy and J.H. Towle, *Nucl. Phys.* 64 (1965) 130
- Gi 65a A. Gilbert and A.G.W. Cameron, *Can. J. Phys.* 43 (1965) 1446
- Go 63 M.D. Goldberg, *Progress in Fast Neutron Physics*, eds. G.C. Phillips et al. (The University of Chicago Press, Chicago, 1963) p. 3
- Go 66 M.D. Goldberg, et al. Brookhaven National Laboratory Report, BNL 325 (1966)
- Ha 52 W. Hauser and H. Feshbach, *Phys. Rev.* 87 (1952) 366
- Ha 63 O. Hansen and O. Nathan, *Nucl. Phys.* 42 (1963) 197
- Ke 64 R.A. Kenefick and R.K. Sheline, *Phys. Rev.* 135 (1964) B939
- Ku 67 K. Kumar, *Nucl. Phys.* A92 (1967) 653
- La 57 A.M. Lane and J.E. Lynne, *Proc. Phys. Soc.* 70 (1957) 557
- Mo 63 P.A. Moldauer, *Nucl. Phys.* 47 (1963) 65
- Mo 64 P.A. Moldauer, *Revs. Mod. Phys.* 36 (1964) 1079
- Mo 64a P.A. Moldauer, C.A. Engelbrecht and G.J. Duffy, Argonne National Laboratory Report ANL-6978 (1964)
- Pe 62 F.G. Perey and B. Buck, *Nucl. Phys.* 32 (1962) 353
- Po 56 C.E. Porter and R.G. Thomas, *Phys. Rev.* 104 (1956) 483





- Ri 69 L.L. Riedinger and N.R. Johnson, Phys. Rev. 179 (1969) 1214
- Ro 66 L. Rosen, J.G. Beery, A.S. Goldhaber and E.H. Auerbach, Ann. Phys. 34 (1966) 96
- Ro 72 B.C. Robertson (private communication)
- Ru 71 N. Rud, H.L. Neilsen and K. Wilsky, Nucl. Phys. A167 (1971) 140
- Se 66 G.G. Seaman, J.S. Greenberg, D.A. Bromley and F.K. McGowan, Phys. Rev. 149 (1966) 925
- Sh 66 W.N. Shelton, Phys. Lett. 20 (1966) 651
- Sh 72 H.S. Sherif, S.A. Elbakr and J. Korte, University of Alberta, Nuclear Research Centre Internal Report UAE-NPL-48 (1972)
- Sm 68 A.B. Smith, P.T. Guenther and J.F. Whalen, Phys. Rev. 168 (1968) 1344
- Tu 65 A.B. Tucker, J.T. Wells and W.E. Meyerhof, Phys. Rev. 137 (1965) B1181
- Va 55 J.J. van Loef and D.A. Lind, Phys. Rev. 10 (1956) 103
- Ve 68 E. Veje, B. Elbek, B. Herskind and M.C. Olesen, Nucl. Phys. A109 (1968) 489
- Vo 68 E. Vogt, *Advances in Nuclear Physics*, ed. M. Baranger and E. Vogt, Vol. 1 (Plenum Press, New York, 1968) p. 261
- Wi 64 D. Wilmore and P.E. Hodgson, Nucl. Phys. 55 (1964) 673
- Yo 65 Y. Yoshizawa, B. Elbek, B. Herskind and M.C. Olesen, Nucl. Phys. 73 (1965) 273
- Ze 66 B. Zeidman, B. Elbek, B. Herskind and M.C. Olesen, Nucl. Phys. 86 (1966) 471



## APPENDIX A



MEASUREMENTS OF NEUTRON ANGULAR DISTRIBUTIONS  
FROM THE  ${}^7\text{Li}(\text{p},\text{n}){}^7\text{Be}$  REACTION<sup>†</sup>

*S.A. Elbakr, I.J. van Heerden\*, W.J. McDonald  
and G.C. Neilson*

Nuclear Research Centre  
The University of Alberta  
Edmonton, Alberta, Canada

The absolute zero-degree differential cross sections of the  ${}^7\text{Li}(\text{p},\text{n}_0){}^7\text{Be}$  and the  ${}^7\text{Li}(\text{p},\text{n}_1){}^7\text{Be}$  reactions have been measured with a time-of-flight spectrometer at 0.1 MeV intervals from 2.20 to 5.50 MeV. Angular distributions of neutrons from both reactions were also measured at 0.2 MeV intervals from 2.60 to 5.40 MeV for the  $\text{n}_0$  neutron group and from 3.20 to 5.40 MeV for the  $\text{n}_1$  group. Absolute differential cross sections were obtained by normalization to the zero-degree measurement. The centre-of-mass distributions were fitted with a Legendre polynomial series. Total cross sections were obtained by integrating the angular distributions. The comparison between present and previous results has revealed some disagreement in the shapes of angular distributions and in the magnitude of total cross sections for the  ${}^7\text{Li}(\text{p},\text{n}_1){}^7\text{Be}$  reaction.

---

<sup>†</sup>This work supported in part by the Atomic Energy Control Board of Canada.

\* Present address: Southern Universities Nuclear Institute, Faure, South Africa



## 1. Introduction

The  ${}^7\text{Li}(p,n){}^7\text{Be}$  reaction has been used in the University of Alberta laboratory to study  $(n,n'\gamma)$  reactions using small scattering samples in a close geometry<sup>1)</sup>. Analysis of the  $\gamma$ -ray data requires an accurate knowledge of the neutron angular distributions. The published information on the neutron angular distributions<sup>2,3)</sup> was not sufficiently complete or accurate enough for the analysis of our  $(n,n'\gamma)$  data. To generate a complete set of angular distributions, a systematic measurement of the absolute differential cross section as a function of both energy and angle for the  ${}^7\text{Li}(p,n_0){}^7\text{Be}$  and  ${}^7\text{Li}(p,n_1){}^7\text{Be}$  reactions has been carried out at proton energies from 2.60 to 5.40 MeV and laboratory angles between  $0^\circ$  and  $150^\circ$ . The measured angular distributions were fitted with a Legendre polynomial series yielding a set of coefficients at the different proton energies to be used in calculating differential cross sections at any angle in this energy range.

## 2. Experimental procedure

The measurements were made with neutron time-of-flight spectrometers using pulsed proton beams from the 6 MV Van de Graaff accelerators of the University of Alberta and of the Southern Universities Nuclear Institute (SUNI).

At Alberta, the absolute differential cross sections of the  ${}^7\text{Li}(p,n_0){}^7\text{Be}$  and  ${}^7\text{Li}(p,n_1){}^7\text{Be}^*$  reactions were measured at zero degree for proton energies from 2.20 to 5.50 MeV at 0.1 MeV intervals.





Angular distribution measurements at  $20^\circ$  intervals were then made at proton energies from 2.60 to 5.40 MeV for the  $n_0$  neutron group and from 3.20 to 5.40 MeV for the  $n_1$  neutron group.

The neutron time-of-flight system used has been previously described<sup>4</sup>). Top terminal pulsing and a Mobley bunching magnet provided proton pulses of  $\leq 0.5$  ns. The neutron detector consisted of a cylindrical glass cell 9.5 cm diameter x 1.9 cm thick filled with NE 213 liquid scintillator viewed by an RCA 4522 photo-multiplier, and was placed at a distance of 3.473 m from the target. General background was reduced by pulse shape discrimination and the overall time resolution of the spectrometer was about 1 ns.

The neutron detection efficiency was calculated using a Monte Carlo program written by N.R. Stanton<sup>5</sup>). This program was adapted for liquid scintillators by incorporating the data of Smith et al.<sup>6</sup>) for the light output from proton recoils in the NE 213 liquid scintillator. For each neutron energy the program gives the efficiency as a function of neutron detection threshold which was independently determined. The results of Chastel et al.<sup>7</sup>) have shown that the calculated efficiencies are in good agreement with measured values.

The lithium target was made by evaporating LiF on a 0.01 cm tantalum backing to a thickness of approximately  $200 \mu\text{g}/\text{cm}^2$ . The total thickness has been checked by measuring the width (FWHM) of a low energy neutron peak and subtracting in quadrature the time resolution of the spectrometer. The tables of Janni<sup>8</sup>) for proton



energy loss were then used to determine the target thickness in  $\text{mg}/\text{cm}^2$ . This gave a value agreeing to within 10% with that determined by weighing.

To ensure that the proton beam was positioned on the same target spot throughout the measurements, the beam was passed through a pre-target slit system. This consisted of two gold plates independently mounted on two micrometers and connected to two microammeters. A negative bias of 300V applied to each plate prevented secondary electrons from leaving the target. The Mobley magnet current was adjusted during the experiment to ensure a balanced minimum current on the plates.

For the excitation curve measurements a beam current integrator was used as a controlling monitor. The target was air-cooled. To check the internal consistency of the results and whether any target deterioration had taken place, various cross section determinations were repeated at randomly selected proton energies. No significant differences were observed.

For the angular distribution measurements a second time-of-flight system was used as a monitor. The neutron detector for the monitor system was positioned at a fixed angle of  $-30^\circ$  to the incident proton beam. It was found that for each angular distribution measurement, the ratio of monitor counts to total electric charge on target remained constant to within the statistics. This indicated that the target was probably uniform, and that the thickness determination by



weighing was justifiable. Relative cross sections were determined by normalizing the yield in the main detector, corrected for efficiency, to that in the monitor.

At SUNI the angular distributions were remeasured using a similar neutron time-of-flight spectrometer at the same proton energies as before. Top terminal pulsing and a klystron bunching system provided proton pulses of  $\sim 1.0$  ns. The main neutron detector was a cylindrical glass cell 12 cm diameter x 4 cm thick filled with NE 213 liquid scintillator mounted on a 58 AVP photo-multiplier and it was placed at a distance of 4.08 m from the target. Pulse shape discrimination reduced the general  $\gamma$ -ray background. A standard Hansen-McKibben long counter with known efficiency<sup>9)</sup> placed at  $90^\circ$  was used as monitor. The relative efficiency of the neutron detector was measured at low energies (threshold to 3.5 MeV) using neutrons from the  ${}^7\text{Li}(p,n){}^7\text{Be}$  reaction and direct comparison<sup>10,11)</sup> with the known response of the standard long counter.

It was found that the two sets of angular distribution measurements agree within statistics. They were then normalized to the zero-degree absolute differential cross sections.

### 3. Results and Discussion

Fig. 1 presents the zero-degree differential cross sections for both the ground state and first excited state groups. Statistical errors are  $\leq 3\%$ , while the error on absolute values is  $\pm 12\%$ . The





latter arises mainly from uncertainties in target thickness and detector efficiency determinations. The present results agree, within error, with the absolute values of Gabbard et al.<sup>1,2)</sup> for the zero-degree differential cross sections of all neutrons. They are also in fair agreement with the results of the relative cross section measurements of Bevington et al.<sup>2)</sup> and Borchers and Poppe<sup>3)</sup>.

The centre-of-mass angular distributions were fitted, using a least squares program, to a legendre polynomial series of the form:

$$\sigma(\theta) = \sum_n A_n P_n(\cos\theta) \quad [1]$$

Terms up to and including  $P_3$  were found sufficient to yield a good fit. Figs. 2 and 3 show the results where the smooth curves through the data are the least squares fits. Statistical errors on the data points are  $\leq 5\%$ . The coefficients resulting from the fits are given in Table 1.

The  $(p, n_0)$  angular distributions vary in a smooth manner from forward peaked at low energies to symmetric around  $90^\circ$  at energies exceeding 5.0 MeV. The  $(p, n_1)$  distributions tend to be peaked in a backward direction. In order to compare the shapes of the present angular distributions with those of Bevington et al.<sup>2)</sup> and Borchers and Poppe<sup>3)</sup>, we have fitted their results with our least squares program. The ratios  $A_n/A_0$  for both neutron groups are plotted as a function of proton energy in figs. 4 and 5. It is clear that





there is some disagreement between the present and previous results regarding the shapes of the angular distributions.

By integrating the Legendre series [1] over the solid angle, the total cross section is given by

$$\sigma_T = 4\pi A_0 \quad [2]$$

Total cross sections obtained using this equation are shown in fig. 6, where they are also compared with other measurements. The present measurements of the ground state total cross sections agree with the previous measurements of Bevington et al. and Borchers and Poppe, but for the first excited state the present total cross sections are about 20 - 30% smaller. Presser and Bass<sup>13)</sup> have also recently determined the total cross section for the (p,n<sub>1</sub>) reaction by measuring the 90° yield of the 0.431 MeV  $\gamma$ -ray. The present results are 13 - 22% smaller than their values.

In fig. 6 we have also compared the total cross sections for reactions leading to the ground and first excited states of <sup>7</sup>Be with the absolute measurements of Gibbons and Macklin<sup>14)</sup>. Their data were obtained by thermalization of neutrons in a large graphite sphere for which the absolute neutron efficiency was very accurately measured. The absolute cross sections were based on weighing a thick LiF target, 380  $\mu\text{g}/\text{cm}^2$ , and were accurate to  $\pm 5\%$ . The present total cross sections are accurate to  $\pm 12\%$ , and in general are smaller than those



of Gibbons and Macklin<sup>14</sup>) by  $\leq 10\%$  below 5 MeV, well within the uncertainties of the absolute cross section scales.

It is obvious that the ratios  $I_1/I_0$  of the intensities for the  $(p,n_1)$  and  $(p,n_0)$  total cross sections obtained in the present work are smaller than those obtained by Bevington et al.<sup>2)</sup> and by Borchers and Poppe<sup>3)</sup>. The ratios obtained at  $0^\circ$  in the present work and those obtained by the above authors and also by Cranberg<sup>15)</sup> are in good agreement with one another. Differences in the angular distributions obtained must therefore account for the differences in the  $I_1/I_0$  ratios for the total cross sections. The present data is based on two independent measurements of the same set of angular distributions. Although different methods were used to determine the relative efficiencies of the neutron detectors, the two sets of data were consistent within the errors. Furthermore, the present measurements were carried out with high resolution, low background time-of-flight spectrometers. We therefore feel that our results are more reliable than those of Bevington et al.<sup>2)</sup> and Borchers and Poppe<sup>3)</sup>.

One of the authors (I.J.v.H.) would like to express his thanks and appreciation to Professor G.C. Neilson of the Nuclear Research Centre, for hospitality during his stay in Edmonton, and to acknowledge a fellowship from the South African Council for Scientific and Industrial Research.



## References

- 1) S.A. Elbakr, I.J. van Heerden, W.K. Dawson, W.J. McDonald and G.C. Neilson; Nucl. Instr. and Meth. 97 (1971) 283.
- 2) P.R. Bevington, W.W. Rolland and H.W. Lewis; Phys. Rev. 121 (1961) 871.
- 3) R.R. Borchers and C.H. Poppe; Phys. Rev. 129 (1963) 2679.
- 4) W.J. McDonald and D.A. Gedcke, *Detection System for a Fast Neutron Time-of-Flight Spectrometer*, University of Alberta Internal Report UAE-NPL-966, Nuclear Research Centre.
- 5) N.R. Stanton, *A Monte Carlo Programme for Calculating Neutron Detection Efficiencies in Plastic Scintillators*, Ohio State University Preprint C00-1545-92 (Feb. 1971).
- 6) D.L. Smith, G.R. Polk and T.G. Miller; Nucl. Instr. and Meth. 64 (1968) 157.
- 7) A. Chastel, M.B. Davis, C.M. Hoffman, N.M. Kriesler and A.J.S. Smith; Nucl. Instr. and Meth. 94 (1971) 493.



- 8) J.F. Janni; Technical Report AFWL-TR-65-150, Air Force Weapons Laboratory, Kirtland Air Force Base, New Mexico.
- 9) W.D. Allen and A.T.G. Ferguson; Proc. Phys. Soc. 70A (1957) 639.
- 10) J.M. Adams, E. Barnard, A.T.G. Ferguson, W.R. McMurray and I.J. van Heerden; Nucl. Instr. and Meth. 34 (1965) 21.
- 11) S.G. Buccino, C.E. Hollandsworth and P.R. Bevington; Nucl. Phys. 53 (1964) 375.
- 12) Fletcher Gabbard, R.H. Davis and T.W. Bonner; Phys. Rev. 114 (1959) 201.
- 13) G. Presser and R. Bass; Nucl. Phys. A182 (1972) 321.
- 14) J.H. Gibbons and R.L. Macklin; Phys. Rev. 114 (1959) 571.
- 15) L. Cranberg; Los Alamos Scientific Laboratory Report LA 1654 (1954).





Table I

Legendre polynomial coefficients in mb/sr for

the centre-of-mass differential cross sections. Errors are statistical.

$E_p$ (LAB) (MeV)	${}^7\text{Li}(p,n_0){}^7\text{Be}$			${}^7\text{Li}(p,n_1){}^7\text{Be}$				
	$A_0$	$A_1$	$A_2$	$A_3$	$A_0$	$A_1$	$A_2$	$A_3$
2.60	$19.0 \pm 0.3$	$17.3 \pm 0.5$	$4.5 \pm 0.6$					
2.80	$19.1 \pm 0.3$	$14.0 \pm 0.4$	$2.8 \pm 0.6$					
3.00	$17.8 \pm 0.2$	$12.0 \pm 0.3$	$1.5 \pm 0.3$					
3.20	$17.6 \pm 0.2$	$11.2 \pm 0.3$	$2.0 \pm 0.3$		$4.25 \pm 0.08$	$-0.9 \pm 0.1$	$-0.7 \pm 0.1$	$-0.2 \pm 0.2$
3.40	$18.8 \pm 0.2$	$10.5 \pm 0.3$	$2.3 \pm 0.3$		$4.26 \pm 0.08$	$-1.1 \pm 0.1$	$-0.5 \pm 0.1$	$-0.2 \pm 0.2$
3.60	$18.5 \pm 0.2$	$9.1 \pm 0.3$	$2.2 \pm 0.3$	$-1.0 \pm 0.4$	$3.79 \pm 0.07$	$-1.2 \pm 0.1$	$0.2 \pm 0.1$	$0.0 \pm 0.2$
3.80	$18.1 \pm 0.2$	$7.2 \pm 0.3$	$2.5 \pm 0.3$	$-1.6 \pm 0.5$	$3.70 \pm 0.07$	$-1.3 \pm 0.1$	$0.6 \pm 0.1$	$-0.2 \pm 0.1$
4.00	$17.9 \pm 0.2$	$5.7 \pm 0.3$	$3.6 \pm 0.3$	$-2.1 \pm 0.5$	$3.20 \pm 0.06$	$-1.2 \pm 0.1$	$0.7 \pm 0.1$	$-0.2 \pm 0.1$
4.20	$19.5 \pm 0.2$	$5.0 \pm 0.3$	$6.0 \pm 0.$	$-4.5 \pm 0.5$	$3.13 \pm 0.05$	$-1.3 \pm 0.1$	$1.1 \pm 0.1$	$-0.5 \pm 0.1$
4.40	$21.2 \pm 0.2$	$5.1 \pm 0.4$	$8.7 \pm 0.4$	$-5.1 \pm 0.5$	$2.96 \pm 0.05$	$-1.3 \pm 0.1$	$1.1 \pm 0.1$	$-0.5 \pm 0.1$
4.60	$24.2 \pm 0.3$	$5.7 \pm 0.4$	$13.1 \pm 0.5$	$-5.2 \pm 0.6$	$2.88 \pm 0.05$	$-1.4 \pm 0.1$	$1.3 \pm 0.1$	$-0.5 \pm 0.1$
4.80	$26.5 \pm 0.4$	$5.3 \pm 0.8$	$15.3 \pm 0.9$	$-3.6 \pm 1.2$	$2.89 \pm 0.05$	$-1.3 \pm 0.1$	$1.4 \pm 0.1$	$-0.8 \pm 0.1$
5.00	$27.3 \pm 0.5$	$4.2 \pm 0.8$	$18.5 \pm 1.0$	$0.3 \pm 1.5$	$2.76 \pm 0.05$	$-1.2 \pm 0.1$	$1.5 \pm 0.1$	$-0.9 \pm 0.1$
5.20	$26.3 \pm 0.4$	$2.3 \pm 0.6$	$15.1 \pm 0.9$		$2.91 \pm 0.05$	$-0.8 \pm 0.1$	$1.6 \pm 0.1$	$-1.1 \pm 0.1$
5.40	$22.2 \pm 0.4$	$1.2 \pm 0.6$	$8.8 \pm 0.8$		$2.28 \pm 0.04$	$0.1 \pm 0.1$	$1.0 \pm 0.1$	$-0.7 \pm 0.1$



## Figure Captions

- Figure 1 Absolute zero-degree differential cross sections. The upper and lower curves are for neutrons leading to the ground and first excited states of  ${}^7\text{Be}$ , respectively. Absolute errors are represented by bars for the  $n_0$  neutron group and by the size of points for the  $n_1$  group.
- Figure 2 Centre-of-mass differential cross sections for the  ${}^7\text{Li}(p,n_0){}^7\text{Be}$  reaction. Each distribution is offset by a certain amount, so that the amount indicated at the right must be subtracted from the ordinate to obtain the correct magnitude.
- Figure 3 Centre-of-mass differential cross sections for the  ${}^7\text{Li}(p,n_1){}^7\text{Be}$  reaction. (See also caption of fig. 2).
- Figure 4 Legendre coefficients for the centre-of-mass angular distributions of the  ${}^7\text{Li}(p,n_0){}^7\text{Be}$  reaction.
- Figure 5 Legendre coefficients for the centre-of-mass angular distribution of the  ${}^7\text{Li}(p,n_1){}^7\text{Be}$  reaction.
- Figure 6 Total reaction cross sections. The data of Gibbons and Macklin<sup>11</sup>) were obtained by thermalization of neutrons in a large graphite sphere. All other data were obtained by integrating angular distribution of neutrons.



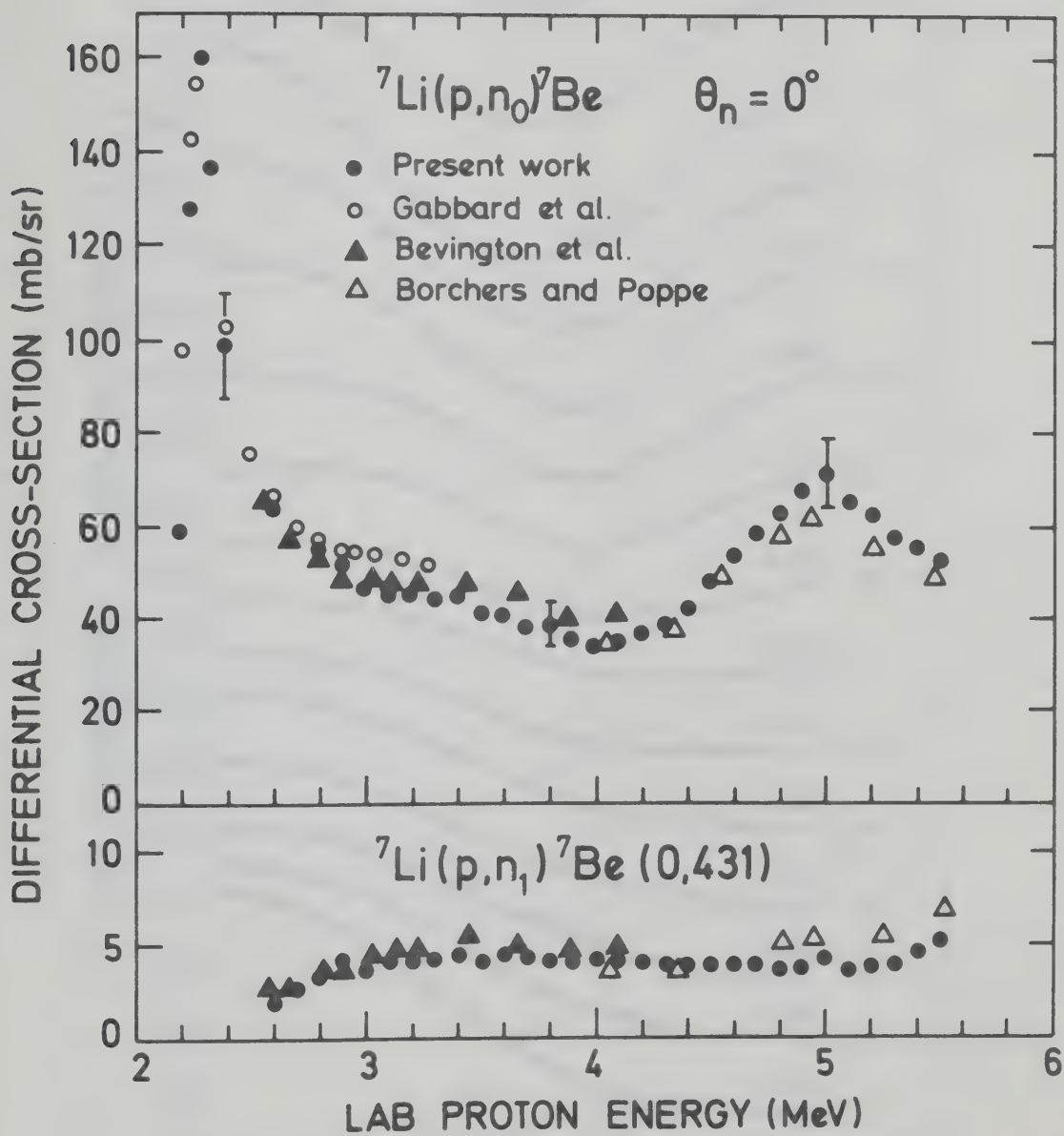


Figure 1



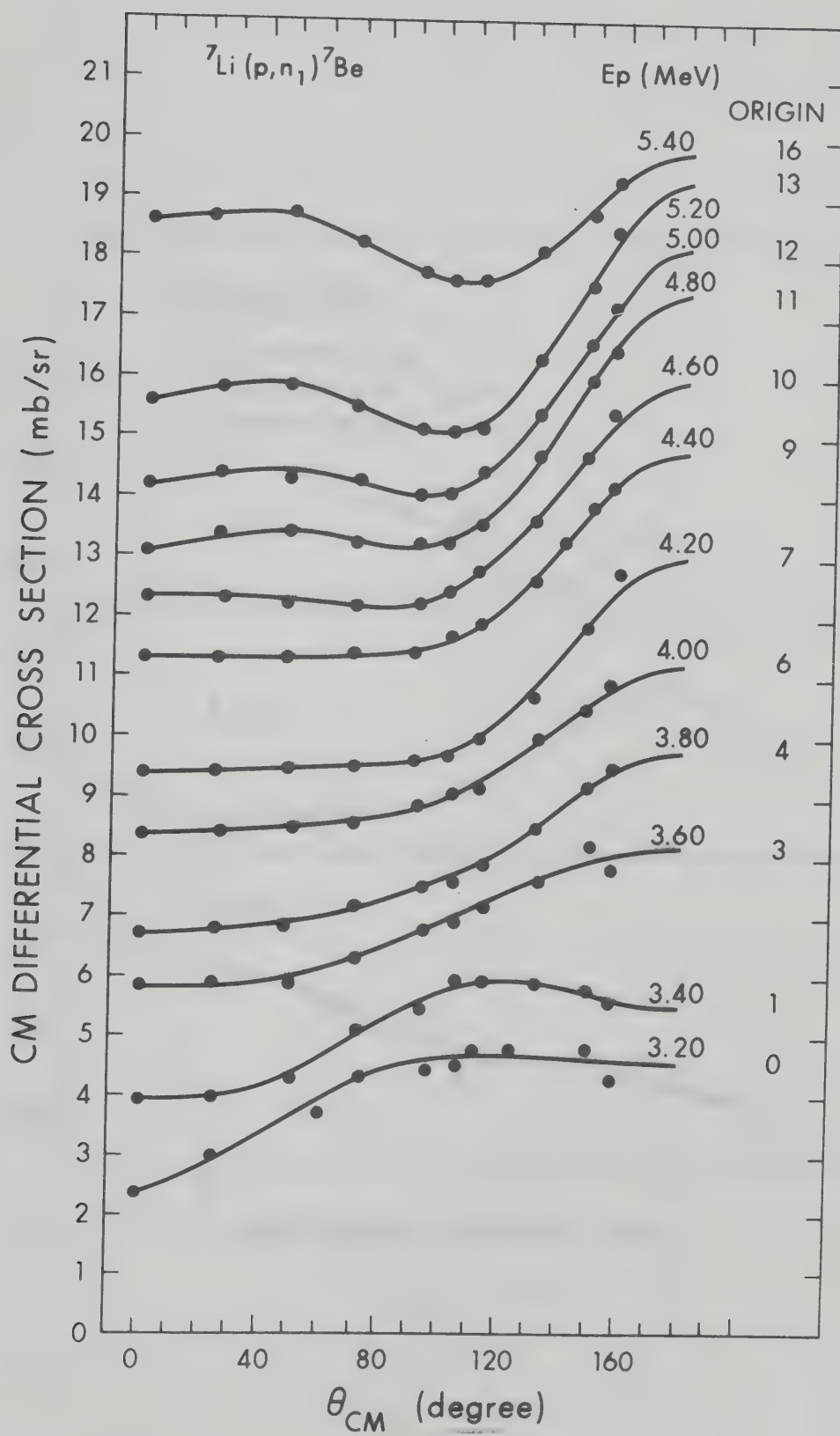


Figure 3





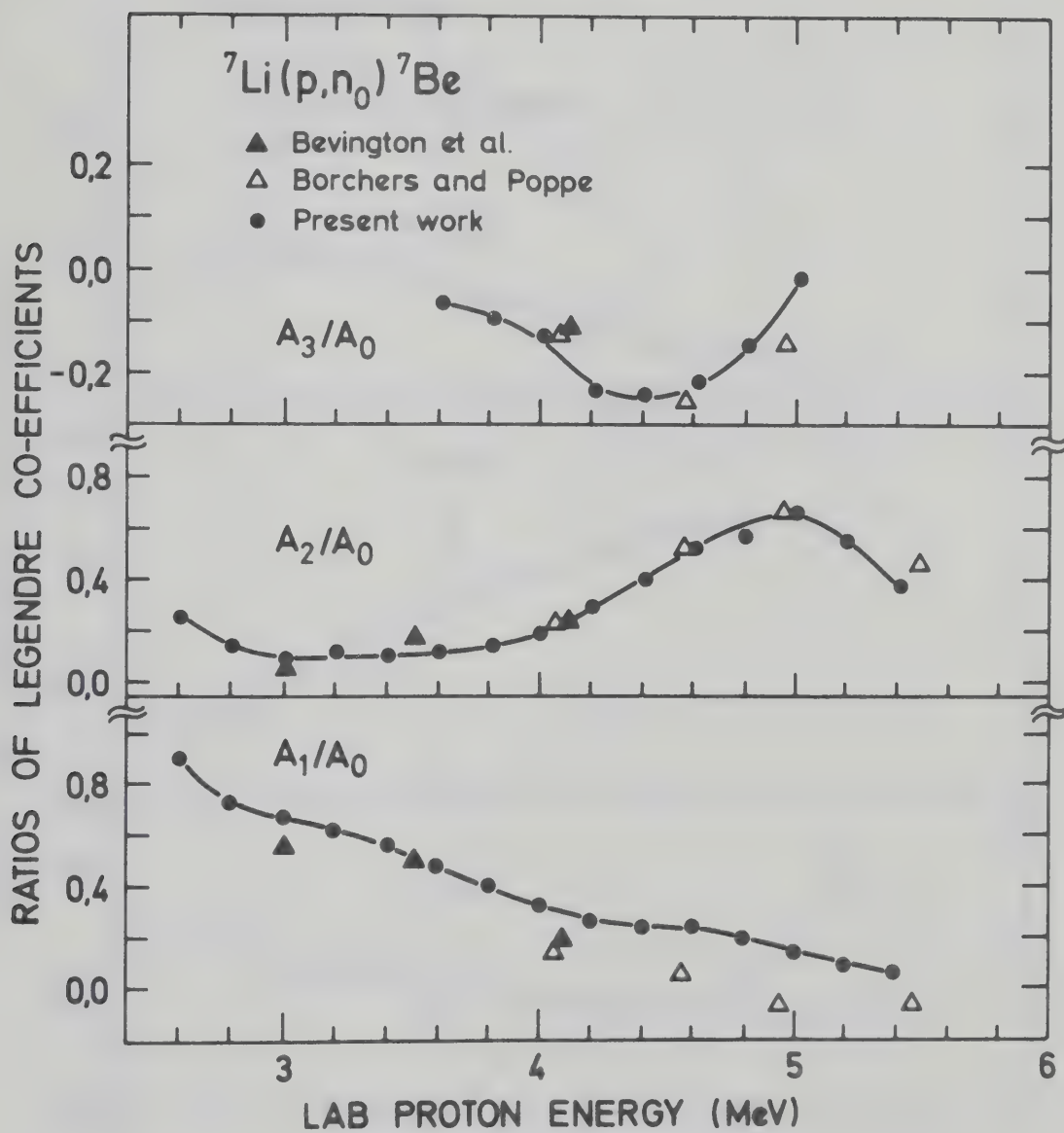


Figure 4



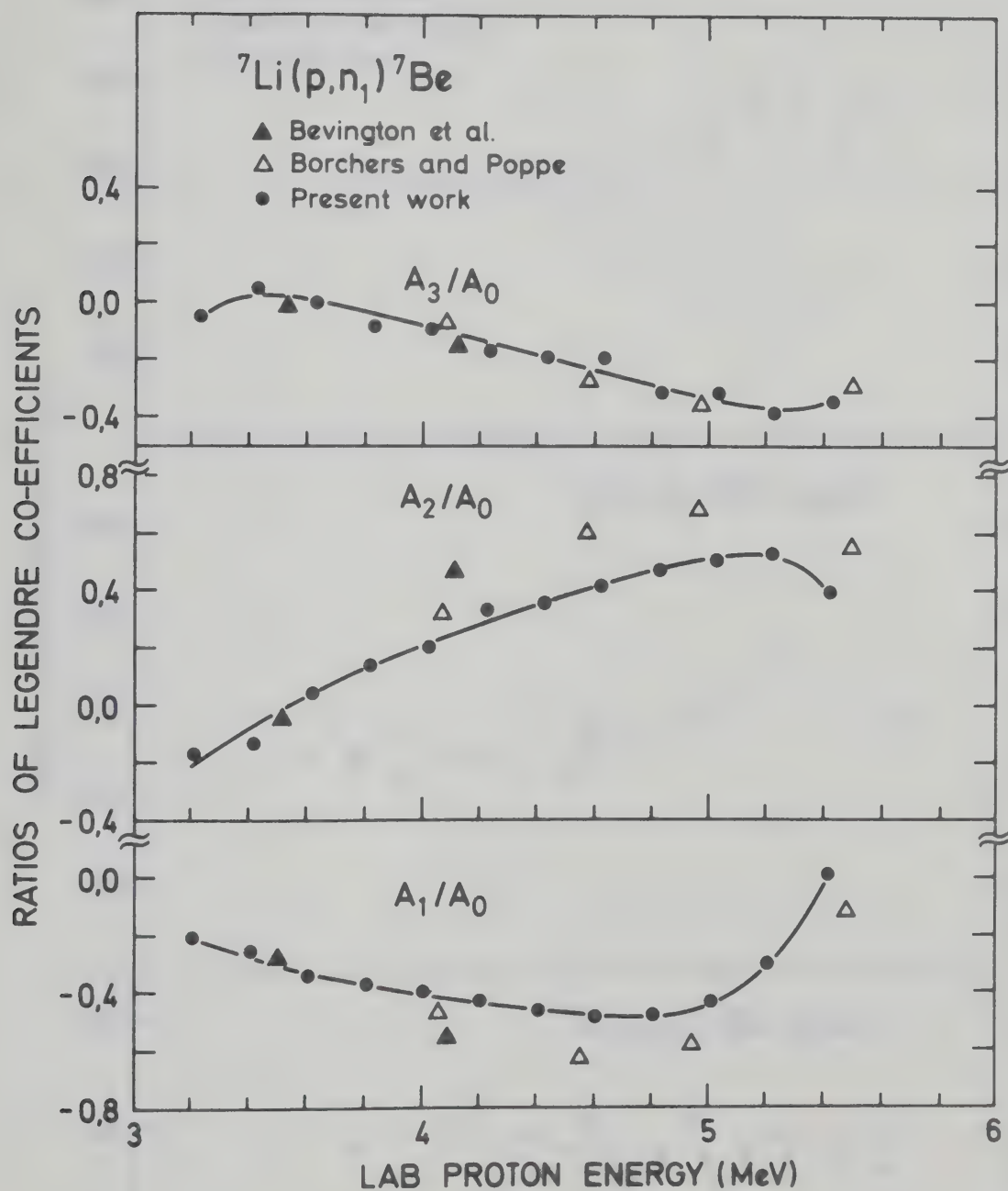


Figure 5



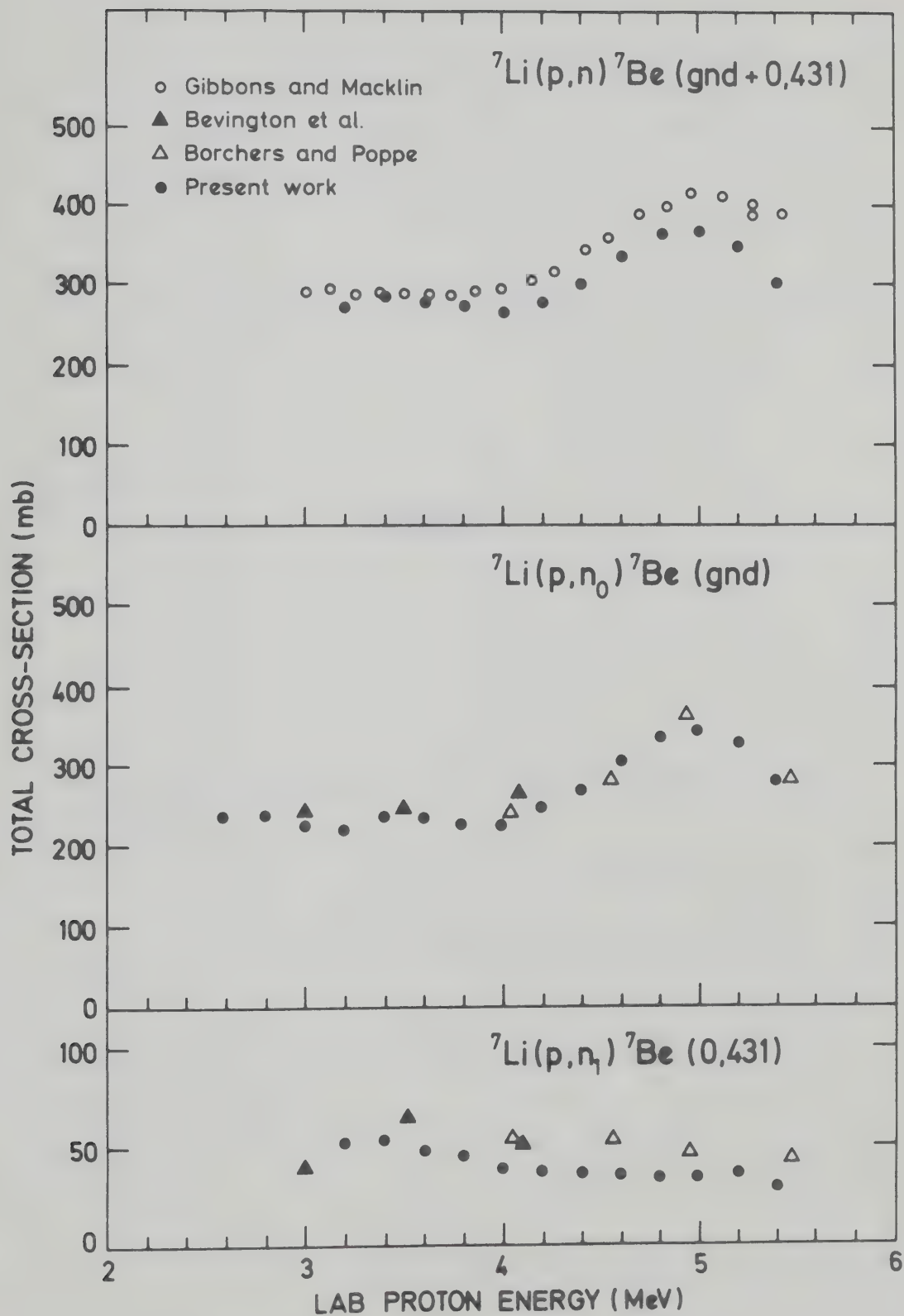


Figure 6



## APPENDIX B





## Geometrical Integration of Neutron Flux

In chapter III, the average production cross section has been defined as (eq. 3.6)

$$\overline{\frac{d\sigma}{d\Omega}} (\bar{E}_n, \psi_\gamma) = [Y_\gamma(E_p, \psi_\gamma)] \{C \int [I'_n(A_i; \rho, z) [\exp(-\mu_\gamma \ell_\gamma(\rho, \phi))]] \rho \, d\rho \, d\phi \, dz\}^{-1} \quad [B.1]$$

where

$$I'_n(A_i; \rho, z) = \left[ \sum_{i=0}^3 A_i P_i(\cos \theta_n) \right] \frac{1}{\rho^2 + z^2}$$

$$\theta_n = \tan^{-1}(\rho/z) \quad [B.2]$$

Apart from the exponential term, the integration of (B.1) can be written as

$$J_z = \int_{\rho \cot \alpha}^T \left[ \sum_{i=0}^3 A_i P_i(\cos \theta_n) \right] \frac{\rho}{\rho^2 + z^2} \, dz$$

The limits of integration are those given in chapter III.  
Changing variables

$$z = \rho \cot \theta_n$$

$$dz = \rho (-\csc^2 \theta_n) \, d\theta_n$$



when  $z = \rho \cot \alpha$   $\theta_n = \alpha$

and when  $z = T = \rho \cot \theta_n$   $\theta_n = \tan^{-1} \rho/T$

Eq. (B.3) can then be written as

$$\begin{aligned}
 J_z &= - \int_{\alpha}^{\tan^{-1} \rho/T} \left[ \sum_{i=0}^3 A_i P_i(\cos \theta_n) \right] \frac{\rho^2}{\rho^2 + z^2} \csc^2 \theta_n d\theta_n \\
 &= + \int_{\tan^{-1} \rho/T}^{\alpha} \left[ \sum_{i=0}^3 A_i P_i(\cos \theta_n) \right] d\theta_n \\
 &= f(\rho, T)
 \end{aligned} \tag{B.4}$$

Thus the integration of (B.1) is given by

$$J = \int_0^R \int_0^{2\pi} f(\rho, T) \exp [-\mu_Y(\rho, \phi)] d\phi d\rho \tag{B.5}$$

The integration (B.4) can be written explicitly as:

$$J_z = A_0 \int_{\tan^{-1} \rho/T}^{\alpha} [1 + a_1 P_1 + a_2 P_2 + a_3 P_3] d\theta_n \tag{B.6}$$

where  $a_i = A_i/A_0$ .

Therefore

$$J_z = A_0 [J_0 + J_1 + J_2 + J_3] \tag{B.7}$$

where

$$J_0 = \theta_n$$



$$J_1 = a_1 \int P_1 (\cos \theta_n) d\theta_n = a_1 \sin \theta_n$$

$$J_2 = a_2 \int \left[ \frac{1}{2} (3 \cos^2 \theta_n - 1) \right] d\theta$$

$$= 0.25 a_2 (\theta_n + 3 \sin \theta_n \cos \theta_n)$$

$$J_3 = a_3 \int \frac{1}{2} (5 \cos^3 \theta_n - 3P_1) d\theta_n$$

$$= a_3 (\sin \theta_n - 0.833 \sin^3 \theta_n)$$

when the limits of integration are applied, we get  $f(\rho, T)$  to be used in eq. (B.5). The integrations over  $\rho, \phi$  must be carried out numerically.













**B30039**